UNIVERSITÀ DEGLI STUDI DI TRIESTE

XXXV CICLO DEL DOTTORATO DI RICERCA IN FISICA

R&D for high-momentum hadron identification: from COMPASS RICH towards particle identification at the future Electron Ion Collider

---

Candidate:
Daniele D'AGO

Coordinator:
Prof. Francesco LONGO

Supervisors:
Dott. Fulvio TESSAROTTO
Dott. Silvia DALLA TORRE

A.A. 2021/2022

Abstract

Hadron production in semi-inclusive measurements of deep-inelastic lepton nucleon scattering (SIDIS) is one of the most powerful tools to investigate the hadron structure. Despite the brilliant results that it has given in the past decades, some fundamental questions, like the emergence of hadron mass and spin from the hadron constituents remain unanswered. A new generation of experiments, like ePIC at the EIC and AMBER at CERN, will shed light on the phenomena that are still unknown.
The core of SIDIS experiments is the measurement of the hadrons in the final state and their identification at high momenta ($p \gtrsim 20\ GeV/c$) is crucial; in this momentum range, Ring Imaging Cherenkov Detectors (RICH) are the most effective way to address particle identification. RICH technology, based on the Cherenkov light emission of particles faster than light in a suitable medium, generally requires the detection of photons on a wide detection area. Gaseous Photon detectors represent a well established, cost-effective way to cover large areas; moreover they can be operated in the presence of a magnetic field. Recently, the development of the MPGD technology has improved the performance of gaseous photon detectors in terms of speed and reduction of the ion backflow at the photocathode.
The R&D project presented in this thesis has the goal to export the MPGD-based photon detection technology developed for COMPASS RICH-1 to a future generation of experiments.
The large amount of data and the high data rate foreseen at the future experiments suggest the use of a triggerless Data Acquisition (DAQ) system, however the front-end electronics used in COMPASS MPGD-based photon detector (APV25) can operate only in trigger mode. A candidate to substitute the APV25 is the VMM, a 64 channels, digital ASIC developed for MPGDs. A prototype chamber, with the same characteristics as COMPASS MPGD-based photon detectors has been built and tested both with a known front-end electronics and with the VMM to confirm the reliability of the latter. Tests were performed using an X-rays and a UV light source to mimic Cherenkov photons. The two electronics gave comparable results with both photon sources, finding no obstacles to the use of VMM for the readout of MPGD-based Photon Detectors.
Another limitation of the MPGD-based Photon Detectors is the fragility of the CsI coated photocathodes: a severe decrease in quantum efficiency is observed following ion bombardment and/or exposure to humidity. In a gaseous detector the main source of ions is the avalanche process, so high radiation environments pose a limitation to the use of CsI based photocathodes. The thesis presents the study of a novel photoconverting material, hydrogenated nanodiamond (H-ND): its quantum efficiency is comparable with the one of CsI but it is more robust against radiation damage. In the thesis the production of the material is presented, as well as the *spraying technique* used to coat substrates. Presented results include studies of quantum efficiency, both in vacuum and in gas mixtures, and a study of radiation damage. The thesis is concluded by the study of the coupling of H-ND with

COMPASS type Photon Detectors; results indicate that the two technologies can be combined for a more robust MPGD-based Photon Detetctor.

Sommario

Un importante strumento per lo studio della struttura adronica sono le misure di produzione di adroni in processi di Deep Inelastic Scattering Semi - Inclusivo (SIDIS). Nei decenni passati queste misure hanno fornito preziose informazioni sulla struttura adronica, tuttavia alcune domande fondamentali, tra cui l'emergere della massa e dello spin adronici dai costituenti elementari, sono ancora senza risposta. Una nuova generazione di esperimenti, come ePIC a EIC e AMBER al CERN, è stata proposta per fare luce sui fenomeni ancora sconosciuti.
Il fondamento dei processi SIDIS è la rivelazione degli adroni nello stato finale e la loro identificazione ad alto momento ($p \gtrsim 20\ GeV/c$) è cruciale; in questo range di momenti, la tecnica più efficace per identificare gli adroni è rappresentata dai rivelatori Ring Imaging Cherenkov, detti RICH. La tecnologia RICH, basata sull'emissione di luce Cherenkov da parte di particelle che viaggiano a velocità superluminale in un mezzo adatto, normalmente richiede la rivelazione di fotoni su una grande area sensibile. I rivelatori di fotoni a gas rappresentano una soluzione ben consolidata e relativamente economica per coprire grandi superfici; inoltre possono essere utilizzati in presenza di campi magnetici. Recentemente, lo sviluppo della tecnologia Micro-Pattern Gaseous Detectors (MPGD) ha migliorato le performance dei rivelatori a gas per quanto riguarda la velocità e la riduzione del flusso di ioni sul fotocatodo.
Il progetto presentato in questa tesi ha lo scopo di esportare la tecnologia di rivelazione di fotoni, basata su MPGD, sviluppata per il RICH-1 di COMPASS a una nuova generazione di esperimenti.
Il grande numero e l'alto rate di dati previsto agli esperimenti futuri suggeriscono l'uso di un sistema di acquisizione non triggerato; tuttavia l'ettronica di front-end attualmente in uso nei rivelatori di fotoni a MPGD di COMPASS (APV25) può essere utilizzata solo in modalità triggerata. Un candidato per sostituire l'APV25 è il VMM, un ASIC digitale a 64 canali sviluppato come front-end per MPGD. Un prototipo di rivelatore, con le stesse caratteristiche dei rivelatori a MPGD di COMPASS è stato costruito e testato con un'elettronica dalla risposta nota e con il VMM, per confermare il funzionamento di quest'ultimo. I test sono stati fatti sia con una sorgente di raggi X che con una di fotoni UV, che imita i fotoni Cherenkov. Le due elettroniche hanno dato risposte compatibili con entrambe le sorgenti, determinando l'assenza di ostacoli all'uso del VMM per il readout di rivelatori di fotoni con tecnologia MPGD.
Un'ulteriore limitazione dei rivelatori di fotoni con tecnologia MPGD è la fragilità dei fotocatodi a ioduro di cesio (CsI): un'importante riduzione di efficienza quantica si osserva a causa del bombardamento di ioni. In un rivelatore a gas la principale sorgente di ioni è il fenomeno di moltiplica della carica, pertanto ambienti ad alta radiazione pongono un limite all'uso del CsI come fotocatodo. Questa tesi presenta lo studio di un nuovo materiale fotoconvertitore, la polvere di nanodiamante idrogenato (H-ND): la sua efficienza quantica è confrontabile con quella del CsI ma è più robusto contro

il danno da radiazione. Nella tesi sono presentati sia la produzione del materiale sia la tecnica con cui esso viene depositato su un substrato. I risultati includono studi di efficienza quantica sia in vuoto che in gas, e uno studio del danno da radiazione. La tesi è conclusa dallo studio dell'accoppiamento dei H-ND con i rivelatori di fotoni a MPGD; i risultati indicano che le due tecnologie possono essere combinate per costruire un rivelatore di fotoni robusto alla radiazione.

Contents

Chapter 1

Probing the Structure of the nucleon with lepton - nucleon scattering

1.1 Introduction

In the XX century many new particles were discovered and identified as the constituents of matter. The behaviour of these objects could not be described by classical mechanics, so a new theory was needed; an intense theoretical effort brought to the development of quantum mechanics: the new theory was a success, being in agreement with the experimental data. Quantum mechanics gave much importance to a property of the particles, the *spin*, that was introduced as a quantum number necessary to explain the behaviour of electrons in atoms.
In 1928 Paul Dirac extended quantum mechanics to the relativistic world; the equation that bears his name describes the motion of spin 1/2 fundamental particles (*i.e.* with no internal structure). One of the consequences of Dirac's equation is that the particle magnetic moment is:

$$\mu = g\frac{q}{2mc}\frac{\hbar}{2} \tag{1.1}$$

where m is the mass of the particle and q its electric charge, g is the gyromagnetic ratio and its value, determined from Dirac's theory, is 2 for spin 1/2 charged particles.
Dirac's theory provided a complete and successful description of the motion of the electrons, regarded as fundamental. The extension of this theory in the form of Quantum ElectroDynamics (QED) provides a quantum field description of the electromagnetic interaction. On the other hand, the proton and the neutron, collectively known as *nucleons*, have a magnetic moment different from the predicted one. If we assume that the two particles have the same mass and differ by the charge only, (e for the proton and 0 for the neutron) one should expect: $\mu_{proton} = \frac{e\hbar}{2m_p} = \mu_N$ and $\mu_{neutron} = 0$. However, precise measurements indicated that $\mu_{proton} = (2.79 \pm 0.02)\ \mu_N$ and $\mu_{neutron} = (-1.93 \pm 0.02)\ \mu_N$ (the results quoted are from [1] and [2]). The conclusion was clear, the nucleons are not fundamental particles, they have an internal structure. This discovery triggered extensive experimental and

theoretical studies with the scope of describing the internal structure of the nucleons. These studies are still ongoing today, in spite of the enormous progress obtained starting in the 60's of the XX century.

1.2 Probing the structure of the nucleon with scattering experiments

A powerful tool to investigate the structure of the nucleons is the scattering of structure-less particles off the nucleons. Information on the target structure can be extracted from the distribution of the projectile particles after the interaction.
In our current understanding, the electromagnetic interaction between electrons and protons at energies $\lesssim 100\ GeV$ is mediated by the exchange of a virtual photon. At low energies the scattering is dominantly elastic, which means that the probe interacts coherently with the proton as a whole, accessing its global properties. In the case of elastic interaction, a one to one correlation links the scattering angle with the transferred energy. The cross section of the process, then, can be studied as a function of the transferred energy by measuring the trajectory of the projectile in the final state. The proton was discovered not to be a point-like particle, but rather a *diffuse* object, whose distribution can be measured. In this theoretical frame the cross section for the process can be written as [3]:

$$\frac{d\sigma}{d\Omega} = \frac{\alpha^2}{4E_1^2 \sin^4(\theta/2)} \frac{E_3}{E_1} \left(\frac{G_E^2 + \tau G_M^2}{1+\tau} \cos^2 \frac{\theta}{2} + 2\tau G_M^2 \sin^2 \frac{\theta}{2} \right) \tag{1.2}$$

where E_1 and E_3 are the energy of the initial and final state leptons respectively and θ is the scattered lepton angle. If the four-momentum squared of the virtual photon is defined as q^2, then $\tau = \frac{Q^2}{4M_P^2}$, where $Q^2 = -q^2$ and M_P is the mass of the proton. The finite size of the proton is accounted for by the introduction of the form factors which describe the electric charge distribution (G_E) of the proton and the magnetic moment distribution (G_M) within the proton.
At increasing transferred momentum, the scattering process becomes dominantly inelastic, resulting in the formation of resonant states and eventually breaking the proton. The description of the inelastic processes requires the introduction of new kinematic variables. In an inelastic scattering in which a lepton with four-momentum p_1 exchanges a virtual photon of four-momentum q with a proton with four-momentum p_2, the four-momentum of the scattered lepton is p_3 and the W^2 is the invariant mass of the recoiling object(s) with four-momentum p_4. Hence $q^2 = (p_1 - p_3)^2 = 2m_l^2 - 2p_1 \cdot p_3$. Assuming that the energies involved are large compared to the masses of the leptons, one can choose a reference frame in which the direction of the impinging lepton coincides with the z axis and the scattered lepton forms an angle θ with respect to the z axis; the four-momenta can be written as $p_1 = (E_1, 0, 0, E_1)$ and $p_3 = (E_3, E_3 sin\theta, 0, E_3 cos\theta)$ and the transferred

momentum becomes $q^2 = -4E_1E_3sin^2\frac{\theta}{2} = -Q^2$. Bjorken introduced the Lorentz invariant kinematic variable x [4] defined, using the nomenclature introduced above, as:

$$x = \frac{Q^2}{2p_2 \cdot q} \tag{1.3}$$

Using the definition of W as the invariant mass of the recoiling object(s), equation 1.3 can be written as:

$$x = \frac{Q^2}{Q^2 + W^2 - M_P^2} \tag{1.4}$$

The invariant mass of the final state hadronic system is always greater than the proton rest mass, therefore, for $Q^2 \geq 0$, the equation 1.4 implies $0 \leq x \leq 1$. This new variable has an important physical meaning: it describes the "elasticity " of a scattering process, $x = 1$ corresponding to the elastic case.
Another Lorentz invariant variable used to describe the inelasticity of the process is defined as $y = \frac{P_2 \cdot q}{P_2 \cdot P_1}$. In the proton rest frame $y = \frac{M_P(E_1 - E_3)}{M_P.E_1} = \nu E_1$, where ν is defined as the energy lost by the incoming lepton: $\nu = E_1 - E_3$.

1.2.1 Deep Inelastic Scattering

The new variables allow to generalize the formula 1.2 to the inelastic case with the introduction of two structure functions, F_1 and F_2 replacing the electric and magnetic form factors [5].

$$\frac{d^2\sigma}{d\Omega dE_3} = \frac{\alpha^2(\hbar c)^2}{4E_1^2 sin^4\frac{\theta}{2}} cos^2\frac{\theta}{2}\left[\frac{F_2(x,Q^2)}{\nu} + \frac{2F_1(x,Q^2)}{M_P c^2} tan^2\frac{\theta}{2}\right] \tag{1.5}$$

Note that, since the process is inelastic, the cross section is double differential in Ω and E_3, or equivalently, Q^2 and x. From the intensive and systematic study of the proton structure functions carried out at SLAC thanks to the availability of intense electron beams with high energy (25 GeV), a surprising result emerged: at fixed values of x the two structure functions $F_1(x, Q^2)$ and $F_2(x, Q^2)$ are almost independent on Q^2. This means that the electrons are scattered off a point-like charge, and it was concluded that the nucleons have a sub-structure made up of point-like constituents. Events of the type described above are commonly called Deep Inelastic Scatterings, shortened in DIS.
Another important experimental observation is that, for $Q^2 >$ few GeV^2, the two structure functions are not independent:

$$F_2(x, Q^2) = 2xF_1(x, Q^2) \tag{1.6}$$

always holds. This relation, known as Callan-Gross relation, is valid for spin 1/2 Dirac particles; the point-like constituents of the nucleon have spin 1/2.

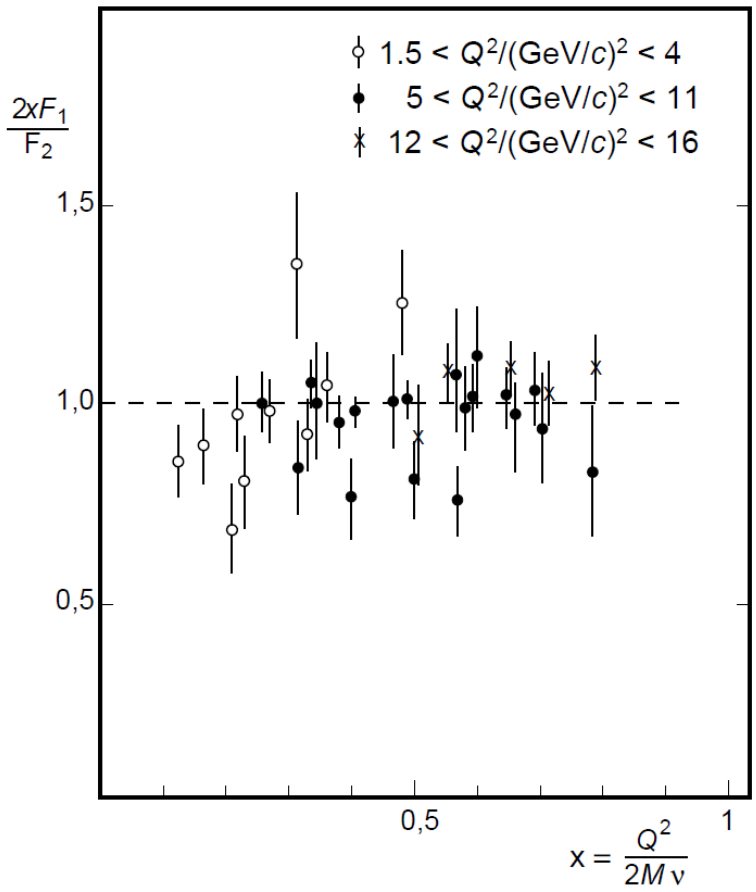

FIGURE 1.1: Experimental verification of Callan-Gross relation for different values of x from [5].

Experimental verification of this equation is shown in figure 1.1
If we use Callan-Gross relation in equation 1.5 we obtain:

$$\frac{d^2\sigma}{d\Omega dE_3} = \frac{\alpha^2(\hbar c)^2}{4E_1^2 sin^4\frac{\theta}{2}} cos^2\frac{\theta}{2}\left[1 + \frac{Q^2}{ax^2M_P^2c^2}2tan^2\frac{\theta}{2}\right]\frac{F_2(x,Q^2)}{x} \tag{1.7}$$

which is the cross section for an elastic scattering off point-like, spin $1/2$ particles with mass $m = xM_P$.

1.2.2 The quark parton model

The experimental approach described in the previous section was used in the '50s and '60s at SLAC to study the structure of the nucleons [6]. The physics of the process requires that the projectile has no internal structure, so the choice fell on electrons; an advantage of electrons, moreover, is their stability, which ensures an easier handling. At SLAC, artificially accelerated electrons were fired against a liquid hydrogen (or liquid deuterium) target.
An interpretation of the experimental results was given by Feynman in his *parton model*. He imagined that the proton is made of a bunch of particles called **partons**, each one carrying a fraction ξ of the the momentum of the

parent particle. Decomposing the proton into free moving partons, the interaction of the electron with the proton can be viewed as the incoherent sum of its elastic scatterings off the individual partons. This approximation is valid as long as the duration of the photon-parton interaction is so short that the interaction among the partons can be neglected. Figure 1.2 shows schematically the interaction of the lepton with a single parton.

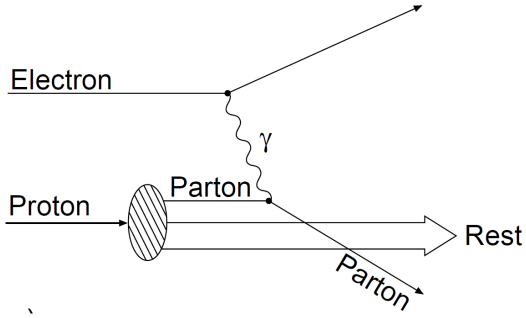

FIGURE 1.2: Schematic representation of a DIS event.

Let us sit in a reference frame in which the energy of the proton is much larger than its mass - like, for instance, the rest frame of the lepton in a DIS event. In this reference frame we can neglect the mass of the proton and the transverse components of its momentum. This particular reference frame is called the *infinite momentum frame*. Assuming that the proton is moving in the z direction with momentum P_z, the momentum of the partons will be $k = \xi P_z + k_T$. Then, we can compute the squared mass of the parton recoiling after the interaction with the photon; in the infinite momentum frame the transverse component of the parton momentum and the mass of the recoiling object can be neglected.

$$m^2_{parton} = |\xi P + q|^2 \simeq 0 \quad \Rightarrow \quad \xi^2 P^2 + q^2 + 2\xi P \cdot q \simeq 0 \tag{1.8}$$

Neglecting $\xi^2 P^2$ and recalling the definitions of the variables from the previous sections we obtain:

$$\xi = \frac{Q^2}{2M\nu} \tag{1.9}$$

This corresponds to the definition of x given by Bjorken; in this reference frame x describes the fraction of the momentum of the parent particle carried by the struck quark. In general the partons will have a momentum distribution, $f_i(x)$, where i indicates the type of parton (an interpretation of the different types of parton will be given in the context of the quark model). Then, $f_i(x)$ represents the probability of finding a quark of type i with a momentum fraction x of the parent nucleon in the infinite momentum frame; this distribution is called **parton distribution function (PDF)**. Since the cross section for DIS is interpreted as the incoherent sum of scattering events on single partons, we can rewrite it as:

$$\frac{d^2\sigma}{dxdQ^2} = \sum_i f_i(x)\left(\frac{d^2\sigma}{dxdQ^2}\right)_i \tag{1.10}$$

If we compare equations 1.7 and 1.10, we can interpret the structure function $F_2(x)$ as the sum of the different PDFs weighted by the square of the parton charge, z_i^2.

$$F_2(x) = x\sum_i z_i^2[f_i(x) + \bar{f}_i(x)] \tag{1.11}$$

In equation 1.11 $\bar{f}_i(x)$ represents the PDF for the antiparton and will have an interpretation in the quark model. Figure 1.3, taken from[7], summarizes, as an example, the measurements of the proton $F_2(x)$; the combination of experimental measurements taken over many years of dedicated efforts results in a precise knowledge of $F_2^p(x)$.
In the years in which Feynman developed the parton model, a set of new particles was discovered. The description of these particles and of the processes in which they were produced imposed the definition of a new conserved quantity, *strangeness*. M. Gell-Mann and Y. Ne'eman showed that the recently discovered particles, along with the known ones, can be grouped in octets and decuplets as a representation of a SU(3) symmetry group. The large number of particles and the absence of the simplest SU(3) representation, the triplet, were hinting the existence of a substructure. A model of the hadron underlying structure came from Gell-Mann and Zweig [8]; they suggested that the hadrons are made of point-like sub particles with spin 1/2 and fractional charge called **quarks**. In this model mesons are bound states of a quark and an antiquark, while baryons are bound states of three quarks. The quarks introduced by Gell-Mann and Zweig are the natural candidates to be identified as Feynman's partons, however the combination of the two models is not straightforward.

If Gell-Mann and Zweig quarks were the only constituents of the nucleons, the model with the known quantum numbers would violate the Fermi - Dirac statistics: a nucleon would contain two particles with the same quantum numbers. This puzzle was solved introducing a new quantum number, the *colour* (see next section). According to the model, the fundamental quarks are three, "up" (u), with electric charge $+\frac{2}{3}e$, "down" (d) and "strange" (s) with electric charge $-\frac{1}{3}e$; as they are Dirac particles they have their respective antiparticle $\bar{u}$, $\bar{d}$ and $\bar{s}$. This model was then extended with the discovery of new particles and to the present knowledge it includes three more quarks, "charm" (c) and "top" (t), with electric charge $+\frac{2}{3}e$ and "bottom" (b), with electric charge $-\frac{1}{3}e$, and their antiparticles. The force binding the quarks together is a "new" force, different from the electromagnetic and the weak one, called *strong interaction*.

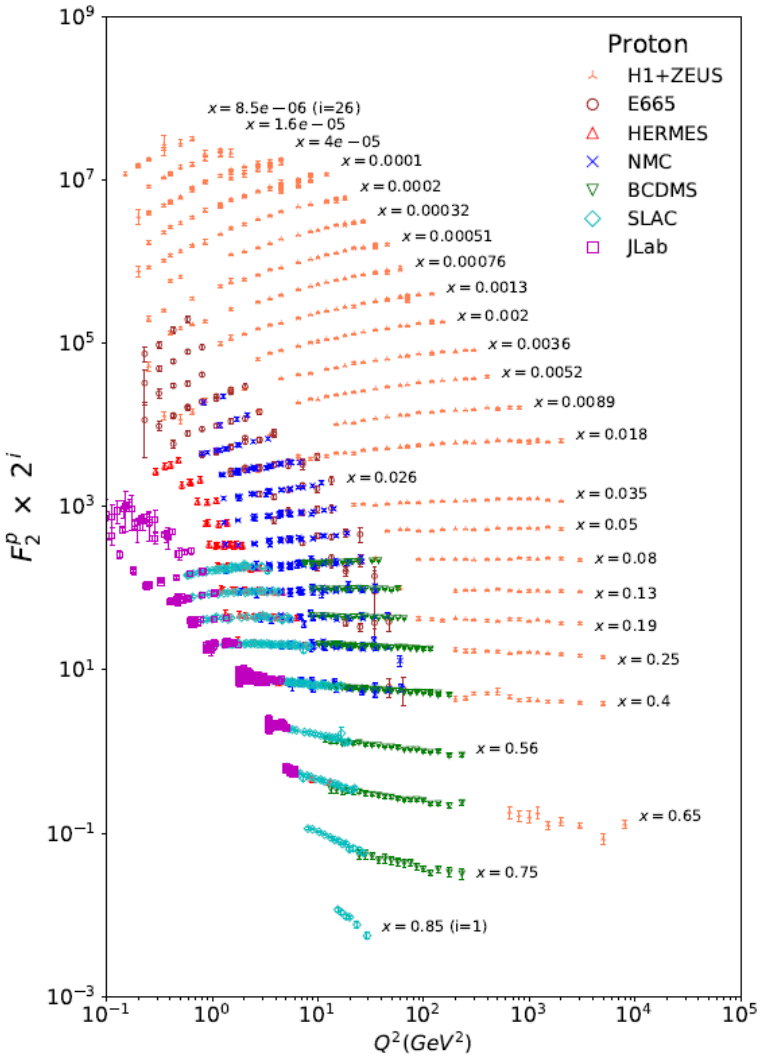

FIGURE 1.3: Summary of experimental measurements of the structure function F_2 for the proton from [7]. Combined efforts of different collaborations result in a precise knowledge of this structure function.

1.2.3 Quantum ChromoDynamics

A field theory was developed for describing the dynamics of the strong interaction in analogy to QED; this theoretical framework is known as Quantum ChromoDynamics(QCD) [6]. In the QCD description, the quarks interact among themselves via the exchange of gauge bosons named **gluons**. Each quark, along with the electric charge, carries a color charge, a quantity that exists in three states, named after the fundamental colours, red, green and blue. Free particles must have a net color charge of zero; in the most simple case, total colour charge can be zero in a three quark system where each quark carries a different colour charge, or in a quark - antiquark pair, where the quark has a colour charge and the antiquark an anticolour charge. Systems of the first type are globally known as baryons while systems of the second type take the collective name of mesons.

Unlike the photons in QED, gluons carry a colour charge and interact among themselves.
The current QCD picture of the nucleons is more complex than the description given in the QPM frame. In the nucleons an infinite number of quarks of each flavour are continuously created and annihilated and they interact exchanging gluons. These quarks are called "sea quarks". Three quarks emerge out of the sea and determine the global properties of the nucleon. These quarks are called "valence quarks". In a DIS experiment the lepton can interact with both valence and sea quarks with a certain probability that depends on the scale of the interaction x. Figure 1.4 schematically shows the dependence of the interaction on the energy scale. At low photon energy the lepton interacts with the nucleon as a whole, while at higher photon energies the interaction occurs between the photon and one of the partons. At much higher energy scale the lepton probes partons that interact among themselves.

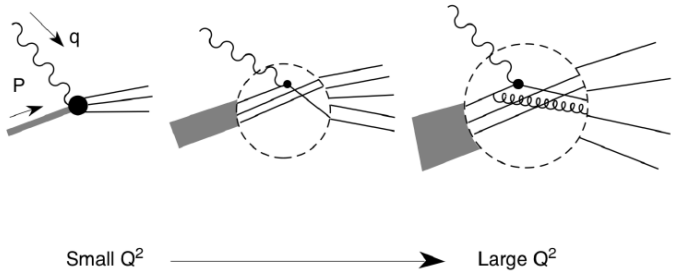

FIGURE 1.4: Scheme of the lepton - nucleon interaction. At small Q^2 the lepton interacts with the nucleon as a whole, for increasing Q^2 the nucleon is probed at a smaller scale.

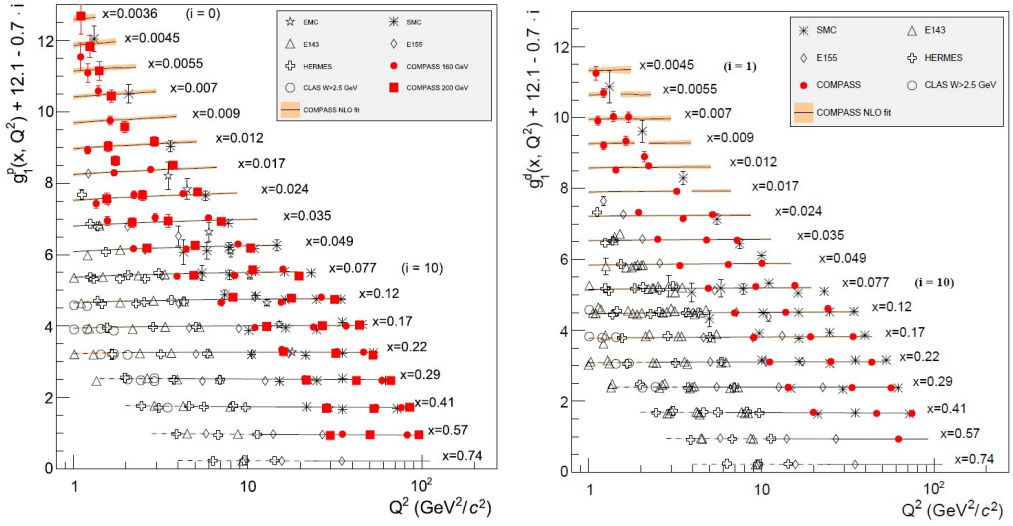

FIGURE 1.5: Experimental measurements of $g_1(x)$ for the proton (left) and for the deuteron (right) from [9] and [10] respectively

1.2.4 Spin dependent DIS

The DIS experiments described above elucidated the quark - gluon structure of the nucleon, demonstrating that the quarks have spin 1/2; however, they provided no information about the distribution of the nucleon spin among its constituents. The nucleon spin is decomposed, according to [11] in the contributions of its constituents, namely the quark and the gluon spins ($\Delta\Sigma$ andΔG respectively) and angular momenta (L_{Q+G}).

$$\frac{1}{2} = \frac{1}{2}\Delta\Sigma(\mu) + \Delta G(\mu) + L_{Q+G}(\mu) \tag{1.12}$$

This spin contribution can be measured in DIS experiments provided the projectile and the target have defined and known spin orientation. Scattering experiments can be, then, carried out, considering different relative orientation of nucleon and lepton spin and measuring asymmetries in the cross section. In the theoretical framework known as parton model, the interaction is regarded as the elementary interaction between the virtual photon and a single constituent of the nucleon, a parton. In this description, only the photon direction, the direction along which the partons are boosted, is relevant for the description of the interaction. With respect to this direction, marked as the z axis, both the photon and the parton spins have two possible projection, namely positive and negative. Since the parton spin is 1/2, the absorption of the photon by the parton can occur only if the two projections of the spin along z have opposite sign, so to result in a spin flip for the parton. From the experimental point of view, however, only the photon and the nucleon polarisation can be determined; the information that can be extracted on the parton concerns whether is was polarised parallel or antiparallel to the parent nucleon. The measured observable is the spin asymmetry defined as the difference in cross section between the two relative spin configurations normalised by the total cross section. The asymmetries can be expressed in terms of two spin dependent structure functions $g_1(x)$ and $g_2(x)$, in analogy with the structure functions introduced for the unpolarised DIS. In particular, $g_1(x)$, named *helicity*, can be interpreted as the probability of finding, in a longitudinally polarised nucleon, a quark with spin parallel to the spin of the nucleon [12]. Figure 1.5 shows a compilation of experimental measurements of $g_1(x)$ for the proton (left) from [9], and for the deuteron (right), from [10]. In the QPM framework, $g_1(x)$ is interpreted as the distribution of the nucleon spin among its constituents. Its integral over x, is related to the total contribution of the quark spins to the nucleon spin, $\Delta\Sigma$. It was believed that a large fraction of the nucleon spin was due to the contribution of the quarks, however in 1989 the EMC collaboration published a surprising result [14, 15]: the quark spins account for just a fraction of the nucleon spin; this discovery went down in history as the "nucleon spin crisis". It became urgent, at that point, to measure the gluon contribution to the spin, ΔG.

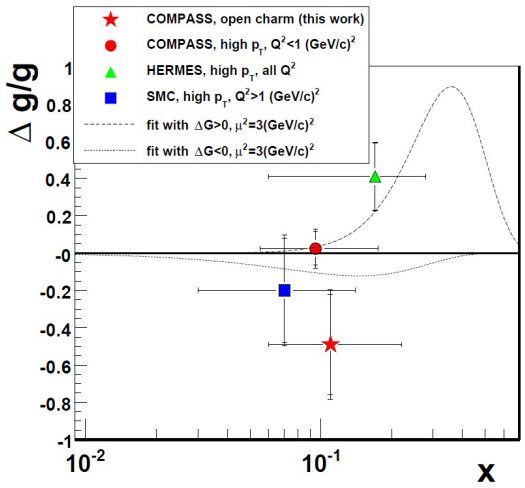

FIGURE 1.6: Experimental measurements of gluon spin contribution to the proton spin [13]

1.2.5 Semi Inclusive Deep Inelastic Scattering

Unlike the quarks, however, the gluons do not interact directly with the photons and probing their spin structure is challenging; the way out is represented by the measurement of interactions of photons with quarks created by the splitting of gluons. From the experimental point of view, to identify such a process the detection of the projectile lepton in the final state is not sufficient; a hadron must be measured as well to tag the event as DIS on a quark created by gluon interaction. This type of processes, where both the final state electron and at least one final state hadron are identified, are called semi-inclusive DIS, shortened as SIDIS [12]. SIDIS processes were used to estimate the gluon contribution to the nucleon spin by several collaborations; figure 1.6 refers to the measurements taken at COMPASS at CERN [13, 16]. The SIDIS events relevant for the determination of ΔG are characterized by particularly large transverse momentum of the final state hadron [16] or by the presence of a charmed hadron in the final state [13]: since there's no valence charm quark, the production of a charmed hadron is the signature of a $c\bar{c}$ pair produced by a gluon. In both cases, however, uncertainties are large.
To describe the spin structure of the nucleon helicity is not enough: a DIS experiment can be carried out polarizing the nucleon in a direction that lays on a plane orthogonal to the photon direction. In this case, the structure function that describes, in a transversely polarized nucleon, the probability of finding a quark with spin parallel to the one of the nucleon is called *transversity*, indicated as $h_1(x)$. Transversity is a chiral-odd function and thus can not be observed in DIS events [17]. However, its effects can be measured when it couples with a chiral-odd object, like a fragmentation function (FF), a function that describes the formation of colourless hadrons (hadronisation) from the interacting quarks. The main method used for extracting transversity is via the *Collins FF* [17], that describes the hadronisation of a polarised quark into a non polarised hadron. The result of the coupling is a modulation of the distribution of the hadrons in the final state that depends on the spin of

the nucleon: it is clear that only a SIDIS experiment can measure it. Other methods that allow to access transversity, like di-hadron asymmetry [18], require SIDIS experiments. Transversity was measured by several experiments; in figure 1.7 results from COMPASS collaboration [19] are quoted. Since transversity is convoluted with another function, its extraction from experimental data is not trivial and requires some assumptions on the functional form of both transversity and FF; information on the FFs come from independent measurements [19].
Finally, SIDIS experiments are a fundamental tool to perform a basic flavour separation of the structure functions.

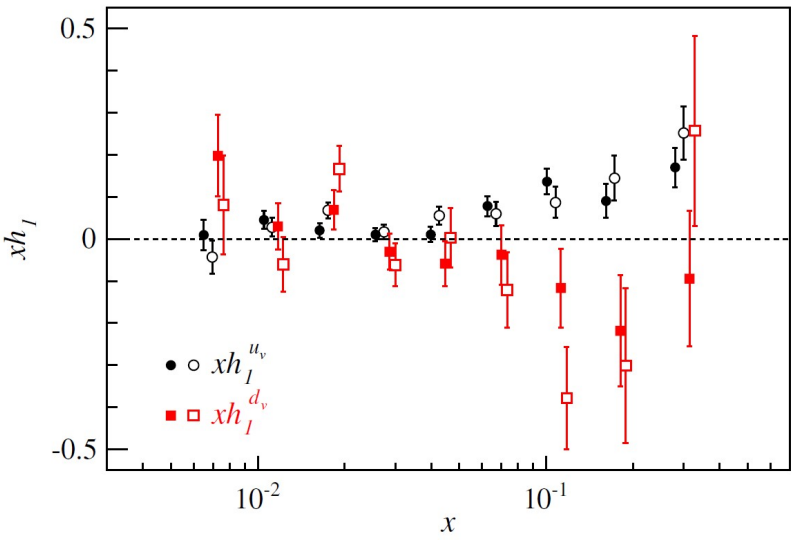

FIGURE 1.7: Extraction of transversity from COMPASS data from [19]. Results from two spin asymmetries are presented, di-hadron (open points) and Collins (solid points).

1.2.6 Transverse Momentum Dependent Structure Functions

In the description of the nucleon structure given by the parton model as exposed in section 1.2.2 the partons are assumed to have only longitudinal momentum. The assumption derives from the consideration that in a boosted frame all the non collinear components can be neglected. However, parton distribution functions can be generalized to include a non zero transverse component of the parton momentum, $\mathbf{k}_T$. If the parton transverse momentum is not zero, it induces an azimuthal modulation in the distribution of hadrons in the final state; this phenomenon is known as the Cahn effect [20]. Another modulation arises from the correlation between the parton intrinsic transverse momentum and its transverse spin; both phenomena can be observed only in a SIDIS experiment. Finally, if one considers all the possible combinations of spins and intrinsic momenta, for a spin 1/2 hadron eight Transverse Momentum Dependent PDFs are obtained for the quarks and eight for the gluons, summarized in table 1.1. If the transverse momenta are

integrated over, only three PDFs survive, the ones described in the sections above, namely $f_1(x)$, $g_1(x)$ and $h_1(x)$. The cross section for polarised SIDIS, assuming single photon exchange, can be expressed in a model-independent way by a set of structure functions [21]:

$$\begin{aligned}
\frac{d\sigma}{dxdydzdp_T^2 d\phi_h d\phi_s} &= \left[\frac{\alpha^2}{xyQ^2}\frac{y^2}{2(1-\varepsilon)}\left(1+\frac{\gamma^2}{2x}\right)\right] \times \Big\{F_{UU,T} + \varepsilon F_{UU,L} \\
&+ \sqrt{2\varepsilon(1+\varepsilon)}F_{UU}^{cos\phi_h} cos\phi_h + \varepsilon F_{UU}^{cos(2\phi_h)} cos(2\phi_h) + \sqrt{2\varepsilon(1-\varepsilon)}F_{LU}^{sin\phi_h} sin\phi_h \\
&+ S_\parallel\left[\sqrt{2\varepsilon(1+\varepsilon)}F_{UL}^{sin\phi_h} sin\phi_h + \varepsilon F_{UL}^{sin(2\phi_h)} sin(2\phi_h)\right] \\
&+ S_\parallel\lambda_\ell\left[\sqrt{1-\varepsilon^2}F_{LL} + \sqrt{2\varepsilon(1-\varepsilon)}F_{LL}^{cos\phi_h} cos\phi_h\right] \\
&+ |\mathbf{S}_\perp|\Big[\left(F_{UT,T}^{sin(\phi_h-\phi_s)} + \varepsilon F_{UT,L}^{sin(\phi_h-\phi_s)}\right) sin(\phi_h-\phi_s) \\
&+ \varepsilon F_{UT}^{sin(\phi_h+\phi_s)} sin(\phi_h+\phi_s) + \varepsilon F_{UT}^{sin(3\phi_h-\phi_s)} sin(3\phi_h-\phi_s) \\
&+ \sqrt{2\varepsilon(1+\varepsilon)}F_{UT}^{sin\phi_s} sin\phi_s + \sqrt{2\varepsilon(1+\varepsilon)}F_{UT}^{sin(2\phi_h-\phi_s)} sin(2\phi_h-\phi_s)\Big] \\
&+ |\mathbf{S}_\perp|\lambda_\ell\Big[\sqrt{1-\varepsilon^2}F_{LT}^{cos(\phi_h-\phi_s)} cos(\phi_h-\phi_s) + \sqrt{2\varepsilon(1-\varepsilon)}F_{LT}^{cos\phi_s} cos\phi_s \\
&+ \sqrt{2\varepsilon(1-\varepsilon)}F_{LT}^{cos(2\phi_h-\phi_s)} cos(2\phi_h-\phi_s)\Big]\Big\}
\end{aligned} \tag{1.13}$$

In equation 1.13, the target spin vector, called S, can be decomposed in $S_\parallel$, its projection along the photon direction, and $\mathbf{S}_\perp$, that forms an angle ϕ_S with respect to the scattering plane, *i.e.* the plane containing the incoming and scattered lepton momenta and the virtual photon direction; ϕ_h is the angle of the outgoing hadron. λ_ℓ is the lepton helicity and ε is the ratio of longitudinal and transverse photon flux. The structure functions, that depend on x, z, Q^2 and $P_{h\perp}^2$, are indicated with F followed by a set of subscripts: the first and the second indicate the polarisation of the beam and of the target, respectively, while the third, where present, the polarisation of the virtual photon. Equation 1.13 shows all the azimuthal modulations induced by the correlation between the TMD PDFs and the nucleon spin. The amplitudes of the modulations are proportional to the convolutions of the PDFs with the fragmentation functions (FF) that describe the hadronisation. FFs depend on the parton transverse momenta as well and need to be measured. In principle, then, polarised SIDIS experiments are capable of measuring all the azimuthal modulations of the cross section and thus extracting the TMD PDFs.

1.3 COMPASS: an experiment to investigate QCD

Some of the results quoted in the previous sections are taken from the measurement of the COMPASS collaboration at CERN. One of the purposes of

		quark		
		U	L	T
nucleon	U	$f_1(x,k_T^2)$		$h_1^\perp(x,k_T^2)$
	L		$g_1(x,k_T^2)$	$h_{1L}^\perp(x,k_T^2)$
	T	$f_{1T}(x.k_T^2)$	$g_{1T}(x.k_T^2)$	$h_1(x,k_T^2)$ $h_{1T}^\perp(x,k_T^2)$

TABLE 1.1: The eight TMD PDFs. The coloured parts represent the only functions that survive after the k_T integration.

COMPASS spectrometer is the measurement of some fundamental quantities, like the gluon contribution to the spin and the quark transversity, that were largely unknown at the time of its conception; other important measurements include light hadron spectroscopy and diffractive processes [22]. This rich physics programme is pursued by Deep Inelastic Scattering (DIS), Semi Inclusive DIS (SIDIS), Drell-Yann processes, bot polarised and unpolarised, and exclusive measurements at high rate and covering a wide phase-space region of the interaction products. COMPASS spectrometer lies on the CERN SPS M2 beamline that can provide a high energy polarized muon beam and high energy secondary hadron beams. The beam particles collide on a target (of different materials according to the specific physics channel) and the products of the interaction are analyzed by the 60 m long COMPASS spectrometer. The spectrometer is characterized by a wide angular acceptance obtained with a two-stage strategy, where the first spectrometer is mainly dedicated to large angle acceptance and the second one to precise analysis of the high momentum particles. Both spectrometers are equipped with magnets for particle momentum analysis. Figure 1.8 shows a schematic view of the two-stage spectrometer of COMPASS. Notable achievements of the COMPASS collaboration in unveiling the hadron structure include the measurement of all the azimuthal modulation of the SIDIS cross section described in equation 1.13.

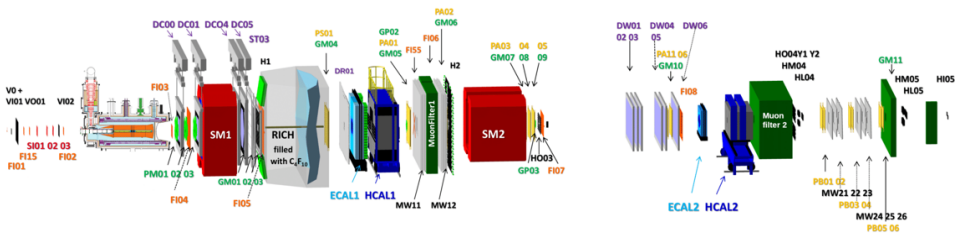

FIGURE 1.8: A schematic view of the two-stage spectrometer of COMPASS.

1.4 The unanswered questions

In the previous sections of this chapter we have seen that DIS and SIDIS processes, both polarized and unpolarized are powerful tools to explore the connection between QCD and the global properties of the nucleons. However, some fundamental links between QCD and its manifestation are not yet clear.
The nucleon spin puzzle, for instance, has not been solved yet. It is clear that neither $\Delta\Sigma$ nor ΔG can account for the total spin of the nucleon, according to the most recent data [23], nevertheless they have large uncertainties, as can be seen for ΔG in figure 1.6, mainly due to the poor knowledge of helicity in the region at low x ($x \lesssim 0.005$). New measurements in this kinematical region are needed.
Like the nucleon spin, the mass of the nucleons can not be simply explained as the sum of the masses of its constituents. In fact, the sum of the masses of the quarks, provided by the Higgs mechanism, is by far too low to account for the large masses of the nucleons. The origin, then, must be found in the strong force that tightly binds quarks and gluons together and intense investigation in this field is ongoing [23].
In section 1.2.6 the Transverse Momentum Dependent Structure Functions are described, as well as their appearance as modulations of distribution of hadrons in the final states of a SIDIS process. A detailed measurement of these modulations in a wide kinematical range is strongly needed to extract the values of the quark and gluon TMD PDFs; they will provide a full description of the nucleons both in position and in momentum space [23].

1.4.1 New QCD facilities

To answer the questions still pending in our understanding of the nucleon physics, as well as many other topics, new laboratories and experiments are being designed and built. Among them, the AMBER collaboration will upgrade the present COMPASS spectrometer to perform a wide range of measurements aiming at unveiling the hadron structure via SIDIS and Drell-Yann processes. The vast physics programme includes, among its diverse goals, the determination of the valence structure functions of pions and kaons, the measurement of the radius of the charge distribution of the proton via elastic scattering and the further investigation of the spin structure of the nucleons. A long term goal of the collaboration is to shed light on the emergence of hadron masses, deeply connected to the parton dynamics.

1.4.2 Electron Ion Collider

The present thesis is focused on the the project I was involved in, the Electron Ion Collider, EIC. The Electron Ion Collider is a new large scale particle accelerator that is planned for construction at Brookhaven National Laboratories (BNL). The machine can be considered a large scale electron microscope that studies nucleons and atomic nuclei by colliding them with a high energy

electron beam.
Few design parameters are essential for the successful achievement of the physics goals of the EIC. A high luminosity is required and the machine is designed for reaching a peak luminosity between $10^{33} cm^{-2} s^{-1}$ and $10^{34}\ cm^{-2} s^{-1}$. To ensure a wide kinematic range, a large coverage in phase space, a variable centre of mass energy $\sqrt{s}$ in the range $20 - 100\ GeV$ is required; moreover, some measurements require a variation in $\sqrt{s}$. The machine can be upgraded to reach $\sqrt{s} = 140\ GeV$, necessary to provide sufficient kinematic reach in the gluon dominated region.
The wide physics programme includes the measurement of double spin asymmetries, where both beams are polarised, and single spin asymmetries, where only one beam, typically the hadron one, is polarised. In both cases the statistical uncertainties on the asymmetries depend on the level of polarisation of the beams. The accelerator machine must then ensure longitudinal and transverse polarization orientation for protons, deuterons, ^3He, and other polarizable light nuclei, as well as longitudinal polarization for the electron beam. Light ion beams are necessary to study the A-dependence of gluon saturation and to investigate the nucleon structure. On the other hand, heavy ion beams at high $\sqrt{s}$ allow high gluon densities and a tool to understand the propagation of coloured particles through nuclear matter. Electron and Ion beams will collide in two points along the accelerator ring, following the existing structure at RHIC. The presence of two independent detectors, one per each interaction point, is of scientific interest [23], although at the moment only one is being planned, ePIC. While the design of the detector is not finalised yet, some features are mandatory for successfully accomplishing the physics programme. The detector must be hermetic, for an efficient tracking and particle identification and for a precise measurement of the energies of the final state particles, that span a wide range, between 10 MeV and 10 GeV [23]. The design of detectors at the EIC is centered around solenoidal superconducting magnets with bipolar fields. The solenoidal configuration naturally leads a detector configuration organized in barrel and endcap.
The asymmetric nature of the interactions at the EIC poses unique detector requirements: barrel, hadron endcap and electron endcap see very different particle distributions, in terms of momenta and particle types. Tracking and vertexing detector systems must have a high granularity to reach the required space resolution, down to 5 μm for tracking and 3 μm for vertexing. A low material budget, as low as 0.8% of radiation length in the barrel and 0.1% in the endcap is also required. Calorimetry is essential to measure the energies of the particles coming from the interactions. An electromagnetic calorimeter (ECAL) constrains the electron kinematics and aids in separating electrons from hadrons, in detection of neutral particles, and the identification of the two photons of neutral pion decays. A hadron calorimeter (HCAL), on the other hand, is required for the measurement of the total energy in hadronic jets, in particular for neutral components which are not tracked. An efficient particle identification is required to separate electrons from pions, kaons and protons. A pion, kaon, proton separation better than 3σ in all the rapidity range is crucial to achieve the physics goals of the EIC.

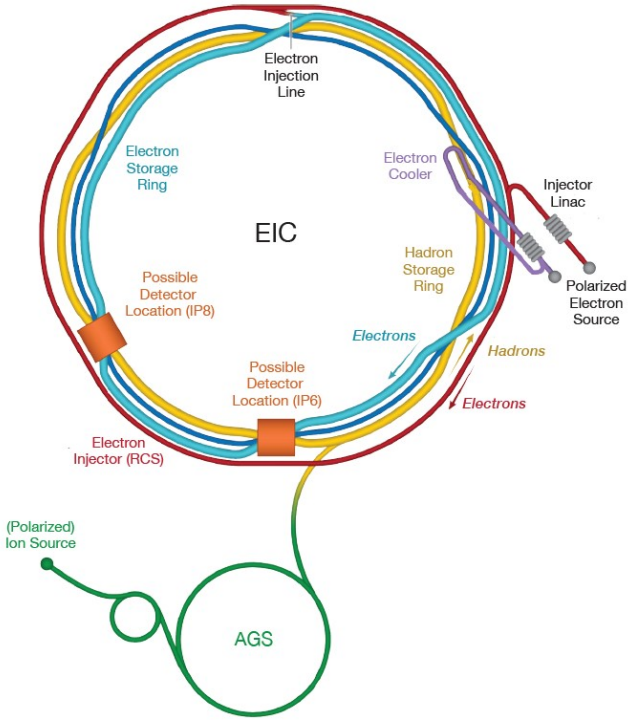

FIGURE 1.9: Schematic view of the accelerator system of the Electron Ion Collider from [23]. In yellow the hadron ring, in red the electron one. The two interaction points are visible.

This thesis is focused on the latter effort.
Finally, the hermetic detector measurements must be accompanied by precision measurements of beam luminosity and, in case of polarised scatterings, of beam polarisations. Dedicated detectors will accomplish this task.
The huge amount of data will be collected in a streaming readout approach, *i.e.* no trigger electronics is required. The single components of the detectors will be operated in a triggerless mode, collecting all the data without any event selection.

Chapter 2

Particle identification with Cherenkov imaging techniques

2.1 Introduction

In order to achieve the physics goals outlined in the previous chapter, the detectors at the future QCD facilities must be able to identify the species of the particles that emerge from the interaction. This capability is called Particle IDentification, shortened in PID, and is accomplished by the means of dedicated detectors.

PID can be performed by observing the peculiar way in which a species interacts with matter. It is the case of highly energetic muons, which, unlike other charged particles, have a very high penetrating power and can be detected after some absorbers that filter out any other particle. In a similar way, the difference in the development of a hadronic and a electromagnetic showers provides information on the nature of the mother particle.

However, when a species-specific interaction with matter can not be used as tool to identify the particle, the mass must be measured. A particle is univocally identified by its mass and its electrical charge [24]; the particle tracking in a suitable magnetic field provides the charge sign. The mass can be measured directly, if the particle decays and its decay products are detected, or indirectly, combining two of the these measured quantities: energy, momentum and velocity.

Practically the choice is restricted to the momentum and velocity [24]. Typically the measurement of deflection in a magnetic field performed by tracking detectors provides a measurement of the momentum $p = m\,\beta\,\gamma$, m, β and γ being the particle mass, its velocity and Lorenz factor, respectively. The velocity of the particle can be extracted using different techniques, such as the measurement of the energy lost in ionizing processes while traversing a material (which depends on β) or the time span between the interactions of the particle with detection planes placed at known distances (Time of Flight, TOF). Another possibility, if the particle is fast enough, is to extract the information on β from the measurement of the angle of emission of Cherenkov radiation (for a detailed description of this technique see section 2.2). The choice of the PID technique is primarily dictated by the particles momentum range and by the required separation power. The work presented in this thesis is focused on the detection of Cherenkov radiation .

If we combine the measurement of momentum with a measurement of β we obtain the mass of the particle as:

$$m = \frac{p}{\beta\gamma c} \tag{2.1}$$

The error associated to the mass can be expressed as:

$$\left(\frac{\sigma_m}{m}\right)^2 = \left(\frac{\sigma_p}{p}\right)^2 + \left(\gamma^2 \frac{\sigma_\beta}{\beta}\right)^2 \tag{2.2}$$

From equation 2.2 it is clear that for highly relativistic particles, the precision on β is the main contributor to the error on the mass, due to the γ^2 factor. To identify two particles of mass m_1 and m_2 respectively with the same momentum p one needs to determine their velocity, namely β_1 and β_2. The difference of the squared masses can be written as:

$$m_1^2 - m_2^2 = \frac{p^2}{c^2}\left[\left(\frac{1}{\beta_1\gamma_1}\right)^2 - \left(\frac{1}{\beta_2\gamma_2}\right)^2\right] \tag{2.3}$$

If the velocities are similar, $\beta_1 \sim \beta_2 = \beta$, then $\beta_1 + \beta_2 = 2\beta$ and $|\beta_1 - \beta_2| = \Delta\beta$. From equation 2.3 we can write:

$$\frac{\Delta\beta}{\beta} = \frac{(m_1^2 - m_2^2)c^2}{2p^2} \tag{2.4}$$

which express the required resolution on β. Distinguishing particles at high momenta requires very high β resolution. For instance, to obtain a 3σ separation of π and K at $p = 50\ GeV/c$ a $\Delta\beta/\beta$ of the order of 10^{-5} is required.

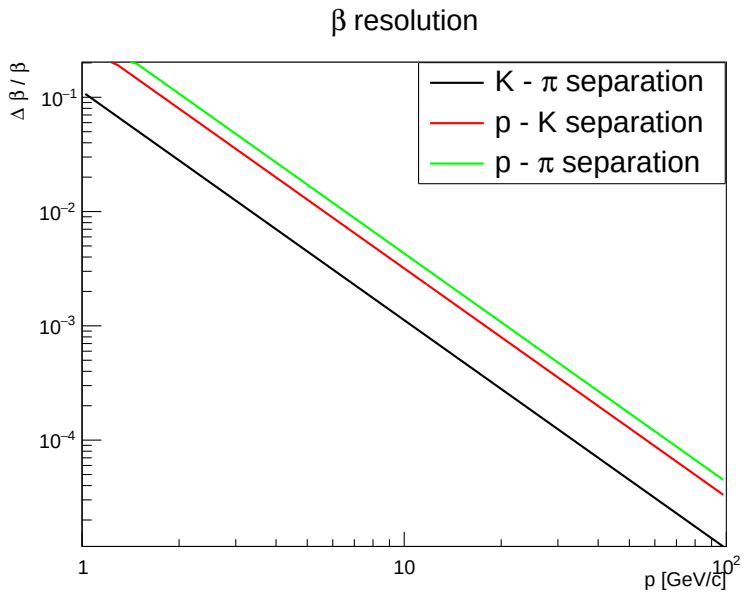

FIGURE 2.1: The β resolution required for distinguishing some hadrons in a momentum range between 1 GeV/c and 100 GeV/c.

2.2 The Cherenkov radiation

In the early 1930s, the Russian physicist Pavel A. Cherenkov studied the feeble visible light emitted by fluids traversed by radiation (β or Compton electrons liberated by scattering of γ rays) [25]. The observed light showed some unusual properties, such as insensitiveness to the action of quenching agents, anomalous polarization and marked spacial asymmetry, that could not be explained by the classical theory of luminescence. In fact, according to classical electromagnetism theory, a charged particle in a uniform rectilinear motion should not emit electromagnetic radiation; however, Cherenkov's observations were in disagreement with this expectation.

The experimental data were interpreted [25] as the radiation emitted by a charged particle traversing a dielectric material with a velocity v_p higher than the velocity at which the emitted wave propagates. In a dielectric material, characterized by its refractive index n, the phase velocity of the electromagnetic radiation is smaller than the speed of light in vacuum (c), being $v_{em} = c/n$. The refractive index n in general is not a constant, depending on the angular frequency ω of the radiation: $n = n(\omega)$. It is therefore possible that highly energetic particle crosses the dielectric medium with a velocity $v_p = \beta c$ higher that v_{em}. In traversing the dielectric, the charged particle temporarily polarises the atoms (or molecules) that lay in the proximity of its trajectory, creating electric dipoles. The dipoles created immediately relax emitting electromagnetic radiation that propagates in spherical waves with phase velocity $v_{em} = c/n$. If the particle is slow enough the waves emitted don't sum up in a coherent radiation and no light is observed. However, if the particle's velocity is larger than the phase velocity of light in the dielectric medium:

$$v_p = v_{em} \Rightarrow \beta c = \frac{c}{n} \tag{2.5}$$

the particle travels with the same velocity at which the waves it generates propagate. This means that every wave front of the emitted light corresponds to a new emitting point: the radiation is thus emitted coherently and the wave fronts sum up giving origin to a detectable radiation. The case of $v_p = v_{em}$ is the *threshold condition* for the Cherenkov radiation and corresponds to the emission of radiation in the direction of the motion of the particle. If $v_p > v_{em}$, the radiation is emitted with an angle θ with respect to the particle's track, with θ increasing for increasing v_p. With a simple geometric construction, portrayed in figure 2.2, it is easy to see that, for ($v_p \geq v_{em}$), the cosine of the emission angle θ can be expressed as:

$$cos\theta = \frac{1}{n\beta} \tag{2.6}$$

Equation 2.6 explains the asymmetry observed by Cherenkov. The cosine in the above equation can have any value between 0 and $+1$; the threshold condition $\beta = \frac{1}{n}$ ensures that $cos\theta$ is smaller than 1. Cherenkov radiation can be emitted at any angle θ between 0 and a maximum angle θ_{max}; θ_{max} is

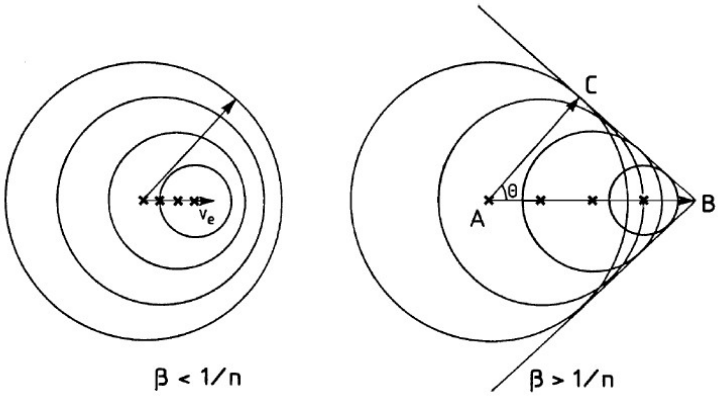

FIGURE 2.2: The Huygens construction of the wave front results in radiation propagating at an angle $\theta = arccos(1/\beta n)$ with respect to the particle track. The image is taken from [26].

reached for $\beta = 1$. This maximum, called *saturation angle*, depends on the dielectric through its refractive index and is calculated as:

$$cos\theta_{max} = \lim_{\beta \to 1} \frac{1}{n\beta} = \frac{1}{n} \tag{2.7}$$

The Cherenkov effect can be naively understood from figure 2.3. In the left figure the orientations of the dipoles at the front and at the rear of the track are symmetric: from a far distance the overall situation is neutral. On the other hand, if the particle is fast enough, like in the right figure, the relaxation of the dipoles, slower compared to the transit of the particles, leaves an asymmetric situation, where the dipoles front and back of the particle do not compensate in a neutral configuration. The emitted waves, then, sum up in a coherent radiation. A mechanical analogous phenomenon is the so-called "Mach cone", formed by pressure waves emitted by projectiles travelling at velocities higher than the speed of sound.

The particle loses energy in emitting radiation. The energy lost by a particle of charge e over a path of length L was calculated by Frank and Tamm [27] as:

$$W = \frac{e^2 L}{c^2} \int_{\beta n > 1} \omega d\omega \left(1 - \frac{1}{\beta^2 n^2}\right) \tag{2.8}$$

From the energy loss we can compute the number of photons emitted in a spectral region confined by the wavelengths λ_1 and λ_2; taking an average value for the the refractive index n:

$$N = 2\pi\alpha L \left(\frac{1}{\lambda_2} - \frac{1}{\lambda_1}\right)\left(1 - \frac{1}{\beta^2 n^2}\right) \tag{2.9}$$

where α is the fine structure constant. Equation 2.9 can be rearranged recalling the definition of the emission angle:

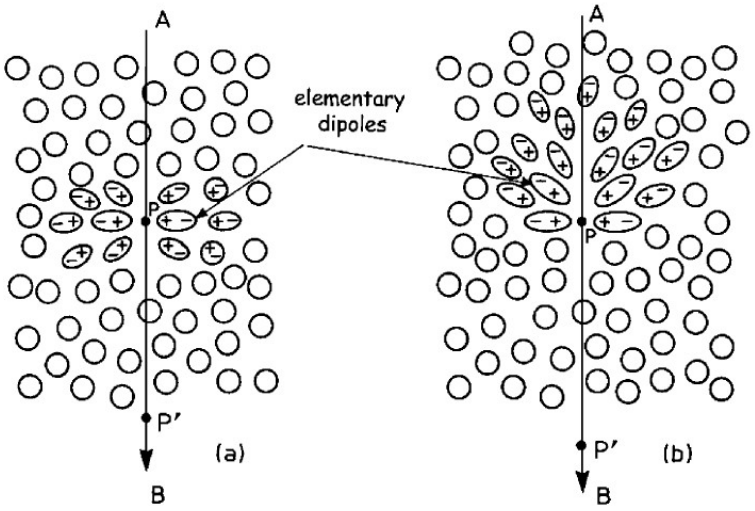

FIGURE 2.3: A schematic view of the dipole orientation in a dielectric traversed by a charged particle. If $\beta c \geq c/n$ the electromagnetic waves emitted by the relaxation of the dipoles sum up coherently resulting in the Cherenkov effect. The image is taken from [26].

$$N = 2\pi\alpha L\Big(\frac{1}{\lambda_2} - \frac{1}{\lambda_1}\Big)sin^2\theta \tag{2.10}$$

Cherenkov radiation is emitted only if the track of the particle in the radiator medium is longer than the wavelength of the radiated photons; otherwise, diffractive effects become dominant [26].

2.3 Detectors based on Cherenkov radiation

The Cherenkov effect described in the previous section and its unique features can be exploited for measuring different physical quantities of the emitting particle; the present thesis is focused on the Cherenkov-based particle identification techniques.

Since the emission angle of Cherenkov radiation is related to the particle's β, the information that a Cherenkov based detector can provide about an unknown particle is its velocity. In a beam of particles of the same momentum p, different particles will have different velocities and will emit Cherenkov radiation with different angles, provided their β is above threshold. In a focalised geometry, if we restrict the detection area, then, we will be able to detect only photons emitted at a particular angle, determined by the construction geometry. This is the operation principle of the *differential Cherenkov detectors* [28]. This detector family features a photon sensitive area restricted to a particular angle range $\Delta\theta$. The selection of a $\Delta\theta$ implies the selection of a $\Delta\beta$ band, which, for particle of the same momentum, means a positive identification of the particle species. Detectors of such a type have a small phase space acceptance and are used, for instance, to identify the particles present in a

beam. Figure 2.4, taken from [28], shows the operating principle of a differential Cherenkov detector: the Cherenkov photons emitted by the incoming particle are reflected to the photon detectors through a diaphragm, which means that they are detected only if they have the "right" β. A differential Cherenkov detector was used by Chamberlain and Segre in their experiment which led to the discovery of the antiproton [29]. With the magnets of the spectrometer they were able to select a precise momentum range, however, the yet to be discovered antiprotons were submerged by a huge background of mesons. The differential Cherenkov detector allowed Chamberlain and Segre to select a narrow band in β where they expected the antiproton.

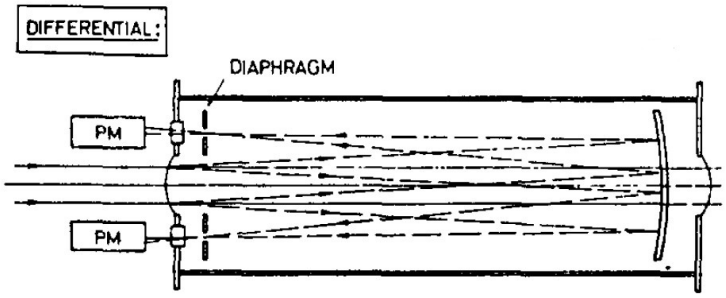

FIGURE 2.4: A schematic view of a differential Cherenkov detector; the image is taken from [28].

The fact that the radiation emission has a threshold in velocity might be used to distinguish between particles of the same momenta whose β are above and below threshold, respectively; the particle with β_1 such that $\beta_1 n > 1$ will emit Cherenkov radiation, while the other, at velocity β_2 for which $\beta_2 n < 1$ will not. Such kind of Cherenkov detectors are referred to as *threshold counters*. In a threshold counter the response of the detector is boolean, since the detector can only tell if the velocity was above or below threshold. Often a measurement of β, combined with a measurement of momentum p, suffices to identify the particle [30], however, an estimate of β can be obtained from the measurement of the pulse height, *i.e.* the number of detected photons. The success of threshold counters was due to their large phase space acceptance that matched the emittance of secondary particles produced in primary interactions [30]. A successful implementation of a Cherenkov threshold counter is the Fermilab experiment E691 [31] where two Cherenkov threshold counters were used for identifying hadrons in a momentum range of tens of GeV/c. The two RICHes were segmented in sectors; in each sector a Winston cone concentrated the collected light onto a photon detector (photomultipliers in this case). The presence of a signal in a specific sector and its amplitude were sufficient to identify the hadron traversing the radiator volume.

2.3.1 RICH

A differential Cherenkov counter can give good β resolution capabilities but its phase space acceptance is not suitable for identifying secondary particles produced in an interaction and distributed over a large phase-space domain. In order to overcome this limit, A. Roberts proposed a detector with an innovative exploitation of Cherenkov radiation [32]. A detector of this concept was built by T. Ypsilantis and J. Seguinot. [33].

The detector they built was composed by a spherical mirror of radius R_M (and focal length $R_M/2$) and a spherical detection plane of radius R_D. The space between these two spherical surfaces was filled with the radiator gas characterized by its refractive index n. A schematic of the geometry is reported in figure 2.5 [33]. The Cherenkov radiation described in section 2.2 is produced when a charged particle with sufficient velocity crosses the radiator material; photons are emitted at an angle $\theta_C = arccos(\frac{1}{\beta n})$ according to equation 2.6. The emitted photons are reflected backward to the detection plane by the mirror surface. Due to the geometry of the system, the photons will be focused at the same distance from the particle's track regardless of their emission point. Since Cherenkov radiation is isotropic in the azimuthal angle, the image formed on the detection surface will be a ring of angular radius θ_D, centered on the particle's track. If the detector surface corresponds to the focal plane of the mirror, *i.e.* $R_D = R_M/2$, the angular radius of the ring is equal to the the emission angle: $\theta_D = \theta_C$. From the measurement of the emission angle θ, the velocity β can be inferred. Since the projections of Cherenkov light cones appear as rings on the photon sensitive surface, the detector is called Ring Imaging CHerenkov, shortened in RICH. Such a detector is also called "focusing RICH" since the ring image is obtained by focusing the photons onto the detection plane.

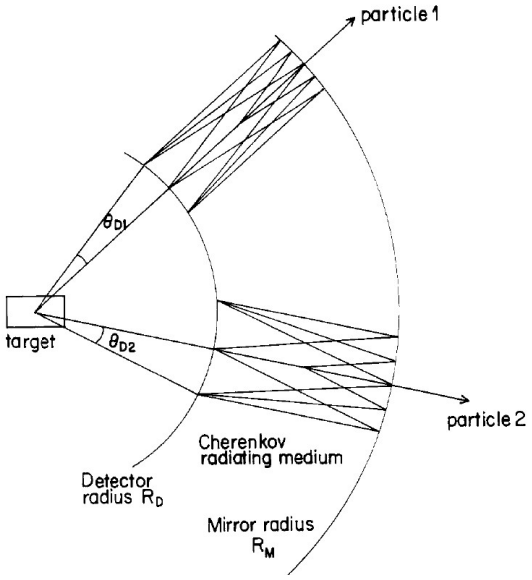

FIGURE 2.5: A schematic view of a RICH, taken from [33]. A detailed explanation is given in the text.

Detection of the Cherenkov photons

In order to reconstruct the Cherenkov ring, the photons emitted in the radiator must be localized [33]. Moreover, an ideal photon detector should have a large spherical surface with uniform sensitivity in order to accept all the ring images generated. Good time resolution and high quantum efficiency for photon detection are also required.

A photon detector will detect a number N of photons, which is different from the number of the total emitted photons derived in equation 2.10: some of them might be absorbed in the radiator or not be reflected by the mirrors. The number of detected photons is the convolution of the number of emitted photons with the quantum efficiency of the photon detector itself. Equation 2.10 was derived in a confined energy range but in general the transmittivity of the optical medium (ε_T), the reflectivity of the mirror (ε_R) and the quantum efficiency for photon detection (ε) are functions of the energy. Differentiating equation 2.10 with respect to the energy:

$$\frac{dN}{dE} = \frac{\alpha}{\hbar c} L sin^2\theta_C \tag{2.11}$$

The number of detected photons, then, can be obtained by integrating 2.11 in a range of photon energy, between E_1 and E_2.

$$N = N_0 L sin^2\theta_C \tag{2.12}$$

where the term N_0 includes all the energy dependent detector parameters:

$$N_0 = \frac{\alpha}{\hbar c} \int_{E_1}^{E_2} \varepsilon(E)\varepsilon_T(E)\varepsilon_R(E)dE \tag{2.13}$$

N_0 constitutes a figure of merit for comparing different Cherenkov detectors [33].

Nowadays different technologies can match the requirements outlined by T. Ypsilantis and J.Seguinot in [33]. Historically, the photon detectors proposed by the authors were based on gaseous detectors operated with a gas mixture enriched with a photoconverting vapour. Chapter3 will be dedicated to photon detection with gaseous detectors.

Choice of Cherenkov radiator

In the design of a RICH detector, as well as for other Cherenkov-based detectors, a key role is played by the choice of the radiator material [26]. The photon emission has a threshold in β (or analogously in γ). The threshold condition is met when $\beta_{thr} = 1/n$ or $\gamma_{thr} = n/\sqrt{n^2-1}$; note that the threshold depends on the refractive index of the dielectric. Since the intensity of Cherenkov radiation is smaller compared to the one emitted in typical scintillation processes, the radiator must not have appreciable scintillation properties. Obviously the radiator must be transparent to Cherenkov light in the selected wavelength range. According to the refractive index, radiators can be roughly grouped into four intervals [26]

- $1 < n < 1.12$ ($\gamma_{thr} > 2.147$) In this range radiators are gaseous, cryogenic liquids; the only solid material which has a refractive index in this range is silica aerogel, a very low density man made material.
- $1.12 < n < 1.35$ ($1.49 < \gamma_{thr} < 1.35$) In this interval radiators are liquid, mostly fluorocarbons.
- $1.33 < n < 1.47$ ($1.37 < \gamma_{thr} < 1.52$) Radiators in this interval are liquids transparent to visible and near UV light.
- $n > 1.46$ ($\gamma_{thr} < 1.37$) All the radiators in this range are solid. Owing to the high refractive index, Cherenkov photons might undergo internal reflection; this feature is important in the design of the radiator.

Figure 2.6 shows the angle of emission of Cherenkov radiation for different particle species in perfluorobutane, a typical Cherenkov radiator used, for instance, in COMPASS RICH [34]. For each particle threshold and saturation are clearly visible.

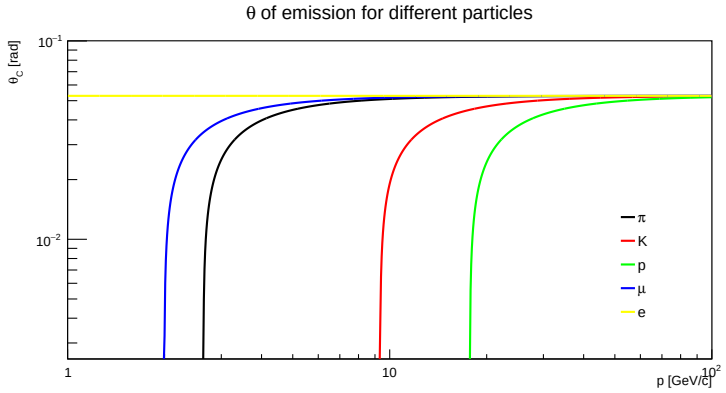

FIGURE 2.6: The emission angle (θ) as a function of the particle's momentum for different particle species in perfluorobutane (C_4F_{10}).

The dependence of the refractive index on the energy of the photon might affect RICH detectors by spoiling the angular resolution, in a context in which the precise determination of the Cherenkov angle is crucial, since it allows to reconstruct θ and hence β. The chromatic dispersion of the radiator, therefore, must be taken into account when designing a RICH detector. In figure 2.7, taken from [34], the refractive index of perfluorobutane, is plotted as a function of the wavelength. The ranges of COMPASS RICH photon detectors are indicated and will be discussed extensively in section 2.3.2. It is important to notice that the chromatic dispersion has a more severe effect at lower wavelengths, in the same range where the number of emitted photons is higher, according to equation 2.9: the compromise between chromatic dispersion and number of detected photons is a crucial point in the design of a RICH detector.

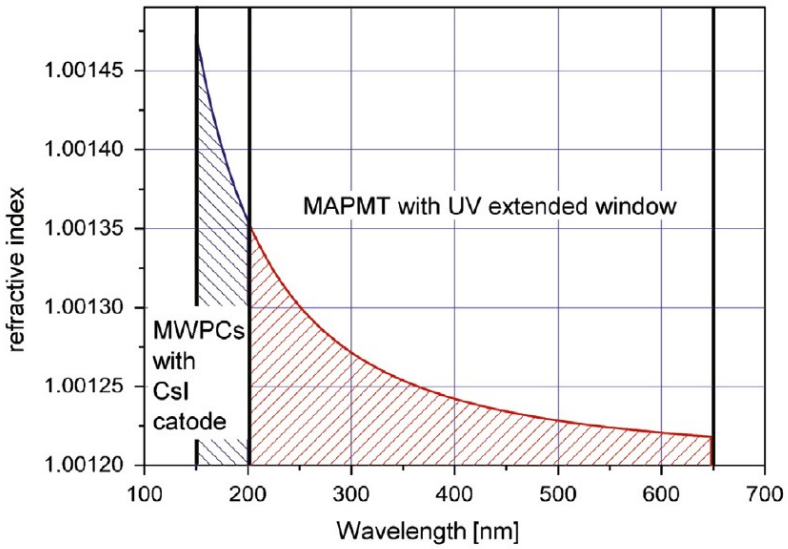

FIGURE 2.7: The refractive index of perfluorobutane as a function of wavelength. In the UV domain the chromatic effects are severe. The image is taken from [34]

2.3.2 A RICH example: the COMPASS RICH

In this section the COMPASS RICH will be described, in order to illustrate an operating example of the principles outlined in the sections above. Moreover, the technology developed for COMPASS RICH marks the starting point of the R&D project presented in this thesis. All the developments that are presented in the following chapters aim at extending this technology to other possible applications.

COMPASS experiment

In the wide physics programme of COMPASS, Particle Identification, is essential; a fundamental detector for identifying the particles traversing the spectrometer is COMPASS RICH [34]. A key requirement of the design of COMPASS RICH is a wide angular acceptance that matches the acceptance of the first stage of the spectrometer: 400 *mrad* in the vertical plane and 500 *mrad* in the horizontal plane, where the acceptance is increased to account for the trajectory bending by the first spectrometer magnet. A 3σ separation of hadrons up to a momentum of 50 GeV/c is required by spectroscopy studies and by the spin dependent nucleon structure studies via SIDIS measurements.

The radiator

The need for a large angular acceptance, combined with the distance of the RICH from the interaction point, explains the large horizontal and vertical dimensions of the vessel, roughly 5m $\times$ 6m. The high momentum range of

the particles coming form the interaction requires a gaseous radiator, as discussed in section 2.3.1, hence the path that particles traverse in the radiator must be adequate to ensure enough detected photons. In COMPASS RICH the particles traverse roughly 3m of radiator gas. The selected radiator is perfluorobutane (molecular formula: C_4F_{10}), a low chromaticity gas with a high refractive index: $n = 1.0014$ at λ = 400 nm. The Cherenkov emission threshold for different particles is plotted in figure 2.6. Figure 2.7 shows the chromatic dispersion of perfluorobutane, from [34]; in the picture two regions are highlighted, corresponding to the sensitivity region of COMPASS photon detectors. The pressure of C_4F_{10} is regulated relatively to the atmospheric pressure by the means of the recirculation system, that prevents also the formation of temperature gradients; this choice is imposed by the two vessel walls that lay in the spectrometer acceptance region, required to be thin in order to limit the amount of material. The evolution of the radiator gas pressure and temperature, related to the environmental conditions, results in a corresponding evolution of the gas refractive index, taken into account in the data analysis. Perfluorobutane is intrinsically transparent in the UV region, however, pollutants that might be present in commercially available gases degrade the transparency. Purity of the gas, is hence mandatory and it is achieved by the means of different filters, like activated carbon, activated copper and molecular sieve 3A, that remove the main photon absorbers in the UV range, aromatics, oxygen and water vapour.

The photon detectors

The Cherenkov photons emitted in the radiator gas are reflected by UV spherical mirrors onto two detection planes, as sketched in figure 2.8. The detection plane are out of the acceptance of the spectrometer and are separated from the radiator volume by fused silica windows, which are transparent to UV light. The large surface that needed to be covered with photon detectors imposed the choice of gaseous technology. In its original design the two detection planes were equipped with four Multi Wire Proportional Chambers (MWPCs) each. Photon sensitivity was ensured by a solid state photocathode made of CsI. Each MWPC was divided in two photocathode planes, resulting in sixteen photocathodes in total. For a detailed description of these detectors see chapter 3. Limitations due to ageing and event rate required a two-fold upgrade, based on dedicated R&Ds. The four central photon detectors were replaced by MultiAnode Photomultipliers and other four in the central region were upgraded with Photon Detectors based on Micro Pattern Gaseous Detector technology. MPGD based detectors, that represent the most recent upgrade of COMPASS RICH, integrate two different technologies and for this reason they are also called *hybrids*; they are thoroughly described in 3.

At present, COMPASS RICH features three different photon detection technologies, two of them are based on gaseous detectors and one on vacuum-based detectors. The combination of the three addresses the issue of having a cost-effective solution that matches the physics needs of the COMPASS experiment.

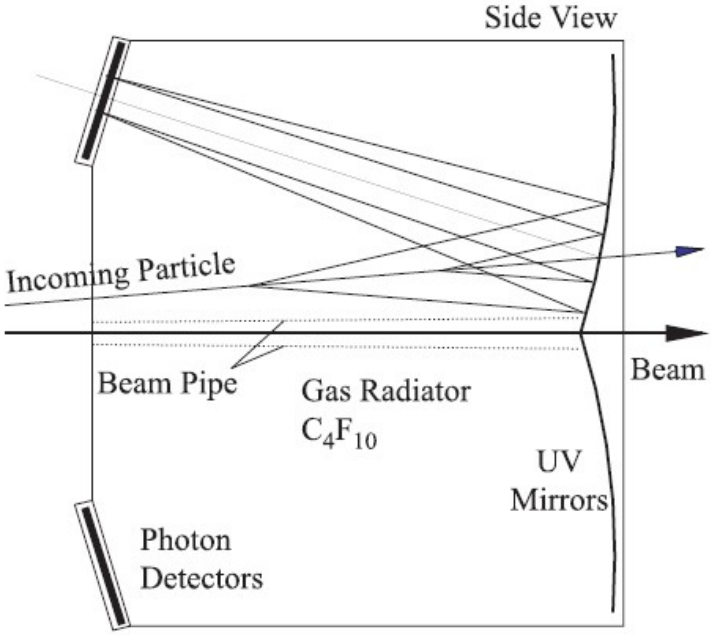

FIGURE 2.8: A schematic view of COMPASS RICH from the side. The spherical mirrors reflect the Cherenkov photons emitted by the incoming particle onto the photon detectors that lay outside of the spectrometer acceptance.

Chapter 3

Gaseous photon detectors

The detection of nuclear radiation is mediated by the transfer of energy to a medium[35]. Several microscopic processes can occur that imply the transfer of part of the particle's energy, or all of it, resulting in a detectable signal. In this chapter the principles of radiation detection with technologies based on charge multiplication in gases are outlined. The first section is a general introduction to gaseous detectors with a focus on the technologies that are relevant for the present thesis, the second section is dedicated to photon detection with gaseous detectors.

3.1 Radiation detection with gas

The operating principles of gaseous detectors rely on the microscopic interaction of radiation with matter. The interaction is species-specific and the case of photons and charged particles are treated separately.

3.1.1 Interaction of radiation with matter

The interaction of photons with matter occurs via several phenomena that depend on the photon energy as well as on the density and atomic number of the medium [35]. Unlike charged particles, photon do not lose their energy along their path but rather in single interactions with or without the creation of secondary particles. Gases are essentially transparent to visible and near UV photons, becoming opaque when the photon energy exceeds the threshold for inelastic interaction with atoms or molecules, that generally occurs in the far UV. The transition between transparent and opaque has a sharp edge for atomic gases, where the threshold is determined by the primary ionization energy, while for molecules radiationless absorption below ionizing threshold are possible due to mechanical excitations. For energies just above the threshold and up to few tens of keV, the dominant process is the photoelectric effect, that consists in the absorption of a photon and the subsequent emission of photoelectrons, whose energy equals the energy difference between the photon energy and the electronic levels. Along with the photoelectrons, cascades of lower energy photons and electrons are produced by the return of the atom to the ground state. The absorption cross section of photons has characteristic jumps for photon energies corresponding to new accessible electronic shells. For energies above few tens of keV the

probability of interaction drops and in this energy range gases are not used as detection media. In this energy range other processes, like Compton scattering and electron positron pair production, become dominant; since they are not relevant in the context of this thesis they will not be further discussed.

The largest fraction of the energy lost by a charged particle traversing matter is due to the electromagnetic interactions between the Coulomb fields of the projectile and of the molecules and atoms that form the traversed medium [35]. If the energy of the incoming particle is between a few and a few tens of eV, the presence of excited atomic states makes excitation the most probable process. Excitation modes are characteristic of the atom or the molecule and they generally increase in number for increasing molecule complexity. Excited species will return to their ground state via characteristic processes; in noble gases de-excitation generally occurs via a photon emission, while polyatomic molecules may return to their ground state via rotational and vibrational radiationless transitions. In practice, this property can be exploited by adding organic vapours to noble gases in detectors: they will dissipate energy without any γ or e^- emission.
For higher energy of the incoming particle the loss of energy in matter is mainly due to multiple inelastic processes ionization, whose probability is function of the energy itself. The energy loss due to excitation processes in gases results in a photon yield (luminescence and scintillation) too small in intensity to be practically exploited [35]. The energy loss per unit length decreases for increasing velocity of the particle till it reaches a minimum value. At β higher than the minimum a constant increase of energy loss per unit length is observed, the *relativistic rise*, which stabilizes the energy loss at a constant value, the so-called Fermi plateau. Fermi plateau can be 40 - 50 % higher than the minimum value for gases at moderate pressures, being smaller in condensed matter [35]. The energy loss per unit length can be parametrized using the Bethe Bloch formula:

$$-\frac{\Delta E}{\Delta x} = \frac{4\pi}{m_e c^2} N_A \rho \frac{Z}{A} z^2 e^2 \frac{1}{\beta^2} \left[ln\left(\frac{2m_e c^2 \beta^2}{I(1-\beta^2)}\right) - \beta^2 - \frac{\delta}{2} - \frac{C}{Z}\right] \tag{3.1}$$

Where N_A is the Avogadro number, e the electron charge and m_e the electron rest mass; I is the mean excitation potential.
Dependence on target material nature is included in the factor $\rho Z/A$, meaning that only the mass density makes up the difference in energy loss between different materials, if we assume that $Z/A \sim \frac{1}{2}$. Energy loss per unit length depends only on two properties of the incoming particle, its charge z, expressed in electron charge units, and its velocity, β.
The energy loss per unit length at low β has a steep decrease, proportional to $\frac{1}{\beta^2}$, then, after reaching the minimum, it slowly increases with a logarithmic growth at increasing β. In other words, a high velocity particle will lose little energy crossing a volume of matter. If it is slowed-down enough to enter the region where $-dE/dx \propto \frac{1}{\beta^2}$ it will lose its whole energy in a short range.
The logarithmic rise is smoothed by two correction factors. $\delta/2$, known as

density effect, becomes predominant at high energies: the electric field of the incoming particles, in fact, polarizes the atoms along its path, thus shielding distant atoms. It becomes relevant as energy increases, since for higher energies distant collision become more and more important. C/Z, the *shell correction*, arises when the the velocity of the incoming particle is comparable with electron velocity; it is therefore relevant at low energies.
The total number of electron ion pairs that is produced in ionization processes can be estimated as [35]:

$$N_T = \frac{\Delta E}{W_I} \tag{3.2}$$

where ΔE is the energy lost by the particle and W_I the average energy per ion pair which, for most gases, has typical values between 20 and 40 eV and depends little on the mass and energy of the ionizing particle [35].

At higher energy of the incoming particle other interactions dissipate the particle's energy: Bremsstrahlung, Cherenkov emission and transition radiation. However, with the exception of electron Bremsstrahlung, the contribution to energy loss is small [35].

3.1.2 Charge multiplication

The ionization process can be exploited for detecting the passage of radiation through a volume of gas. In an ionizing encounter a pair of objects with opposite charges is created; in order to use this charge separation to produce an electric signal, recombination must be avoided. A suitable electric field will drift the free charges, created by ionization, in opposite directions. However, in general, the signal of primary ionization is too low to be detected.
The electrons emitted in an ionization process, in presence of an electric field, can acquire enough energy to ionize other atoms or molecules. Ions, on the other hand, are too heavy to acquire the energy sufficient to ionize in typical conditions in which gaseous detectors are operated. The mean free path for ionization λ is the mean path that a particle travels between two successive ionizing collisions. If λ is small compared to the dimensions of the gas volume, many ionizing interactions can take place, resulting in an avalanche charge multiplication. The inverse of the mean free path for ionization $\alpha = \lambda^{-1}$ is the first Townsend coefficient and can be interpreted as the number of ion pairs produced per unit length. α can be expressed in terms of ionization cross section as $\alpha = N\sigma_i$, where N is the number of molecules per unit volume.
With a simple mathematical model the total multiplication factor can be estimated. If n is the number of pairs at a position x, then the increase in number of pairs produced (dn) in a path dx will depend on n and on the first Townsend coefficient as $dn = \alpha n dx$. The multiplication factor is the ratio between the number of electrons at an arbitrary position x_1 and the number of initial electrons.

$$M = \frac{n(x)}{n_0} = \frac{n_0 e^{\int_{x_0}^{x_1} \alpha(x)dx}}{n_0} = e^{\int_{x_0}^{x_1} \alpha(x)dx} \tag{3.3}$$

In general, the first Townsend coefficient is a function of the electric field, thus it may vary along the electron's track. Under the effect of the electric field, electrons and ions will drift in opposite directions. Due to the huge difference in mobility, the charges will propagate in a drop shaped distribution, with all the fast electrons in front and a tail of slow ions.
The size of the avalanche can not increase indefinitely. The presence of a high number of charges in the gas gap modifies the electric field, increasing it in the proximity of the avalanche. Photons that are emitted in the ionization process can further produce electron ion pairs that will trigger the formation of secondary avalanches. If the flux of charges is not dumped by the geometry or by a reduction of the field, it can propagate through the entire gas gap, leading to a spark breakdown. The maximum size of an avalanche that does not trigger a spark breakdown is given by the empirical Raether limit:

$$\alpha x < 20 \tag{3.4}$$

that means that the maximum achievable gain in a single avalanche multiplication is $\sim 10^8$. In practice, due to statistical fluctuations, the limit is about 10^6 [35].

3.1.3 Choice of gas

Charge multiplication may take place in every gas but not all the gases can be practically used in a detector. The ideal gas should allow high gains and low operating voltage. Due to the absence of rotational excited stated, in noble gases avalanche multiplication occurs at lower fields compared to complex molecules.
In noble gases, during avalanche multiplication process, ionized and excited atoms can return to their ground states via photon emission. These photons, hitting the metal electrodes, might extract a photoelectron that triggers a secondary avalanche. Secondary avalanches can be triggered as well by the emission of photons or electrons in the process of neutralization of ions at the cathodes. The presence of secondary avalanches prevents the operation of the detector at high gains.
Unlike monoatomic gases, polyatomic molecules can absorb photons in a wide energy range without being ionized, thanks to the presence of non-radiative excited states. The presence of such a gas, called *quencher*, in a mixture will allow, then, to reach high gains. Typical quenchers are organic compounds in the hydrocarbon and alcohol families and several inorganic compounds like CO_2 and CF_4; a common characteristic is the absorption of photons in the energy range of the emission by Ar, widely used for charge multiplication [35].
In order to increase even further the gain, a small percentage of an electronegative gas can be added to the mixture. Electronegative molecules will attach

the electron and form negative ions that will not start an avalanche. The presence of an electronegative gas allows gains of about 10^7 to be reached before discharge [35]; however, a large fraction of such a gas will eventually reduce the detector efficiency.

3.1.4 MWPC

Multiwire Proportional Chambers (MWPCs) were developed in late 1960s by G. Charpak. They consist in a plane of thin anode wires enclosed between two cathode planes. Typically the spacing between wires is three or four times smaller than the distance between wires and cathode planes. If the anode wires are grounded and the two cathodes are biased with the same negative voltage, the electric field is similar to the one shown in figure 3.1. At a large distance from the wires the electric field is constant, as it would be between two parallel electrodes. In this region primary interaction occurs and the electrons drift towards the wire. At a distance closer to the wires, the electric field is very intense, and can trigger a charge multiplication process that develops mostly in the last few mean free paths. The short space development of the avalanche ensures that the amplitude of the collected signal is almost insensitive to the position of the first ionization.

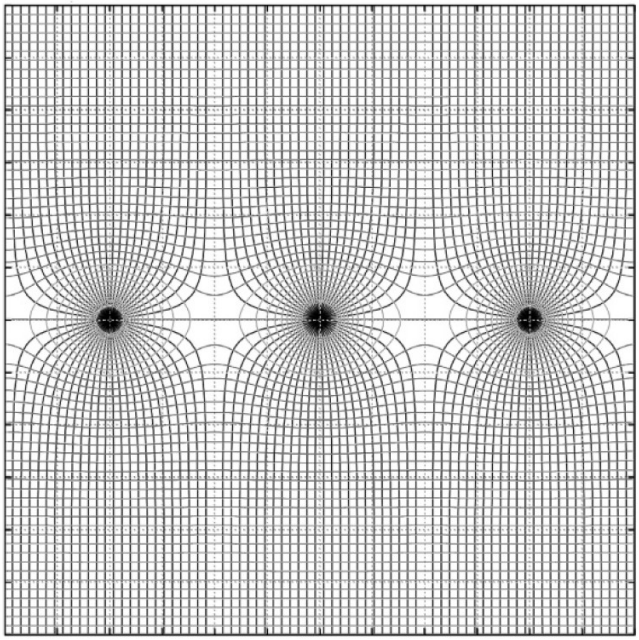

FIGURE 3.1: Field and equipotential lines in a Multiwire Proportional Chamber from [35].

3.1.5 MPGD

MWCPs have good performance and gave a fundamental contribution to particle physics. However, the challenging conditions of modern precision measurements put some limitations to their use, triggering the quest for new

gaseous architectures.
One of the most severe limit to the use of a MWPC is its rate capability that could not keep the pace with the increasing fluxes required at modern accelerator facilities. The rate limitation arises from the slow ion drift from the anode, where they are produced, towards the cathodes. If the incoming particle flux is high, positive charges will accumulate in the gap between anodes and cathodes, thus reducing the electric field close to the wires. For common wire chamber geometry, the gain drop begins at a particle flux around $10^4 mm^{-2}s^{-1}$ [36].
Several gaseous technologies were developed in order to overcome the limits of MWPCs. The manufacturing of these novel detectors made use of photolithographic or silicon foundry technologies both on rigid and plastic supports. A common characteristic are the narrow pitched anode electrodes that earned them the collective name of Micro-pattern gaseous detectors, MPGD. Many different micro-pattern detectors were conceived, manufactured and used; an exhaustive overview can be found in [36]. In the following sections only THGEMs and Micromegas are described since they constitute the elements of COMPASS hybrid photon detectors.

GEMs and THGEMs

The Gas Electron Multipliers (GEMs) were introduced in 1997 by F. Sauli [37]. The basic element of a GEM is a thin polymer foil metal coated on both sides. With photolithographic techniques holes are etched in the foil in a small pitched pattern - typical values for hole density are between 50 and 100 holes per square millimeter. Typical holes have a diameter of tens of μm and thickness of the same order of magnitude. In its basic design, the geometry is completed by drift and anode electrodes; the detector is operated in a gas mixture. A suitable choice of the voltages applied to the electrodes establishes a high electric field inside the holes, of the order of tens of kV/cm. Electrons created in the drift region by impinging radiation drift towards the GEM structure and enter the holes. Inside the holes the electrons acquire sufficient energy to cause secondary ionization of the molecules of the gas. Figure 3.2 depicts schematically the multiplication process inside the GEM holes. A sizeable fraction of the total charge exits the holes and is collected at the anode; many electrons, however, end at the bottom of the GEM: the result is an effective gain at the anode smaller than the maximum gain obtained in the avalanche. The signal at the anode is induced predominantly by the movement of the electrons, making the GEM a fast detector and largely overcoming the limitations due to space charge that affect MWPCs. The space sensitivity depends on the segmentation of the anode electrode, that can be patterned in strips or pads of various dimensions. With a single GEM foil gains above 10^3 can be easily obtained; however, high particle flux increases the discharge probability at lower gains. A common way to solve the latter issue is a multi GEM detector, where usually two or three amplification stages are chained.

The same geometric concept of GEM has been exported to a larger scale structure, the so called THGEM. The dielectric of a THGEM is thicker, typically hundreds of μm and holes are mechanically drilled. The resulting structure is rigid and can cover large areas without the need of a stretching frame. Holes might be surrounded by an annular region where the metal coating is removed: the presence of this rim allows to reach higher gains but reduces its stability since charges liberated in the avalanche process will accumulate in the dielectric region. The choice of the rim size (or of a no rim configuration) depends on the specific application. As for GEMs, a multi-THGEM structure reduces the discharge probability but in order to avoid the formation of large avalanches in single holes, which might lead to a discharge, the holes in two consecutive layers should not be aligned [34].

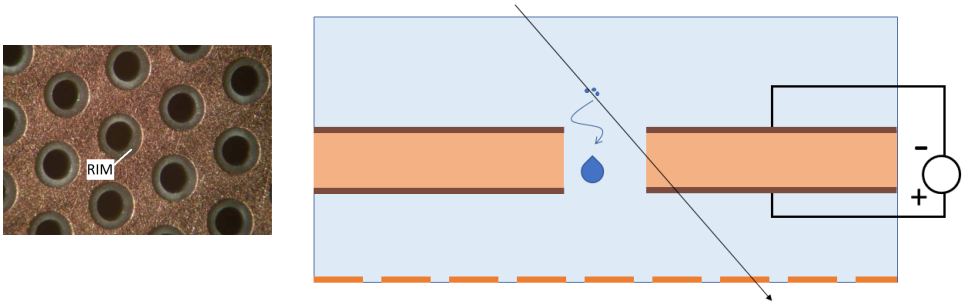

FIGURE 3.2: Left: image of a THGEM; the hole rim highlighted. Right: operating principle of a GEM/THGEM detector; primary electrons, generated from the interaction of impinging radiation with gas, are funneled through the holes where amplification occurs.

Micromegas

MICROMEsh GAseous Strucures, or in short Micromegas, were proposed by I. Giomataris in 1996 as fast detectors that could overcome the rate limitation of the MWPCs. The fundamental idea is to confine the avalanche development in a small gap close to the anode, so the slow ions will travel a reduced distance before being neutralized and the electric field restored. Typical gap sizes are of the order of 100 μm. A small amplification gap requires a larger volume where primary interactions with gas molecules occur; in this region a low electric field ensures the collection of primary electrons to the amplification gap. The two volumes are separated by a thin metallic mesh suspended above the anode plane by the means of dielectric pillars. Figure 3.3 shows the operating principle of a Micromegas detector. Mesh transparency to the passage of charge is determined by the ratio between the amplification and drift field. For high values of the ration E_A/E_D all the electron cloud is transferred to the amplification gap while most of ions get trapped by the mesh. Anode plane can be segmented in pads or strips. With a proper choice of gases, gains of 10^5 can be obtained.

Different technologies are available for producing a Micromegas. The Micromegas in COMPASS hybrids are of *bulk* type [34]. The manufacturing process of a bulk Micromegas [38] consists in laminating one (or two) layers of photoresist material, the mesh and another layer of photoresist on top of the anode electrode. The entire stack of material is exposed to UV light with a mask that let only the pillars become resistant to chemical etching. After UV exposure, a chemical bath washes out the non exposed parts; the resulting structure is, then, a mesh suspended and embedded in the dielectric pillars.

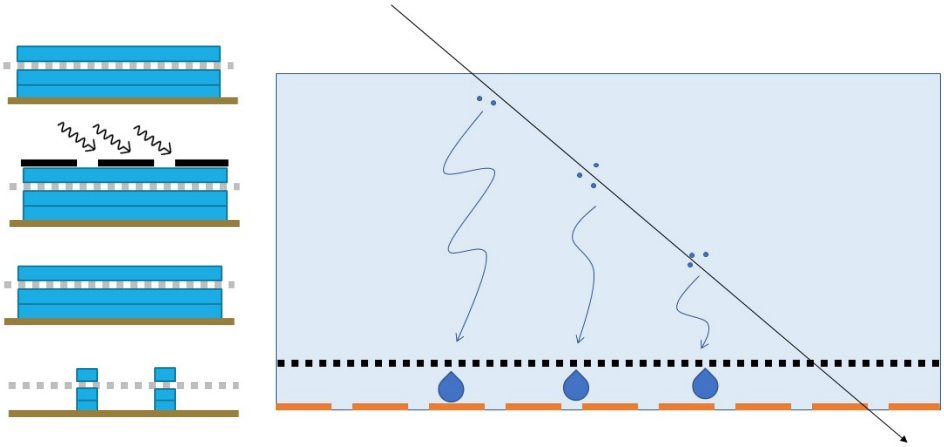

FIGURE 3.3: Fabrication of a bulk Micromegas (left): photoresist and mesh are laminated together on top of anode; pillars are obtained by chemical etching of non exposed photoresist. Operating principle of a Micromegas (right): primary electrons, generated from the interaction of impinging radiation with gas drift to the mesh after which amplification occurs

3.2 Gaseous photon detectors

Detection of photons for RICH application in large acceptance and wide momentum range requires to cover large surfaces with photosensitive detectors [39]. A cost effective solution, proposed along with the introduction of RICH concept is based on position sensitive gaseous detector operated with a mixture enhanced with photoconverting gases. In the early RICHes Triethylamine (TEA) was used as photoconverter; its ionizing threshold in the far UV (7.45 eV) required a window with a comparable transparency and MgF_2 was used. The later discovery of a vapour with ionization threshold as low as 5.5 eV, tetrakis dimethyl amino ethylene (TMAE), allowed the use of less expensive and more robust fused silica windows [40].
In order to detect the photons converted by TEA and TMAE, a position sensitive photon detector was required. MWPCs were suitable for covering large areas, however, the addition of photoconverting gases favoured the spread of discharges, due to the reconversion in the sensitive volume of the UV photons produced during the multiplication process. For addressing the

latter issues different solutions were adopted, such as MultiStep Chambers (MSC) [40] and Delphi MWPCs [41]. The usage of gaseous photoconverters required large volumes where the incoming photon could be absorbed, resulting in a sizable parallax error. Other limitations came from low rate capabilities, that made RICH detectors unsuitable for high flux applications. Furthermore, these gases required a delicate handling due to their explosive and corrosive properties. For these reasons, the use of gaseous photoconverters is today abandoned and will not be further discussed.

3.2.1 Photon detectors with solid photon converters

A solid state photocathode, on the other hand, has the advantage of surface photoconversion and emission, reducing parallax errors. Among the solid state photocathodes sensitive in UV range, Cesium Iodide (CsI) has high quantum efficiency over a considerable spectral range.

MWPCs with CsI

The MWPCs of COMPASS RICH are built according to the design optimized in the context of the RD26 collaboration at CERN [34]. The multiplication volume, filled with pure CH_4, is separated from the radiator by a fused silica window. Position sensitivity is given by one cathode plane, segmented in squared pixels with 8 mm pitch and coated with CsI: the incoming UV photon hits the cathode emitting an electron. The electron drifts towards the anode wires, with diameter 20 μm and 4 mm pitch, and starts multiplication. The chamber is completed by a plane of cathode wires, with diameter 50 μm and 2 mm pitch, placed between the anodes and the window. Front-end electronics is based on APV25 ASIC [42].
The APV25, originally designed for the readout of the CMS inner tracker, is a low noise, low power and radiation hard front-end ASIC. It is designed in 250 nm CMOS process. It has 128 readout channels, each consisting of a 50 ns CR-RC type shaping amplifier, a 192 element deep pipeline, used to store the amplified outputs, and a pulse shape processing stage. The amplitude of the shaped signal is sampled and the analog values are multiplexed onto a single differential output for subsequent optical transmission to the DAQ system. The output data frame consists of the analog samples preceded by a digital header which includes a digital address of the pipeline column from which the data originates. In COMPASS RICH APV25 ASICs are operated in *peak mode*: upon the arrival of an external trigger, one sample per channel is read from the pipeline (timed to be at the peak of the analog signal) and output through the multiplexer.

MPGD-based Photon Detectors

In 2016 COMPASS RICH was upgraded: four MWPC were replaced with MPGD-based PDs. The final architecture is the result of seven years of R&D

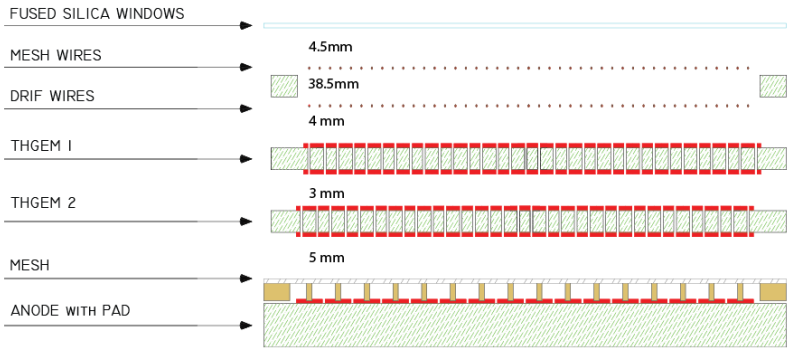

FIGURE 3.4: Sketch of COMPASS MPGD-based photon detectors; two layers of THGEM are followed by a Micromegas stage.

[34] and consists of two THGEM amplification stages followed by a Micromegas; the topmost THGEM is coated with CsI. 4 mm above the first THGEM a plane of wires allows to control the electric field and tune it in order to maximize the photon extraction. Each THGEM is made of 400 μm thick fiberglass where 400 μm diameter holes are mechanically drilled in a triangular pattern with 800 μm pitch; holes have no rim. THGEMs are staggered, in order to have a complete hole misalignment; the distance between the two layers is 3 mm. Each THGEM electrode is segmented and segments are powered via individual resistors: this powering scheme prevents discharges from affecting the whole detector and allow a fast restoration of the nominal voltage. The THGEMs are operated with a gain of about 10 each.
The final charge multiplication occurs in a bulk Micromegas; the mesh is made of woven stainless steel wires with 18 μm spaced by 45 μm. The mesh is suspended at 128 μm above the anode by a pillar array of 2 mm pitch. The mesh is the only non segmented electrode and is grounded. The gain of the Micromegas alone is tuned to be $\sim$ 100. Figure 3.4 sketches the structure of COMPASS MPGD-based Photon detectors. The anode plane is segmented in square pads with 8 mm pitch and 0.5 mm interpad clearance. The pad facing the mesh are positively biased via a individual resistor. Below each pad, buried under 70 μm of fiberglass lay the pickup pads, connected to the front-end electronics. A scheme of the pad structure with the equivalent electric circuit is shown in figure 3.5. This peculiar capacitive - resistive configuration prevents discharges from damaging the electronics. Read-out electronics is based on APV25 ASIC.
In order to ensure a stable gain over long periods voltages at the electrodes are adjusted according to pressure and temperature variations [43].
Hybrid photon detectors have been successfully operated during several years of data taking, showing good performance in terms of gain, around 13000, stability and reduction of Ion Backflow, that is as low as 3% [34].

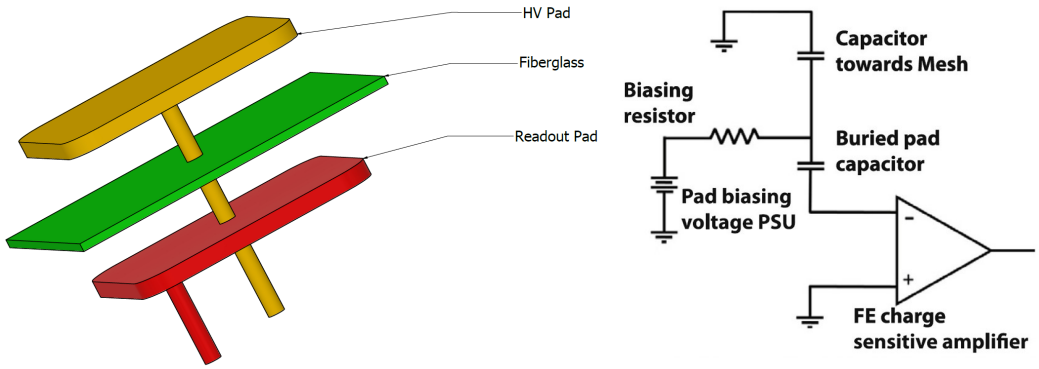

FIGURE 3.5: Pictorial view of the capacitive - resistive pad implementation (left) and its electrical equivalent circuit (right).

Chapter 4

Operation of COMPASS RICH-1

A RICH detector working in a physics experiment is a complex instrument that requires trained staff to be operated. In order to get familiar with a running system, much more complex than a laboratory desktop setup, I shared the responsibility of preparing and operating COMPASS RICH - 1 during transversity run 2021 - 2022. In the preparation phase, I had the responsibility of the radiator gas, which includes filling the radiator vessel and recovering the gas at the end of the data-taking period, making the radiator gas UV transparent as well as measuring its transparency. I measured also the transparency of the mixture used in the photon detectors. The latter task was achieved with the help of a dedicated gas mixing system that I built and operated; the same mixing system was later used to prepare the gas mixtures used in laboratory setups.

4.1 RICH filling and gas recovery

One of the main task that I was responsible for in COMPASS 2021 - 2022 run is filling the radiator vessel and recovering the radiator gas at the end of the data-taking periods. In order to avoid unnecessary perfluorobutane losses, during shutdown periods the radiator volume is filled with N_2; before each run nitrogen is replaced with perfluorobutane and at the end of each run perfluorobutane is recovered in the storage tank.

Figure 4.1 shows a schematic representation of the gas circulation system. In the filling procedure C_4F_{10} enters from a pipe in the bottom of the volume and from the top of the vessel a gaseous mixture of N_2 and C_4F_{10} is extracted. At the beginning of the filling the main component of the extracted mixture is N_2 while the percentage of C_4F_{10} gradually increases. The separation between the two components of the mixture is done in a cool cell where at a temperature of $-36^{\circ}C$ perfluorobutane condensates and flows to the storage tank, while the gas exceeding a user-defined pressure is vented out; values of the vent out valve can be chosen up to 7 bar. A little percentage of C_4F_{10} is unavoidably vented out; the choice of pressure and temperature values allows to keep it as low as a few percent only, typically around 3%. When the volume is completely filled the direction of injection and extraction of gas is inverted, the cool cell is switched off and evaporation and condensation to the storage tank are ensured by environmental temperature and pressure variations only. The recovery of the gas follows the inverse procedure: N_2

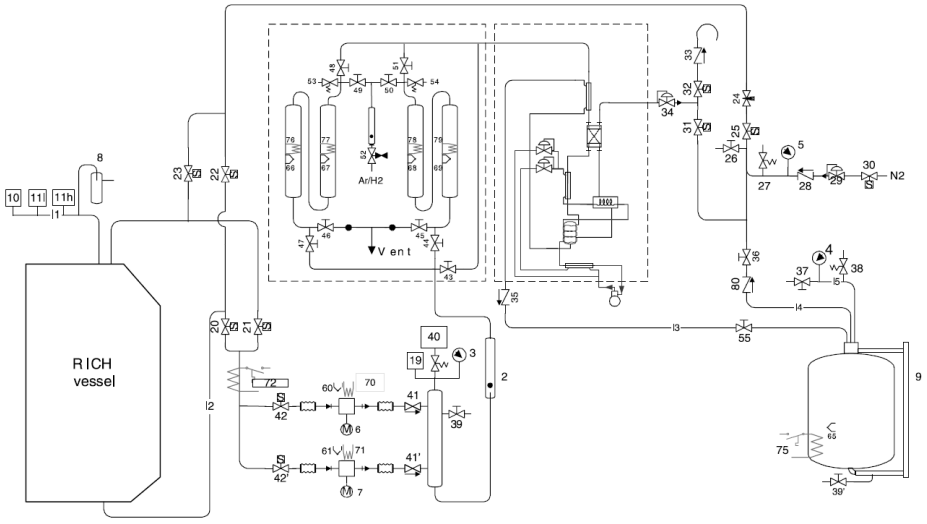

FIGURE 4.1: A schematic view of the COMPASS RICH gas system.

is injected from the top in the radiator volume and the recovered mixture is separated in its components in the cool cell: perfluorobutane is liquefied and stored in the tank while N_2 is vented out. The radiator gas fraction during both filling and recovery shows a characteristic exponential behaviour versus time, being completed in 4 - 5 days, depending on the speed of the compressors.

4.2 Transparency measurements

The photoconverter used in COMPASS RICH-1, CsI, is sensitive only to UV light. Therefore, we must ensure that the materials crossed by the photons, namely the radiator gas, the fused silica window and the multiplication gas, are transparent to UV light. The window has a wavelength cutoff of 165 nm, while the transparency of the gases, measured with a dedicated setup described below, mainly depends on the purity of the gas itself.

4.2.1 Transparency setup

A dedicated setup measures the transparency of a gas comparing it to the transparency of N_2, known to be transparent and assumed to be pure. A sketch that shows its operating principle is shown in figure 4.2. A monochromatic beam is selected using a diffraction grating that can rotate thanks to a motor; a fixed slit selects photons with a precision better than 1 nm. The obtained beam enters the T shaped gas volume and is split by a semitransparent mirror placed in the junction of the arms at an angle of 45 ° with respect to the light direction. The two beams travel along two arms with different lengths, having a different optical path, and hit two photomultipliers, one per each

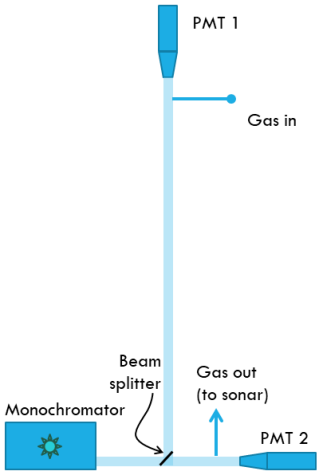

FIGURE 4.2: A schematic view of the setup used for measuring the transparency of gases. A UV light source is followed by a two arm gas volume; at the end of each arm a photomultiplier converts the impinging photons into a detectable current. The light in the two arms is split by a semitransparent mirror.

beam, whose current is measured. If the initial intensity of the photon beam is I_0, the intensity of the beam hitting each of the two PMT window, is:

$$I_i = I_0 \, c_i \, e^{-\mu x_i} \tag{4.1}$$

where x_i is the length of the arm, μ the absorption coefficient and c_i the coefficient of refraction or reflection, depending on the arm of the instrument. The ratios of the measured currents, subtracted by the dark current measured in each photomultiplier, gives:

$$R = \frac{I_1}{I_2} = \frac{c_R}{c_T} \, e^{-\mu(x_1 - x_2)} \tag{4.2}$$

that is the equivalent transparency of an optical length in the gas under test of $x_1 - x_2$ multiplied by the unknown quantity $\frac{c_R}{c_T}$. The technique adopted for cancelling the unknown term in equation 4.2 consists in measuring the ratio R for N_2, assumed to be transparent to UV photons, for which

$$R_{N_2} = \frac{I_1}{I_2} = \frac{c_R}{c_T} \, e^{-\mu(x_2 - x_1)} = \frac{c_R}{c_T} \tag{4.3}$$

since $\mu = 0$.The transparency of any gas is then evaluated as the ratio R divided by the same quantity measured for N_2.

$$T = \frac{R_{gas}}{R_{N_2}} = e^{-\mu(x_2 - x_1)} \tag{4.4}$$

In COMPASS setup, the length x_1 and x_2 are fixed at 13 cm and 200 cm, resulting in an optical path $x_2 - x_1 = 187$ cm.
The transparency plotted versus the wavelength gives information about

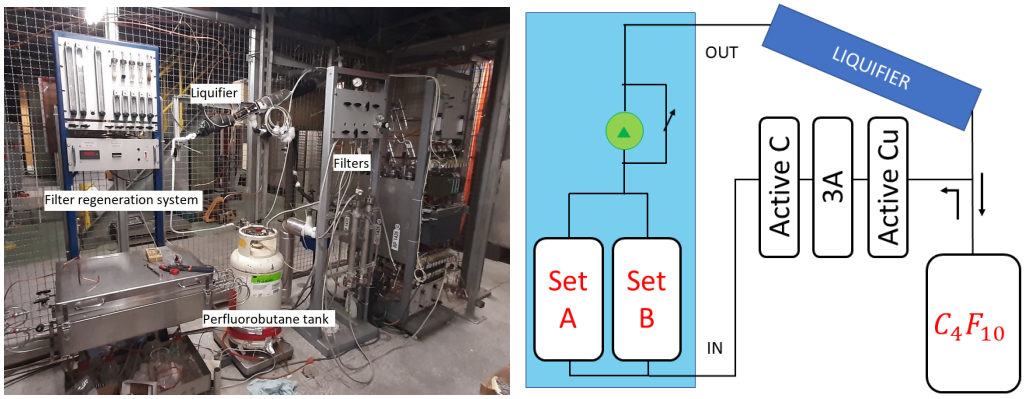

FIGURE 4.3: The cleaning setup (left) and its operating principle (right). In the picture some elements are visible, the filter regeneration setup, at the left, on the right the gas tank under the liquefier and more on the right the filters and the pump.

particular energies absorbed by the gas, thus revealing the nature of the contaminant.
The measurement is automatized and runs over a user defined wavelength range in user defined steps. The method of the double ratio cancels the dependence on the amount of emitted light because the two photomultipliers measure a fixed fraction of the generated light.

Perfluorobutane in COMPASS RICH vessel is recirculated in order to avoid the stratification of the residual N_2, the irreducible fraction corresponding to about 3% which cannot be separated from perfluorobutane, and to prevent the formation of temperature gradients. Moreover, recirculation allows a continuous filtering and a control on the pressure inside the radiator volume. Continuous filtering is needed to avoid building up oxygen and water vapour impurities related to air leakage in the vessel and gas system. Filtered perfluorobutane enters the top of the vessel and is sucked from the bottom by two oil-free compressors and stored, in liquid phase, in a tank. The compressors run at fixed rate, typically 2.5 m^3/h. Following pressure variations, more or less perfluorobutane is sucked, in gaseous phase, from the tank via a pneumatic valve, whose opening is automatically regulated on the basis of the relative pressure inside the vessel. The pressure inside the vessel follows the atmospheric pressure and is kept at 1.0 ± 0.1 *mbar* above it. The operation of such a large system, however, unavoidably introduces some losses and further amount of perfluorobutane must be supplied every few years. The need for COMPASS 2021 - 2022 run was estimated to be about 350 *kg* of perfluorobutane. The gas as received from the producers could not be used in COMPASS RICH due to the presence of contaminants that reduce significantly its transparency. The gas had, then, to be filtered with a dedicated setup. I operated the setup outlining a procedure that minimizes the gas losses.

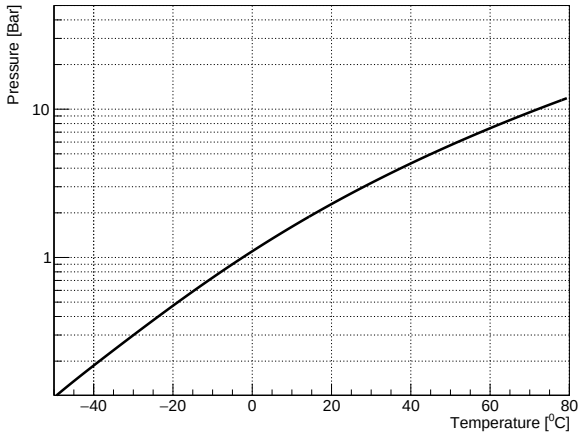

FIGURE 4.4: Phase diagram of perflurobutane, the radiator gas of COMPASS RICH-1; at atmospheric pressure it liquifies at about -1° C.

Perfluorobutane was supplied in a large tank ($\sim$ 1000 L); since the pressure of the gaseous phase is too high for the cleaning setup, perfluorobutane was spilled in smaller tanks; in each tank two knobs allow to access both the liquid (at the tank bottom) and the gaseous phase (at the tank top) of perfluorobutane. The cleaning system circulates the gas in a closed loop: perfluorobutane is extracted from the gaseous phase knob and passed through different filters. The activated carbon filters the hydrocarbons present in the gas and the molecular sieve 3A captures the water vapour. In the original design, oxygen is removed in a cold section (T = - 60 °C) where C_4F_{10} condensates - its boiling point is around -1°C - and the liquid drops return to the bottle; at such a temperature oxygen is in gaseous phase - its boiling point is around T = - 183 °C - and is vented out. A small fraction of perfluorobutane is in gaseous phase and is vented out along with the oxygen; to avoid these losses I added an activated copper filter that removes oxygen without major gas losses. In the modified setup, the filtered gas is cooled with liquid N_2 till it reaches the liquid phase and is fed into the tank. A valve placed before the filters connects the cleaning system to the setup described in 4.2.1, so that transparency can be monitored during the cleaning procedure at the price of a small loss: in fact, the gas that flows out of the transparency setup is vented out. Once the transparency has reached the required value ($\geq$ 95% over the whole wavelength range), the recirculation through the filters is stopped and the gas is fed into the RICH storage tank.
Accumulating impurities, filters reduce their capability to filter and need to be regenerated. Regeneration of active carbon and molecular sieve is done at high temperature (200°C) with a continuous flow of an inert gas, Ar. Regeneration of active copper, on the other hand, requires to cleave the oxygen - copper bonding to create water vapour that can be flushed away; this is done by flushing the filters with ARCAL, a mixture of Ar and H_2 in 98 : 2 ratio, at high temperature (200°C). The regeneration procedure results in the

loss of all the perfluorobutane that is contained in the filters; small filters contain less perfluorobutane but must be regenerated more often; however they have the advantage of minimizing the amount of perfluorobutane in liquid phase, reducing the total losses. The new procedure that was outlined makes use of smaller filters compared to the ones that were used in the previous years and allows to reach high cleaning efficiency $\geq$ 95%, to be compared with previous efficiency of $\sim$ 70%.

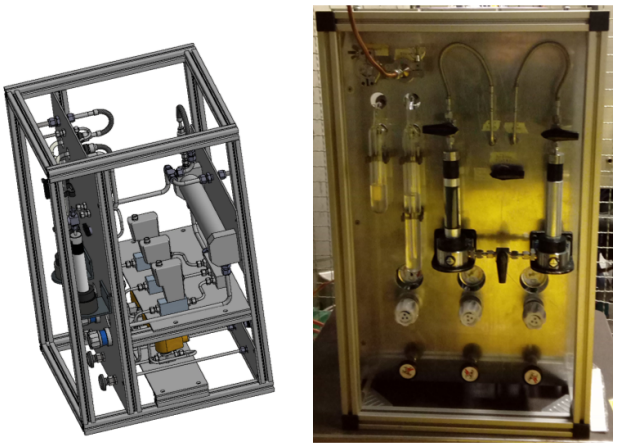

FIGURE 4.5: Design of the gas mixing system and front view.

4.2.2 Gas mixing system

UV photons produced via Cherenkov effect should not be absorbed in the gas mixture of photon detectors, therefore the transparency of the gaseous mixture must be measured. The gaseous mixture used in COMPASS hybrid photon detectors is made of CH_4 and Ar in volumetric proportion of 50% : 50%, while pure CH_4 is used for the MWPCs. The presence of methane, however, prevents the measurement of the mixture in our transparency setup, since it would not comply with the safety rules of CERN. For performing the transparency measurement a new gas mixing system was designed and built using ATEX compliant components; since it can mix also non explosive gases, the system was later used for other laboratory measurements.

In order to ensure a safe use, the system must be operated from remote; the percentage of methane in the mixture must be always monitored and in case it exceeds the explosive limits (4.4% for methane in air), a fast shut down of the lines must stop the system, triggering an alarm.

The gas mixing system is a compact object (45 cm $\times$ 47.6 cm $\times$ 74 cm) with three gas input line and one output line. At the entrance of each line an ATEX compliant solenoid valve (normally closed) allows or blocks the gas flow to the system. The solenoid valves are remotely controlled via a NI USB 6501 board. After the solenoid valve, a manual pressure reducer in each line sets the pressure of the gas. The remote control of gas flow in each line is provided by a mass flowmeter of the Bronkhorst in-flow series, in series

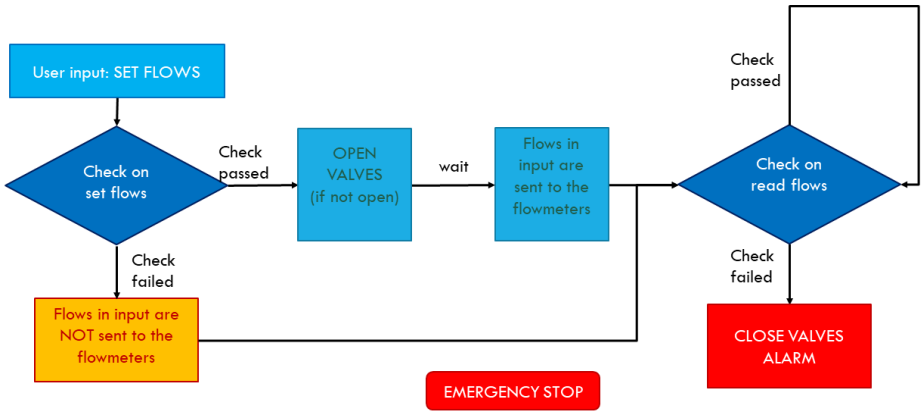

FIGURE 4.6: Flowchart illustrating the operating principle of the gas mixing system control software. The core is a continuous check of the concentration values; a further check prevents the user from setting *not allowed* mixtures while an emergency stop button can be pressed at any time stopping the gas inputs.

after the valves, that sets and measures the flows; the three flowmeters communicate via RS232 serial cables. Two flowmeters have a dynamic range of $0.6 \div 30\ L/h$, while the third one, used for CH_4 has a dynamic range of $0.1 \div 5\ L/h$. The flowmeters are followed by the mixing volume, a metal cylinder of about $\sim 1\ L$ where a serpentine on the gas path mixes the gases: from this point the mixture is surely non explosive. The system is equipped with two filters, Oxysorb, for filtering out oxygen and Hydrosorb, for filtering out water vapour; the filter set can be bypassed. Finally, a safety bubbler controls the pressure at the output line. The system is completed by a return line that contains a return bubbler and drives the mixtures to an exhaust connector.
All the communication cables are plugged in a box where a USB hub manages the communication with the control computer via a single serial cable. The operation of the system is managed with a dedicated software written in LabView2020 that runs on the control computer. A flowchart of the software operation is shown in figure 4.6: a continuous check runs on the values read out by the flowmeters once per second and controls that the percentage of methane is smaller than the 4% of the total mixture (explosive limit is 4.4%). If the error condition is encountered, the solenoid valves kill the flow and an alarm is triggered. In order to restore working conditions, *i.e.* open the solenoid valves, a button on the box must be pressed and the software restarted. A preliminary check on the user-defined values prevents from selecting a mixture with a concentration of methane higher than 4%.

4.2.3 Methane transparency

A fundamental measurement for the preparation of COMPASS 2021 - 2022 run was the measurement of the transparency of methane in the UV range.

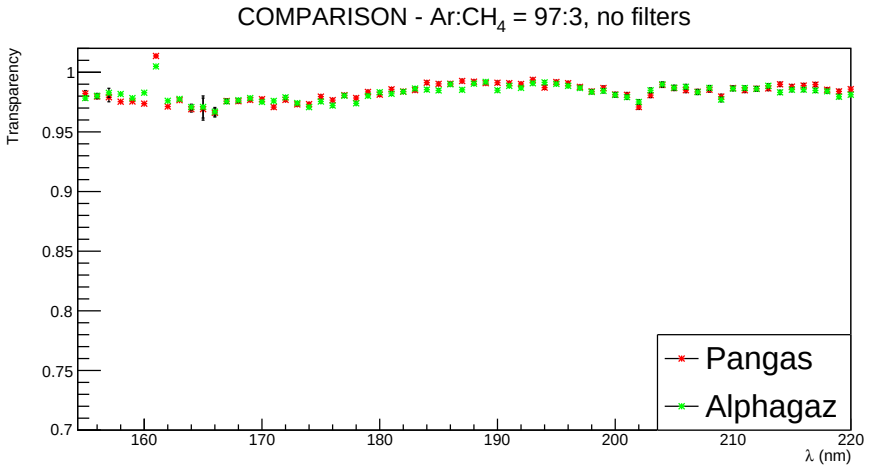

FIGURE 4.7: Result of the comparison of transparencies measured for mixtures of nitrogen with ALPHAGAZ methane (green dots) and PANGAS methane (red dots). Transparency is $\sim$ 97% over the whole wavelength range.

In fact, CERN had changed the gas supplier from ALPHAGAZ to PANGAS. The quality of the methane delivered by the new company had to be checked. The measurement was performed using the instrument described in subsection 4.2.1. The test mixture contained N_2 and CH_4 in proportion 97 : 3, that corresponds to an optical path of $\sim$ 5.6 cm, roughly the thickness of the Photon Detectors. The whole experimental setup was checked by CERN safety staff and permission to run the measurement was given. A sample of methane from each company was delivered in a small tank. The transparency setup was flushed with an amount of N_2 equal to several times the volume of the setup itself and transparency was measured. Then ALPHAGAZ tank was connected to the input of the mixing system and the methane-rich mixture was flushed for the equivalent of 6 times the volume of the setup in order to be sure that the mixture present in the volume is the desired mixtures. For the first measurement the gas mixture was passed through the filters, later filters were bypassed. Once the transparency was measured, the system was cleaned by flushing the equivalent of several setup volumes (more than 100) and the same procedure was repeated with the PANGAS tank.
Figure 4.7 shows the comparison of the transparencies in the two gases, PANGAS in red and ALPHAGAZ in green. The values are in good agreement, being around 97% over the whole wavelength range. PANGAS methane was then validated and used in 2021 - 2022 run.

Chapter 5

Front-end electronics: VMM

The MPGD-based photon detection technology developed for the COMPASS RICH1 can not be exported, coupled with its electronics, to an experimental setup at the Electron Ion Collider. In fact, the readout electronics, based on the APV25 front-end ASIC, works only in triggered mode and it is not compatible with the planned streaming readout approach. Therefore, a new front end ASIC must be coupled to the detector. The requirements a front-end ASIC must satisfy are, naturally, a trigger-less operation and good performance in terms of signal to noise ratio, since signals generated by a single initial photon (and, hence, a single initial photoelectron) are small.

5.1 VMM

VMM is a custom ASIC designed at Brookhaven National Laboratories (BNL), produced in the 130 nm Global Foundries 8RF-DM process [44]. The device is packaged in a Ball Grid Array (BGA) with outline dimensions of 21 $mm \times$ 21 mm. The main physics drive for the project is the readout electronics of the ATLAS New Small Wheels (NSW) [45], a large complex of detectors that include Micromegas and small strip Thin Gap Chambers (sTGC). The Micromegas - specific design makes the VMM a good candidate for COMPASS-type MPGD-based photon detectors. Unlike the Micromegas of the ATLAS NSW, the anode of COMPASS-type photon detectors is segmented in pads. The chip version studied in the present thesis work is VMM3a.

5.1.1 The chip architecture

A detailed description of the VMM architecture can be found in [45], which is the main source for most of the information outlined in this section. The VMM is made of 64 linear front-end channels; figure 5.1, taken from [45], shows a block diagram of one of the 64 identical channels. Each channel integrates a low noise charge amplifier with adaptive feedback, test capacitor and mask option. The input MOSFET can be configured for accepting either positive or negative polarity. The gain is adjustable in eight values: 0.5, 1, 1.5, 3, 4.5, 6, 9, 12, 16 mV/fC. The signal is shaped by a third order filter, referred to as *shaper*, with one real pole and two complex - conjugate poles, in Delayed Dissipative Feedback (DDF). The shaping time can be set at four values: 25,

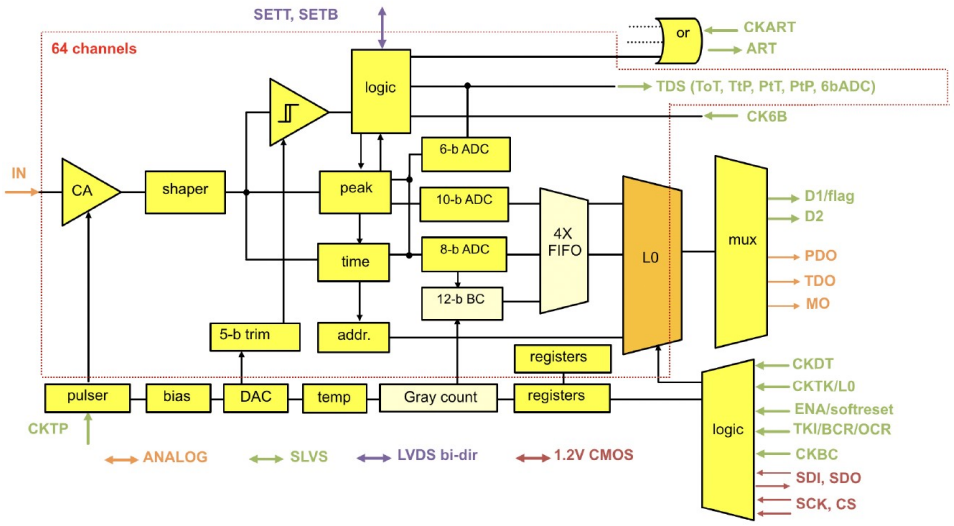

FIGURE 5.1: The architecture of one of the 64 identical channels of the VMM. The picture is taken from [45].

50, 100 and 200 *ns*. The shaper is followed by a sub-hysteresis discriminator [46]. A global threshold is set with a 10-bit DAC, while in each channel a 5-bit threshold trimming logic takes into account the fluctuations of the baselines in each channel. A neighbour-enabling logic allows the digitization of signals below threshold if a hit is found in one of the nearby channels; the neighbouring logic can be extended to other chips via bidirectional input - output line. This powerful feature, designed for a strip readout, can not be used in a pad - segmented anode and is not exploited in the described setup. The peak amplitude is measured by the peak detector and stored in an analog buffer. The time is measured with a Time to Amplitude Converter (TAC): a signal starts ramping up either at peaking time or at threshold crossing,upon user's choice, and is stopped at the clock cycle of the Bunch Crossing clock (CKBC), provided externally; the resulting amplitude is digitized.
In each channel three ADCs are implemented. A 6-bit, single stage ADC converts the peak amplitude into a digital word that is available at the serial direct output of the channel. The other two ADCs (10-bit and 8-bit) are current mode, two stages ADCs; the 10-bit ADC digitizes the peak amplitude while the 8-bit one the time through the TAC. In both ADCs the analog currents are compared, at the first stage, with few current levels flowing in *macrocell circuits*; the upper (coarse) bits are determined in this way. A precise comparison within the selected macrocell determines the lower bits, reaching the nominal precision.
The VMM includes a test pulse generator connected to the input capacitors of each channel. The pulse is triggered by an external signal and its height can be adjusted in 1024 values with a 10-bit DAC. The ASIC has also a temperature sensor and a band gap reference circuit. The VMM integrates an analog output that allows the monitoring of baseline and shaped pulses in each channel as well as some global features like threshold, test pulse, band

gap reference voltage and the readout of the temperature sensor.

5.1.2 Read Out Modes

The VMM can be read out essentially in three modes [45]. The *two-phase analog mode* consists in two steps, acquisition and readout. In acquisition phase the signals are processed and the analog values of peak and time detectors are stored in an analog buffer. Once the acquisition is completed, the VMM can be switched to the readout mode. In the readout mode, the analog values are available at Pulse Detector Output (PDO) and Time Detector Output (TDO), while the address is serialized in 6 bits.

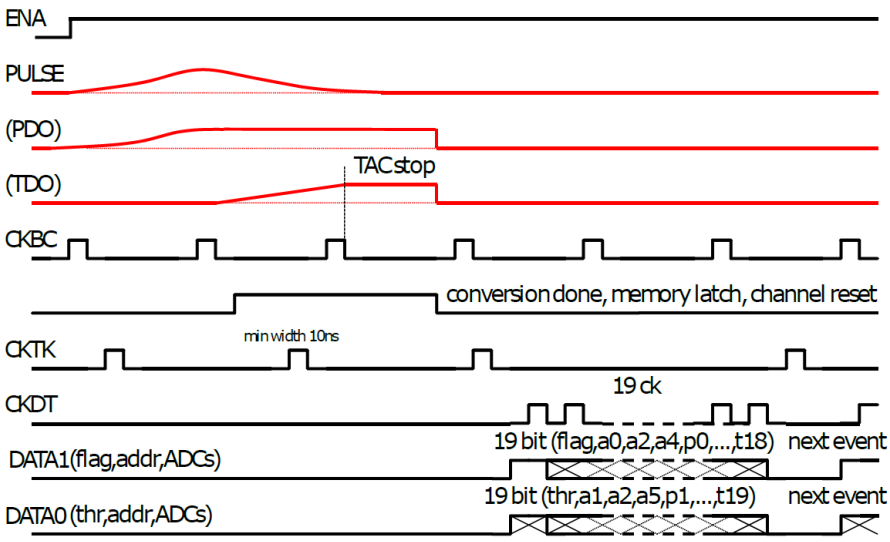

FIGURE 5.2: A timing diagram of the continuous readout mode. In red the analog values of the pulse, and the Pulse Detector Output (PDO) and the Time Detector Output (TDO) that will be digitized. Once the conversion is done, baselines are restored and digitized data are transmitted via the two data lines

The *continuous (digital) mode* is the working procedure adopted for the present thesis; a timing diagram is shown in figure 5.2. In this mode the pulse detector output and the time detector output, converted in currents, are driven to the ADCs. The pulse detector output can be digitized in the fast 6-bit ADC or in the more precise 10-bit ADC, the latter being used for the present thesis. The TAC stop signal occurs at a next clock cycle of a shared 12-bit Gray-code counter which is incremented using the external clock signal CKBC. The counter value at the TAC stop time is latched into a local 12-bit memory, thus providing a total of 20-bit deep timestamp with a nanosecond resolution. The channel is reset once both pulse and time conversions are completed and the digital values are latched in digital memories. The channel self resets provide continuous and independent operation of all 64-channels. Thus, in continuous mode a word of 38 bits is generated for each

event. The first bit is a readout flag, followed by a threshold crossing indicator that states whether the conversion was triggered by a signal above threshold or by the firing of a neighbouring channel. The following 6 bits store the channel address, while other 10 the signal amplitude; the last 20 bits are associated with the time. The 38-bit word is stored in a 4-event deep FIFO, accessible by the external electronics via two serial data lines.
The third readout mode, the *Level-0 mode*, is designed specifically for being compatible with ATLAS trigger [45]. The acquisition is analogous to the continuous digital mode described above, however the readout is different. All the events are temporary stored in a 64-event deep FIFO. In each channel, upon the arrival of an external trigger, a selector circuit selects only the hits within the timing window configured. An "event builder" circuit combines the BC information and the digitized values of the events selected by the trigger.

5.1.3 Fast Direct Outputs

Along with the described readout modes, two additional modes can be used to get a quick response from the detector. The *Address in Real Time (ART)* gives the digitized address (6 bits) of the first channel with the earliest registered hit within a BC clock. A flag is released at the ART output either at threshold crossing or at peaking time, according to user's choice; the flag is followed by the address of the event.
Each channel includes a Direct Digital Output (DDO). The 6-bit output can be either a coarse digitization of the peak amplitude or one of the following time information: time over threshold, threshold to peak, peak to threshold or a 10 *ns* pulse occurring at peak.

5.2 MMFE1 evaluation board

A front-end board is used to read out the signals of the detector with the VMM ASIC. The front-end board present in Trieste Laboratory is a MMFE1, designed for prototyping and tests of the VMM [47]. The board, powered with a DC voltage between 3.4 V and 42 V, provides the correct biases to the ASIC. The signals collected picked up at the detector anode are driven to the input of the charge amplifiers of the VMM through a Panasonic P5K connector, that housed 128 pins in 0.5 *mm* pitch; since the board has only one VMM, 64 pins of the connector are not used.
The core of the MMFE1 board is a Xilinix Artix 7 FPGA. The FPGA hosts a firmware capable of reading-out, configuring and calibrating the ASIC; the firmware, written primarily in VHDL, interfaces the on-board VMM and the software. It gives also the possibility to work in combination with other boards, although this feature is not exploited for this thesis. The firmware generates the Bunch Crossing clock (CKBC) and the test-pulse signal (CKTP). The CKBC is used as the VMM's reference clock, while the CKTP is driving the VMM internal test pulser. The test-pulse strobe is generated by the FPGA

FIGURE 5.3: The front end board MMFE1. In the lower part the VMM ASIC is visible, while the FPGA is under the cooling fan. The connector to the detector is on the back side.

synchronously to the CKBC. The reference clock source may be the on-board oscillator or an external common clock source.
The FPGA supports all the readout modes; the readout cycle starts with a trigger signal either from the internal CKBC/CKTP generator or from an external source. The Artix 7 is equipped with a 12-bit ADC, that is driven by the VMM analog outputs. The ADC is used either for the readout in dual phase mode or for calibrating the threshold and the pulser DAC. Another fundamental use of the ADC is sampling of the analog output to estimate the noise level(see 5.3.2).
The communication between the FPGA and the data acquisition (DAQ) and control computer, managed via Ethernet cable, is controlled by a dedicated software, *verso*[1]; a description of the software is presented in section 5.3.
The MMFE1 board also provides physical access to the ART, PDO, TDO and Monitoring Output (MO); these values can be measured with a tester or an oscilloscope. Particularly useful for the present thesis is the Monitoring Output which allows, selecting the VMM registers correctly, to access the analog values of each channel or some global properties like threshold value, test pulse height, band gap reference voltage or temperature sensor readout. Since the settings of the VMM registers might affect the readout values, when calibrating the board great attention was payed in switching off the Monitoring Output and disconnecting any test device connected. Figure 5.3 shows

[1] the software can be downloaded at:
https://gitlab.cern.ch/NSWelectronics/vmm_readout_software.

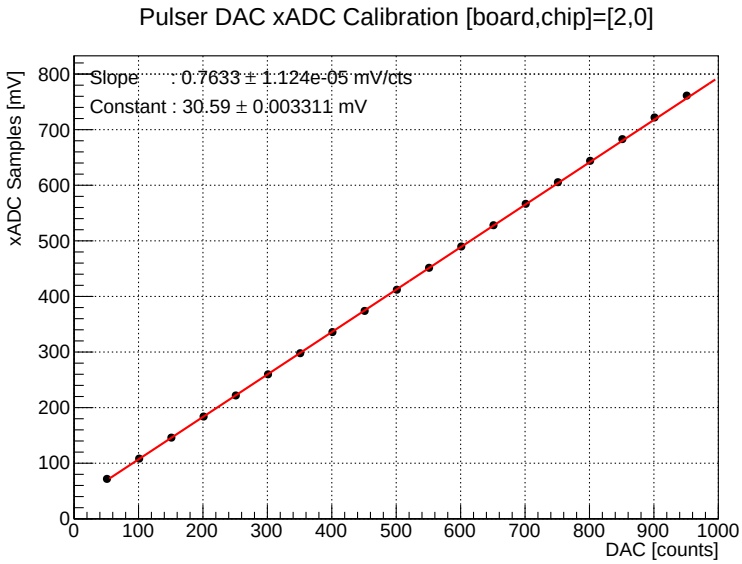

FIGURE 5.4: Calibration curve of the board Test Pulse.

the front-end board; in the central part the VMM ASIC and the FPGA (covered by the fan) are visible, while the external connections can be identified in the upper part of the board: from left Ethernet data cable, ART, MO, external trigger, power. The connection to the detector lays on the back side.

5.3 The DAQ and Calibration software

The official software for interfacing the MMFE1 board, called VMM Ethernet Readout SOftware or VERSO, manages the data collection from the board and is equipped with tools for calibrating the board. The DAQ software can handle both the continuous readout mode and the L0, ATLAS specific, readout. VERSO Graphical User Interface allow the user to monitor all the VMM registers; user defined values of the registers can be written in the ASIC via the "configure" command.
VERSO has some pre-defined loops that allow to change recursively the values in the ASIC registers, like the threshold value and the test pulse height. Some calibration data taking require the sampling of the analog value read out via the MO: this task is accomplished by the FPGA ADC. The calibration tool is completed by a dedicated set of macros[2] in ROOT, the CERN data analysis framework. The calibration macros open the calibration files and perform preliminary analysis depending on the type of calibration. The following paragraphs are dedicated to the different calibration analysis that were run.

[2]The calibration software can be downloaded at:
https://gitlab.cern.ch/NSWelectronics/vmm_calibration_software.

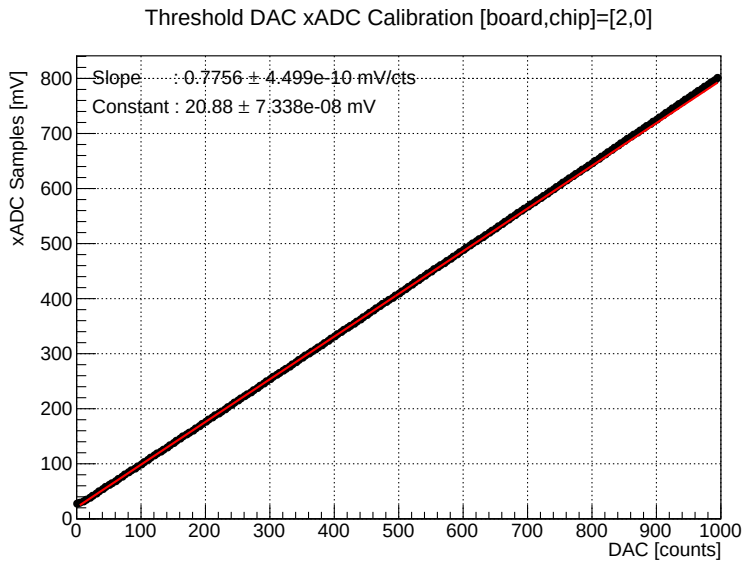

FIGURE 5.5: Calibration curve of the board Threshold

5.3.1 Test pulse and Threshold DAC

The test pulse height has values between 0 V and 1 V and a 10-bit DAC allows the user to select the desired amplitude. A conversion curve between DAC values and pulse amplitude in mV is obtained by sampling the analog voltage with the FPGA xADC; data are shown in picture 5.4. A linear fit to the data, of type:

$$TP[mV] = a + b * TP[DACcts] \tag{5.1}$$

gives the following conversion parameters:
$a = 30.59 \pm 0.003\ mV$
$b = 0.7633 \pm 0.00001\ mV/cts$
quoted in the figure. A similar procedure was adopted to extract the correlation between the threshold DAC and its voltage level in mV; the resulting curve is plotted in figure 5.5. A linear fit of type 5.1 gives the following parameters:
$a = 20.88 \pm 7.338 \cdot 10^{-8}\ mV$
$b = 0.7756 \pm 4.499 \cdot 10^{-10}\ mV/cts$

5.3.2 Baselines and Noise

The baseline values, that differ from channel to channel, are measured by sampling the analog value of the baseline via the MO when no input charge is injected in the Charge Amplifier, *i.e.* neither test pulses nor signals. The number of collected samples N is defined by the user. A histogram is made with the N samples and a Gaussian fit gives the mean values of the distribution and estimates the noise as the standard deviation of the curve. Note that the values of baselines and noise depend on the parameters of the shaper.

The shaping time is kept at 200 ns for all the measurements, while the gain is varied according to the physics needs. Figure 5.6 shows an example of a noise histogram with 2000 samples, measured in one single channel for $G = 0.5\ mV/fC$; the ADC counts on the x axis correspond to the 12 bit counts of the FPGA ADC. The procedure described above is looped over

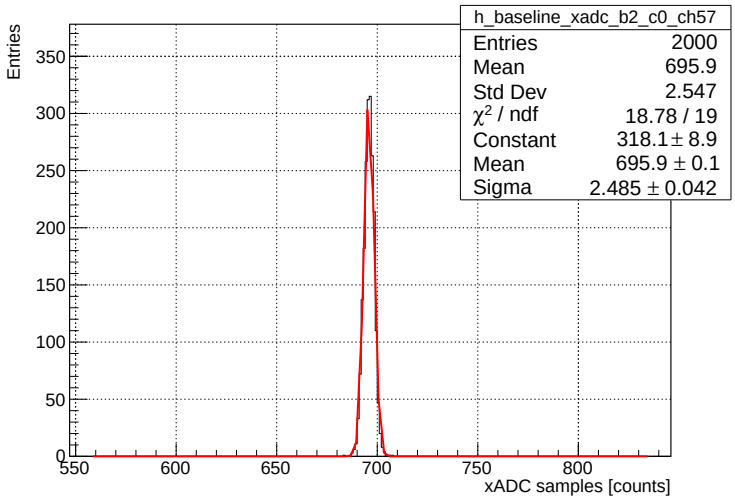

FIGURE 5.6: Baselines samples in 57 (connected to detector pad 58). Shaping parameter are $\tau = 200\ ns$ and $G = 0.5\ mV/fC$.

all the VMM channels and a summary plot is presented in figure 5.7. The left plot shows the baselines measured in the 64 channels; the mean value, quoted on the plot is $167 \pm 2\ mV$. The right plot shows the standard deviation of the Gaussian fits and gives an estimate of the noise levels; the mean value is $0.55 \pm 0.07\ mV$.

For a more convenient comparison with other ASICs, the noise levels are quoted in Equivalent Noise Charge (ENC), *i.e.* the amount of charge, in number of electrons, which, amplified, gives the observed noise level. Figure 5.8 shows the ENC, averaged over the ASIC channels, studied varying

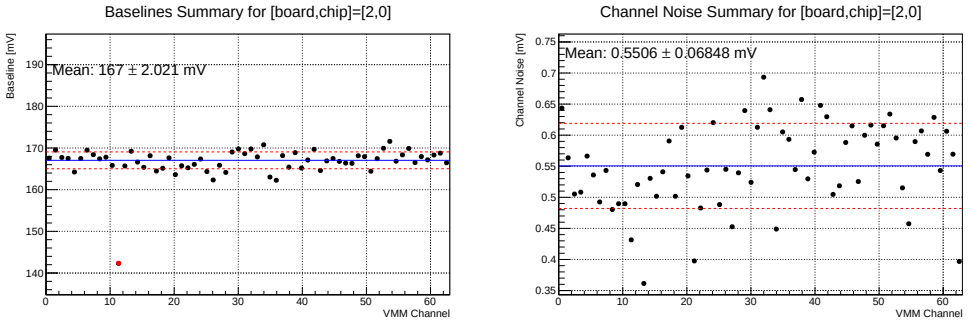

FIGURE 5.7: Left: summary of baselines values. Right: summary of noise measurements.In both figures, the blue line indicates the mean value and the red dashed lines the standard deviation.

the charge amplifier gain in all eight possible values. The presented measurements of ENC include the effect of the noise introduced by the prototype chamber described in chapter 6. For high amplification gains the ENC is below 1000 e^-, not far from the $\sim$ 900 e^- obtained during the operation of COMPASS MPGD-based photon detectors with APV25 [34]. The result is promising, however the ENC strongly depends on the front-end board design and future applications of these detectors with VMM will require dedicated studies.

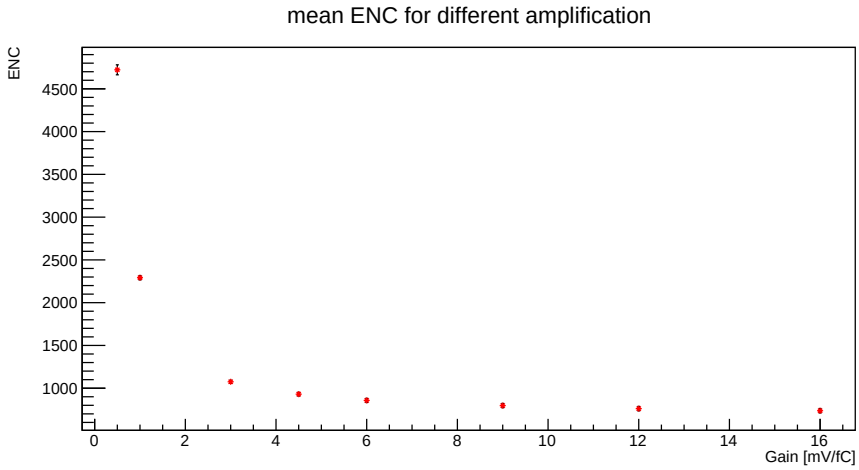

FIGURE 5.8: ENC

5.3.3 Threshold Trim

The fluctuations of the baseline might severely affect the discrimination efficiency, since the threshold has a global value, constant over all the channels. To account for channel-dependent variations, a 5-bit DAC adjusts the threshold at the level of 30 mV, so that the discriminator selects events with the same threshold charge. After calibration, a common channel discrimination above pedestal is set. The single channel DAC values are written in a *xml* format that can be fed to VERSO; the software writes the correct values in the ASIC registers.

5.4 Data extraction software

The data of the the front-end board are transferred to the DAQ computer and stored in root files; each root file contains two trees, one stores the run variables, like gain and shaping time, while the other contains the data. To extract the data from the files I wrote dedicated root macros that also perform some basic analysis; the macros are available in Trieste Laboratory server for future studies. The basic features of the extraction software is to extrapolate the data from the complex structure in which they are arranged to a more convenient format. The main focus of the macros is on the extraction of the pulse height distribution in a histogram.

5.4.1 Channel calibration

Pulse heights are digitized with the VMM 10-bit ADC. In order to get a correspondence between input charge and ADC channel a calibration with known input charges is needed. The calibration software, then, extracts the calibration data from the data tree and produces a histogram, that, ideally, contains one peak per input charge. The peaks are identified with a simple pattern recognition algorithm. In order to correctly associate each peak to the input charge value, the input charges are selected to be all equally spaced in terms of charge except for two values, for which the gap is doubled. The double spacing between two peaks in the histogram will allows to identify all the peaks. Once the coarse peak position is identified, a weighted mean measurement is done in an interval of the identified peak position: the centroid is then the precise measurement of the peak. A graph of peak positions versus input charges is created for each channel and is fitted with a linear slope. The fit parameters are used to convert the ADC values in charge.

5.4.2 Gain extraction

Extraction of the gain from the VMM data depends on the physical source that is used, as will be discussed in sections 7 and 8. In all cases the gain is calculated from the parameters of a fit run on the pulse amplitude histograms. The pulse amplitudes are extracted from the data tree, they are converted in a value in charge, using the calibration curve of the particular channel, and stored in a histogram. A simple pattern recognition algorithm is run to identify the regions of interest where the fit will be performed.

Chapter 6

The construction of the detector prototype

In order to study the coupling of VMM ASIC to COMPASS MPGD-based photon detectors, I built a small test chamber. The chamber is a smaller and simplified version of COMPASS hybrid photon detectors described in 3.2.1: in fact, unlike COMPASS MPGD-based photon detectors, a single THGEM amplification stage precedes the Micromegas. A gain similar to the one obtained by COMPASS photon detectors is ensured by an appropriate tuning of the amplification fields. We do not expect large differences at the front-end entrance since the last amplification stage, that shapes the signal, is the same in both detectors.
The building process of the test chamber had two phases; first a single stage detector with Micromegas - only was finalized and tested, while the production of THGEMs was ongoing. Eventually, the THGEM foil was added to the chamber and the detector was finalized.

6.1 The anode plane

The anode plane covers an active area of 13 $cm \times 13$ cm and is a Printed Circuit Board (PCB) segmented in 256 square pads of size 7.7 $mm \times 7.7$ mm with a pitch 8 mm. The pads are grouped in four radial sectors; the pads belonging to the same sector are read out via the Panasonic P5K connector, of which 64 channels only are used. The position of the connectors, one on each side of the anode plane, allows simultaneous readout with different electronics. The structure of the pads is a copy of the COMPASS hybrid Photon Detectors, with an anode pad facing the mesh, powered via a 470 $M\Omega$ individual resistor (soldered on the back of the PCB plane) and a *pickup pad* buried below 70μ m of fiberglass and connected trough printed vias to the readout connector. Following the powering scheme of COMPASS photon detectors, the mesh is grounded and the pads are biased at a positive voltage. The positive voltage is applied to a pad in the back of the anode plane and distributed by vias to the resistors. The SMD resistors are placed behind each pad they power, as shown in figure 6.1.
The anode plane is completed by a ring that can be independently powered in order to obtain a uniform electric field at the edges of the anode plane.

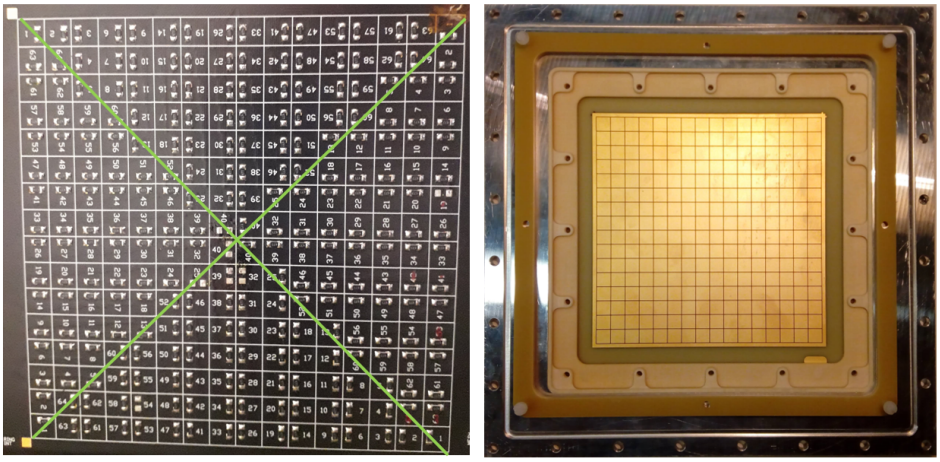

FIGURE 6.1: Back (left figure) and front (right figure) view of the anode plane. On the back the $470 M\Omega$ SMD resistors can be seen on each pad; the green lines indicate the division in sectors. The holes that can be seen bordering the anode in the front view host the screws that suspend the THGEMs (only 8 are used).

The PCB plane that contains all the pads and vias is glued to a 1 *cm* thick aluminum frame that is directly screwed to the the chamber frame and closes the gas vessel. A dielectric border is glued to the aluminum skeleton on top of the anode: eight plastic screws are glued on this element and will support the THGEMs.

6.2 Chamber frame and drift electrode

The gas is contained in a 25 $cm \times 25\ cm \times 6\ cm$ aluminum vessel with 1 *cm* thick lateral walls and 1.5 *cm* thick anode and lid frames, resulting in a total volume of 1.9 *L*. In the lid panel, a window ensures a good transmission of particles; two different windows can be mounted, according to the energy of the particles to be detected. A polyimmide (kapton) window is used to study the response of the detector to ionizing radiation – in our case $\sim$ 6 *keV* X-rays from a ^{55}Fe source. Kapton, however, is not transparent to UV photons and to detect them a fused silica window is used, with good transparency for photons with wavelenght greater than 165 *nm*. The fused silica window, being 5 *mm* thick, would absorb the X rays emitted by the radioactive source. The vessel is equipped with 2 Swagelok QC connectors, one with an inner diameter of 4 mm for the gas inlet and one with an inner diameter of 8 mm for the gas outlet. Eight SHV connectors, arranged in two groups of four, bring high voltage to the THGEM segments. On the lid plane a SHV connector allows to power the drift electrode that is screwed to the window frame. The drift electrode consists in a plane of Au coated Copper - Beryllium wires of 150 μm diameter with a 4 *mm* pitch; support of the wires is provided by a fiberglass frame on which the wires are soldered on printed pads. The

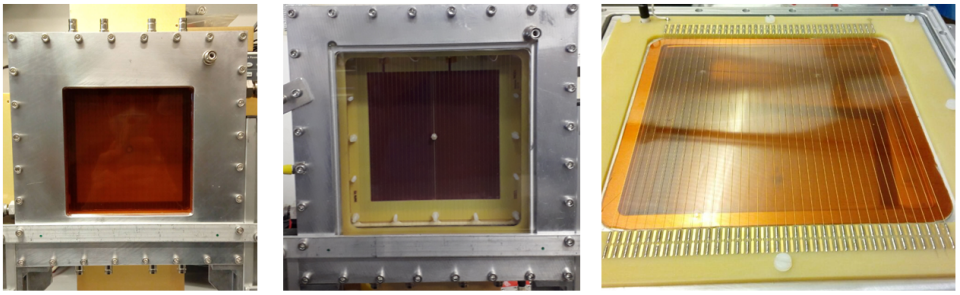

FIGURE 6.2: The two windows of the chamber are shown, the kapton one, in leftmost figure and the fused silica one, in central figure. In right figure the drift plane is shown; drift frame can be mounted on both windows.

distance between the wire plane and the frame is fixed by dielectric spacers and the gap size is chosen in order to avoid discharges between the drift electrode (at $\sim \ -4kV$) and the vessel, grounded. The drift frame can be easily mounted on both windows.

6.3 Micromegas

The Micromegas grid was built at the EP-DT-EF MPT workshop at CERN in standard bulk technology. The pillars were grown on top of two of the anode planes designed in Trieste; on each pad there are four pillars. The amplification gap is 128 μm, while the mesh is made of woven stainless steel wires with 18 μm diameter and 63μm pitch. The mesh is electrically connected to a dedicated pad printed on the anode plane; grounding is ensured by an aluminum braid.
The Micromegas was inspected with a microscope in order to look for possible major defects. With the help of the microscope, the distance between mesh and pad surface was estimated; with a fixed focus, the position of the microscope was recorded when the surface of interest (mesh, pad) was in the focal point. The microscope system has quite a good vertical position resolution ($\pm 1\ \mu m$), but the limit of this method consists in the low precision of the focus position determination. We estimated that the error associated to the human uncertainty is $\sim 10\ \mu m$. The measured distance between the top of the mesh and the anode pad is $117 \pm 10\ \mu m$, roughly compatible with construction parameters; a precise measurement, however, would require dedicated instrumentation. Figure 6.3 shows the Micromegas observed at the microscope; in left figure the focus is on the top of the mesh, while in the right figure the focus is at the pad surface.

6.4 THGEM

The design parameters of the prototype THGEMs reproduce COMPASS photon detectors: fiberglass layers are 400 μm thick, coated with 35 μm Cu on both sides, for a total thickness of 70 μm. The holes have 400 μm diameter and are arranged in a triangular pattern with 800 μm pitch; holes have no rim. THGEM foils have $\sim 17\ cm \times 17\ cm$ surface with a $\sim 13\ cm \times 13\ cm$ active area. In order to improve the electrical stability and reduce the recovery time after discharge, the active area is segmented in two sectors, each one independently powered. The holes that lay at the edges of the active area have a larger diameter, 500 μm, to mitigate border effects of the field. The misalignment between holes layers is obtained by producing two types of THGEM.

6.4.1 Uniformity studies

In order to ensure a good gain uniformity over the entire THGEM, the distance between top and bottom electrodes, *i.e.* the thickness of the fiberglass, must be as constant as possible. A large number of Cu coated fiberglass foils were bought for the upgrade of COMPASS RICH and the ones that showed a good thickness uniformity were selected for producing the THGEMs required by the upgrade [48]. The selection process followed an accurate measurement of the thickness of all the foils performed with a Mitutoyo tester. The setup is shown in figure 6.4; right figure shows the whole setup while left figure shows the ruby tip in detail. Since the THGEMs produced for the presented R&D have a smaller active area compared to COMPASS ones, some of the rejected foils for large detector can be used in a smaller area where they present a good uniformity. Using the data taken by S. Dasgupta [48], I selected three foils with a maximum thickness dispersion over the active area smaller than 3%; the dispersion is calculated using formula 6.1. Foils are labelled, according to the laboratory convention, 310, 311 and 314.

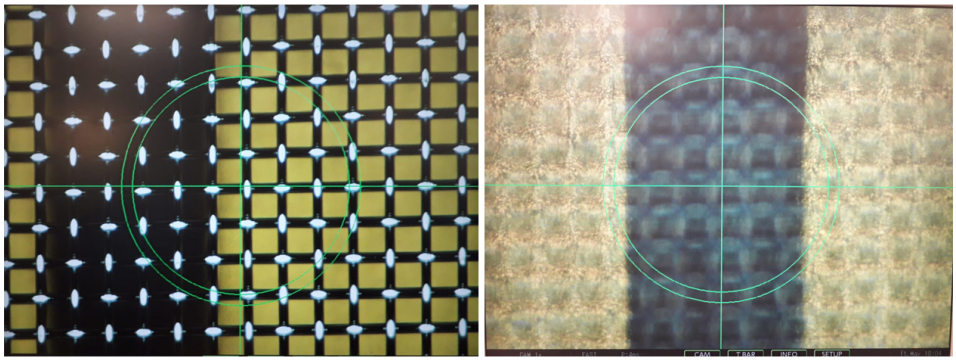

FIGURE 6.3: The two different focus position discussed in 6.3: in the left figure the top of the mesh is focused, in the right one the pad surface is on the focal plane.

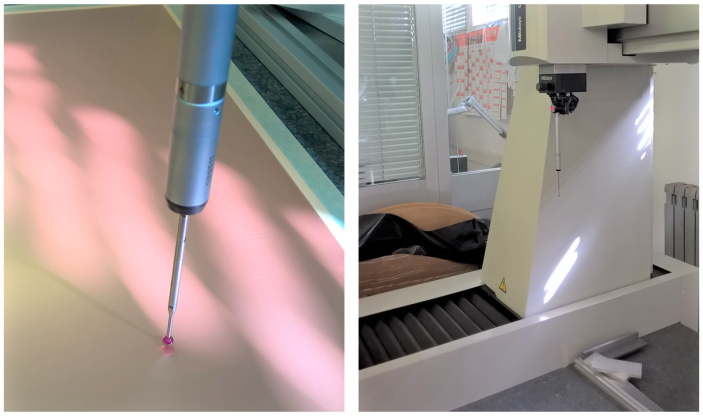

FIGURE 6.4: Left: the ruby tip that touches the surfaces in order to measure its thickness. Right: the whole setup.

$$\frac{d_{max} - d_{min}}{d_{avg}} \leq 3\% \tag{6.1}$$

The three foils were cut in two halves, named A and B or C and D depending on the axis along which the cut was done. Out of each half foil three THGEMs were produced (named α, β and γ) for a total of 18 THGEMs, 9 per type.

6.4.2 Post-processing

The mechanical drilling of the holes might introduce some defects in the final product. Some holes, for instance, might be partially or totally closed due to residual dielectric material: these kind of defects will result in a non-uniformity of the gain. On the other hand, scratches on the Cu surface, with their sharp edges, are places where electric charge will accumulate and will result in sparks. All the THGEMs were eye-checked with a microscope (Din-Lite Digital Microscope[1]) searching for visible defects. None of the THGEMs showed major defects.
All THGEMs underwent the standard post-production process developed for COMPASS RICH-1 upgrade described in S. Dasgupta's thesis [48]. THGEMs are first polished with pumice powder in order to smooth the superficial scratches. The surface is rubbed with pumice powder with the help of an orbital sander. Careful attention was paid in tuning the parameters necessary to obtain a good result: proportions of water and pumice powder, pressure to be applied with the sander, time of rubbing. THGEMs were washed with pressurised water in order to remove any trace of pumice powder; high pressure is necessary for cleaning the holes, that otherwise might be obstructed. With a second eye-check with the microscope I decided whether THGEMs should undergo a second polishing treatment or the process can be finalised. After polishing, THGEMs were cleaned in a ultrasonic bath with a SONICA

[1] web: https://www.dino-lite.com

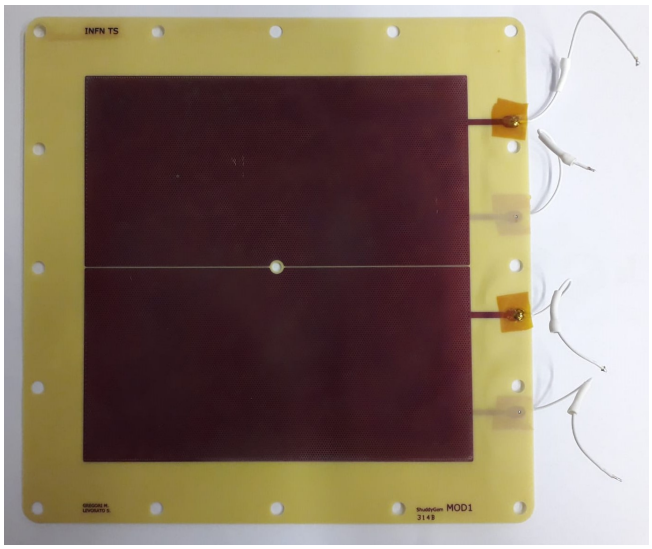

FIGURE 6.5: A THGEM after polishing and cleaning procedure. The four white wires visible on the right of the picture power the four sectors (two on top electrode and two on bottom electrode) independently.

PCB cleaner, a high pH solution (pH $\sim 10.5 - 11.5$). The foils were cleaned for 4h at $60°C$. Residuals of the cleaning solution might be aggressive for the copper layer if they are not washed away, thus the foils were thoroughly rinsed with water and after, with deionized water, in order to prevent the formation of weakly conductive channel between the layers that will eventually draw current during the operation of the detector. Finally, the THGEMs were dried in an oven for 48h at $100°C$. Figure 6.5 shows one THGEM after the polishing and cleaning procedure. The active area is surrounded by a clearance area where large holes are visible; these holes are used to fix the THGEM to the support screws. On the right four cables provide the bias to each of the four sectors (two on the top electrode and two on the bottom). Full THGEM characterization requires a long time, however a breakdown check can be done in order to confirm the quality of the polishing procedure. From the parametrization of Paschen's law on breakdown voltage [49] and the expertise of our lab [48] the maximum bias voltage that THGEMs can stand without discharging is about 2000 V in air. The newly produced THGEMs were tested in a dedicated chamber, shown in figure 6.6, where they can be easily mounted and dismounted and the sectors can be powered independently via crocodile clips. The voltage is increased slowly in each sector until a spark is observed. The THGEM is considered to withstand a particular value of high voltage if for 2 minutes no sparks are registered. If the measured breakdown voltage is lower than the 75% of the expected breakdown voltage, $V_{BD,meas} \leq 75\% V_{BD,th}$, then the THGEM must undergo a second polishing treatment. All the THGEMs produced underwent a second polishing procedure.

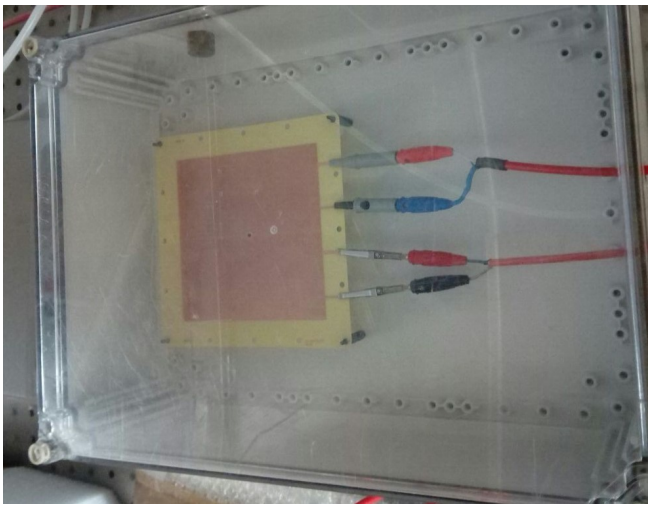

FIGURE 6.6: The chamber used for measuring breakdown voltages (Paschen test).

Chapter 7

Characterization of the prototype with ionizing source

To understand how the VMM-based electronics, coupled to a COMPASS-like photon detector, responds to the signals produced by UV photons, a complete characterization of the chamber must be carried out. The main parameters that are studied in this thesis are gain and stability of the chamber prototype. Since the behaviour of the small chamber described in chapter 6 has to be determined, a first characterization with a known electronics has been done using an ionizing source. Once the response of the chamber is understood, the VMM-based electronics could be characterized.

7.1 Ionizing source

In order to evaluate the gain of the chamber, a ^{55}Fe radioactive source is used. ^{55}Fe is an unstable isotope of iron that decades in ^{55}Mn via electron capture. The vacancy left by the captured electron is filled by an electron coming from an outer shell and the energy difference is released either by emitting an Auger electron or by emitting an X-ray, of energy corresponding to the whole electron energy or part of it. The X-ray production is the relevant phenomenon for our characterization. The K-α-1 and the K-α-2 X-rays are not distinguished with the resolution of our setup, they will be then considered a mono-energetic photon of $E \sim 5.9\ keV$ with a total probability of 28% [35]. The interaction of a 5.9 keV photon with Argon, the main component of the gaseous mixture used in our setup, yields about 220 electrons. A typical spectrum of ^{55}Fe in a Ar based mixture is shown in figure 7.1, taken with the prototype described in this chapter. The spectrum shows a characteristic peak corresponding to 5.9 keV and a second peak at 3 keV due to events where the fluorescence photon has escaped detection; this peak is known as *escape peak*. The effective gain of the chamber is estimated from the charge amplitude of the main peak: since a photon of $E = 5.9\ keV$ produces $\sim$ 220 electrons, the effective gain is computed as the ratio between the amount of charge at the anode and the number of primary electrons, 220.

$$G = \frac{Q_{fin}[C]}{1.6 \times 10^{-19}[C/e]} \cdot \frac{1}{220e} \tag{7.1}$$

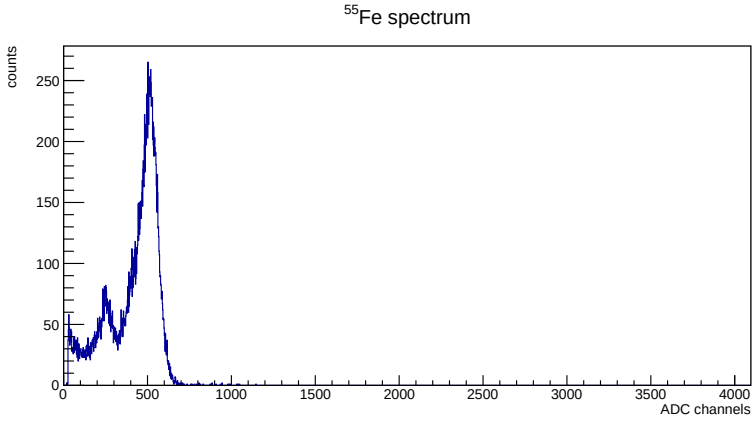

FIGURE 7.1: A spectrum of the ^{55}Fe source measured with the prototype chamber (Micromegas only, $V_{MM} = 550\ V$). Both the main peak and the escape peak are well resolved.

The gain of our chamber in different condition is thus determined using equation 7.1. In this thesis I refer to the effective gain simply as *gain*.

7.2 Electronics

In order to characterize the chamber a single channel readout electronic chain with a known behaviour was mounted. Signals can be collected from any pad or any arbitrary group of pads thanks to an interface board, designed in Trieste, that allows to select the desired pads and ground the others via jumpers. A short LEMO cable (1 *ns*) brings the induced charge to the charge sensitive amplifier (CSA), a Cremat of the family CR-11X . Either CR-110[1], with a nominal amplification of 1.4 mV/fC, or CR-111[2], with a nominal amplification of 0.13 mV/fC, were used depending on the operating conditions of the chamber, and thus on its charge amplification. The CSA is plugged in a CR-150 board[3], specifically designed for hosting devices of this family. On the board, a 1 pF capacitor is connected between a *test in* input and the input of the ASIC: it is used for injecting a known amount of charge at the entrance of the CSA for calibration purpose. The test charge is injected with square voltage signal waves, with a rise time < 13 ns, generated by an Agilent 33220A waveform generator.
The signal from the CSA is amplified and shaped by an Ortec 672, a NIM module housed in a rack dedicated to the test setup. The Ortec 672 features several parameters that can be set by the users in a wide range of values; for the measurements described in this thesis, a Gaussian shaping with 6 μs peaking time is used. Different coarse and fine gains are used according to the type of observed signal; the selection is based on the optimization of signal detection in the Multi-Channel Analyzer (MCA).

[1] https://www.cremat.com/CR-110-R2.1.pdf
[2] https://www.cremat.com/CR-111-R2.1.pdf
[3] https://www.cremat.com/CR-150-R5.pdf

Analog signals are digitized by an AMPTEK Pocket MCA 8000A, interfaced with a computer. The input range is set to 10 V and a 12-bit digitization is used, for a total of 4096 ADC channels; the number of channels is a compromise between the desired precision and the speed of operation. The digital readout is combined with an analog monitor of the signals with an oscilloscope.
The bias voltage necessary to operate the chamber is supplied by two high voltage modules CAEN N1471; the modules are controlled by the lab computer through a dedicated software (GECO). The high voltage modules provide a measurement of the currents in the various electrodes with a high precision ($\pm$ 50 pA). Each module has four independent channels but only six are needed for the prototype tests. The first power supply is used for powering the drift electrode (negative voltage) and the anode pads (biased at positive voltage): it is the only module needed for a Micromegas-alone configuration. The second module, with four negative channels, is used for powering separately the two sectors of the THGEM top and bottom electrodes. Along each line a low pass filter stabilizes the high voltage; the low pass filter implement a simple R-C scheme, with a 500 $M\Omega$ resistor and a 220 pF capacitor, for a cut frequency of $\sim$ 9 Hz.

7.3 Gas

The test setup is completed by the gas mixing and distribution systems. The gas system is composed by two remotely controlled Bronkhorst mass flowmeters with maximum flow rate of 200 L/h, a mixing volume and safety and return bubblers. The laboratory gas mixing system is not ATEX compliant, so methane cannot be used: all the measurements presented in this thesis were taken in an argon-based mixture ($Ar : CO_2 = 70 : 30$), established using the Bronkhorst software interface. Each mass flowmeter is calibrated for one gas only, Ar and CH_4; a conversion table gives the corresponding flow for the actual gas in the second flowmeter, CO_2. The total flow in the chamber is typically fixed at about 10 L/h. Argon gas is stored in 40 L tanks ata pressure of 200 bar pressure and is injected in the laboratory gas system via a pressure reducer, while the carbon dioxide is stored in liquid phase at $\sim$ 70 bar.
At the output of the detector a sensor located in a dedicate chamber along the gas line measures pressure and temperature once per second; pressure and temperature values are used for correcting the measured gain values.

7.4 Characterization of the Micromegas

The test campaign started with the characterization of the Micromegas-alone configuration, *i.e.* without THGEM preamplification. This setup was tested only with the radioactive source, while a test with UV light would be impractical due to the high optical transparency of the micromesh.
The drift electrode is mounted on the kapton window frame positioning the

wires at $\sim$ 3.5 cm above the top of the mesh; in this gap the X-ray photons interact with Ar originating a cloud of primary electrons that drifts towards the mesh. In this region, the field established by the drift electrode must be intense enough to efficiently collect all the charges and avoid recombination; 800 V/cm is considered standard in our setup.

7.4.1 Calibration

Due to the exponential nature of the amplification process, we expect the gain to increase exponentially for increasing the Micromegas bias voltage. At the maximum voltage withstood by the chamber, (610 V) we observe a gain of $\sim$ 20 k, which, for 220 primary electrons, corresponding to a total charge at the input of the front-end electronics of $\sim$ 700 fC. Hence, calibration of the electronic chain was done injecting a known input charge that spans between 25 fC and 800 fC. The relation that links the input charge and the ADC channel is linear and parametrized as follows:

$$ch_{ADC} = a + b * Q_{in} \tag{7.2}$$

with:
$a = (-7.17 \pm 0.34)\ ADC\ ch$
$b = (3.391 \pm 0.001) ADCch/fC$
This calibration is used to determine the input charge from the peak position in the MCA spectrum and, ultimately, estimate the gain.

7.4.2 pT correction

The avalanche multiplication in gases also depends on the mean free path for the electrons which is influenced by the thermodynamic state of the gas [35], mainly its density, which is directly proportional to the pressure and inversely proportional to the absolute temperature. Variations of temperature and pressure, hence, determine a variation of the gain in an avalanche process, and ultimately affect the stability of the chamber gain. It is therefore important to study these variations in a controlled environment in order to be able to compare results taken in different conditions by correcting the gain for environmental conditions variations.
In the chamber, a little overpressure of about 1 $mbar$, necessary to avoid contamination from external gases, is obtained by the means of the return bubbler: 1 cm of paraffin oil ensures an output impedance of about 0.8 $mbar$, that determines the pressure inside the chamber. To change the pressure in a controlled way it would be sufficient to increase the amount of paraffin oil in the bubbler. However, the length of the bubbler allows only small variation of the chamber pressure. For this measurement, then, a dedicated output line replaced the standard one: a 2 m long pipe is connected at the output of the chamber while the other end is dipped in a tank that is progressively filled with water. In this way the response of the chamber to pressure variations is studied over a 30 $mbar$ range, between 970 $mbar$ and 1000 $mbar$. Variations

of temperature affect the stability of the gain as well, however, the laboratory is equipped with an AC system that stabilizes the temperature at 26° C; a temperature scan is not performed, however small fluctuations are recorded by the pT sensors. The study is done at $V_{MM} = 560\ V$ and $E_{drift} = 800\ V/cm$: with these electric configuration we observe stable conditions that allow safe operation without discharges over a long time. Figure 7.2 shows the gain as a function of the variable p/T. The dependence of the gain on p/T is expected

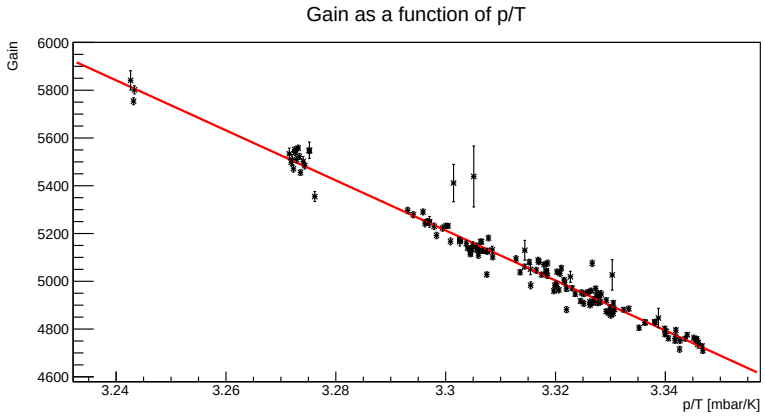

FIGURE 7.2: Gain of the Micromegas-only chamber as a function of pressure over temperature. In the small range studied the dependence can be approximated as linear, hence a linear fit is performed.

to be exponential [35], however, in the small range considered in our setup it can be approximated as linear. A linear fit is performed and the obtained curve is:

$$G = a + b \cdot \frac{p}{T} \tag{7.3}$$

with:
$a = (3.98 \pm 0.02)10^4$
$b = (-1.048 \pm 0.005)10^4 K/mbar$

The fit curve is used for estimating the gain which would be measured with the Micromegas chamber at the standard temperature and pressure for our laboratory, to which all the measurements are referred, $T = 25.7^\circ\ C$ and $p = 980\ mbar$. The estimated is named *corrected gain*.
To study the stability of the gain over time we let the chamber in a continuous data taking configuration for one day. Figure 7.3 shows the values of the measured gain in dark green, along with the corrected gain, in yellow, and with the p/T measurement used to apply the gain correction in light green; no relevant gain variations are observed over time, except from the ones induced by environmental conditions variation that are not perfectly compensated by the correction. Overall, the variation of gain over the time considered is around 3%.

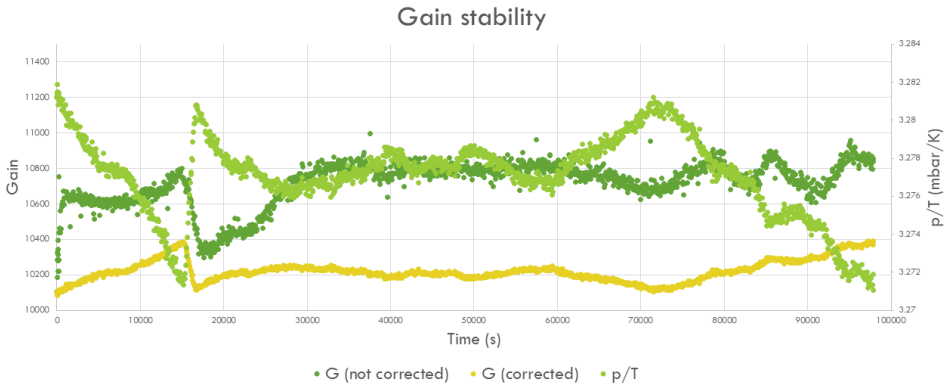

FIGURE 7.3: The measured gain of the chamber as a function of time in dark green and in yellow its values corrected for pressure and temperature variations, presented in light green.

7.4.3 Gain as a function of drift field

A Micromegas chamber is divided in two volumes by the mesh: an amplification gap and a drift gap where the first interaction occurs; in both volumes an electric field must be established to collect the electrons and multiply the charges. An optimization of the electric fields is necessary to have good detector performance; in our setup the mesh is strongly grounded via an aluminum braid connected to the cage, so the only user-defined parameters are the drift voltage (negative) and the pad voltage (positive).
The first measurements are carried out to study the response of the chamber to the variations of the drift field. Figure 7.4 shows the gain of the chamber as a function of the drift field for two different Micromegas voltages. Signals are taken from a single pad on which the ^{55}Fe source is centered. For drift fields greater than $\sim$ 100 V/cm, the electron collection efficiency reaches its maximum value, *i.e.* all the electrons are collected, and the gain has a plateau. In the plateau region no significant variations of the gain are observed.

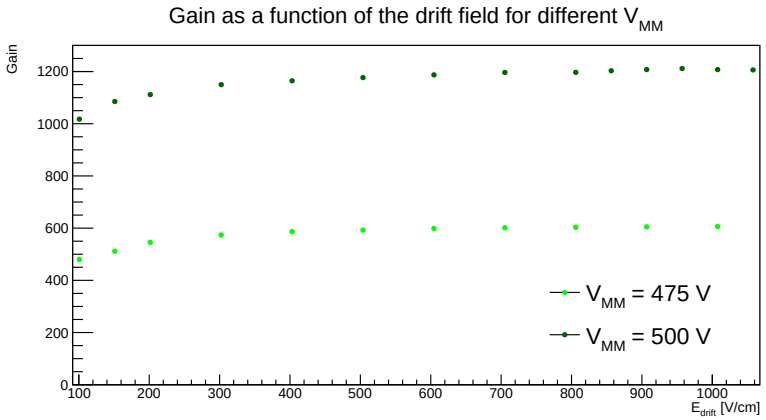

FIGURE 7.4: Gain of the Micromegas-only chamber as a function of the drift field. Two values of Micromegas voltage are studied.

7.4.4 Gain as a function of the Micromegas field

To a first approximation, the electric field in the amplification gap of a Micromegas is uniform and the gain, according to equation 7.4, depends exponentially on the electric field. Figure 7.5 shows the gain as a function of the Micromegas voltage for three fixed drift voltages. The points of the three data sets were fitted with three exponential functions, plotted along with experimental points:

$$G(V) = 10^{\frac{V-V_0}{V_{10}}} \tag{7.4}$$

The parameters V_0 and V_{10} define the gain response of the chamber. In particular, V_{10} defines the bias voltage increase that needs to be applied to the amplification gap to increase the gain by a factor 10.

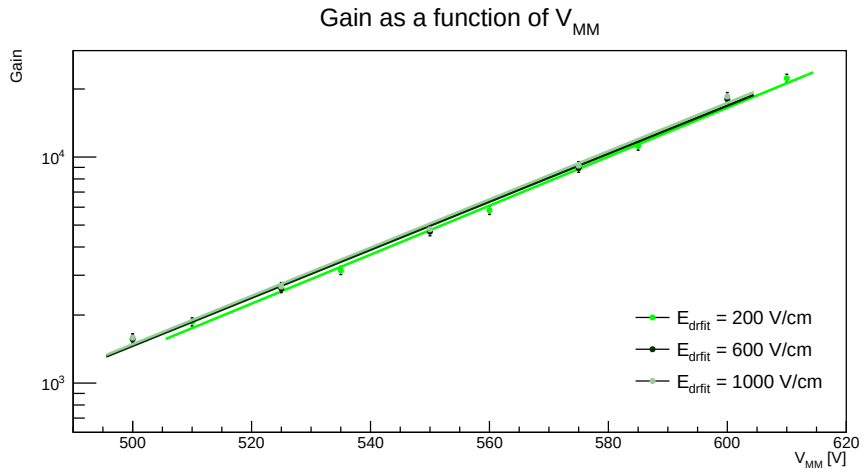

FIGURE 7.5: Gain as a function of Micromegas voltage for different drift fields; the three lines are the fitting curves of the three data sets.

In figure 7.5 three different drift field configurations are presented, with a slightly different range in the amplification voltage. The exponential curves well describe the data. The results of V_{10} extraction are listed in the top part of table 7.1. The values are compatible among themselves and similar to the standard values obtained for standard COMPASS RICH-1 Micromegas.
The collection efficiency of a Micromegas detector is determined by the ratio between the amplification field and the drift field, $R = E_a/E_d$. A second set of measurements was obtained keeping the ratio between amplification and drift field at a constant value. Three different ratios were explored, that correspond to $E_a/E_d = 199.22$, $E_a/E_d = 218.75$ and $E_a/E_d = 238.28$. Figure 7.6 shows the gain as a function of the Micromegas voltage for the three different *constant ratio* configurations. Results of V_{10} extraction at fixed R are quoted in the bottom part of table 7.1. A comparison of the various plots shows that the measurement are consistent and no significant variations are introduced by changing the drift field, provided we are in the plateau region of graph 7.4. At lower values of E_d, *i.e.* the measurements at fixed R and at $E_d = 200\ V/cm$, the obtained values of V_{10} are slightly smaller, but compatible within errors.

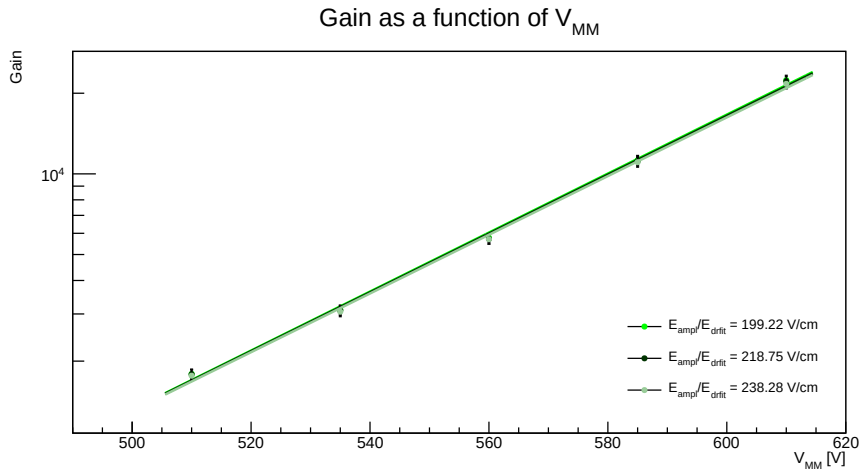

FIGURE 7.6: Gain as a function of the Micromegas voltage for different values of the ratio E_a/E_d.

TABLE 7.1: Values of V_{10} extracted in different drift field configurations.

$E_d[V/cm]$	E_a/E_d	$V_{10}[V]$
200		92 ± 2
600		94 ± 2
1000		94 ± 2
	199.22	91 ± 2
	218.75	91 ± 2
	238.28	91 ± 2

7.5 Characterization of the prototype in the full chamber configuration

After the characterization of the prototype chamber in the Micromegas only configuration, the THGEM amplification stage was mounted. Out of the 18 THGEMs produced, the three that gave best results in the Paschen test were characterized, $310C\alpha$, $314B\alpha$ and $311D\gamma$. THGEMs are supported by plastic pillars and are suspended 5 mm above the mesh. The test chamber can be operated in a COMPASS-like configuration, *i.e.* with two THGEMs and a Micromegas, or in a single THGEM configuration: all the measurements reported in this thesis were performed in the latter configuration. We don't expect significant differences between the two configurations in the charge signal at the input of the front-end electronics. In fact, with the test chamber in $Ar : CO_2 = 70 : 30$ we can reach approximately the same gain that we obtain in COMPASS photon detectors. Moreover, the final amplification stage before the front-end is the same for both detectors.
Figure 7.7 shows a schematic view of the chamber where the dimensions of the various parts are indicated. The gap between the drift electrode and the

top of the THGEM is called *drift gap* and is 2.99 *cm* thick; here the primary interaction occurs and the electrons are drifted towards the THGEM holes. The gap between the THGEM and the Micromegas, 0.5 *cm* thick, is called *transfer gap*: the electric field in this region must be high enough to ensure an efficient transport of the charges to the final multiplication stage.

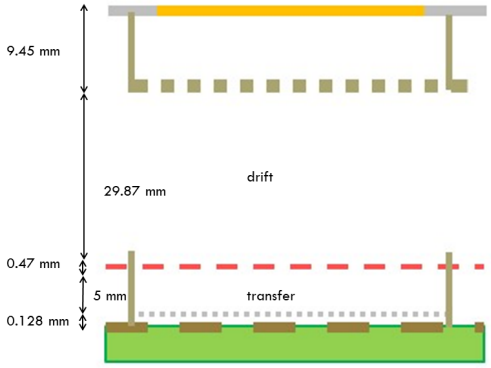

FIGURE 7.7: Schematic view of the chamber. The *drift* field is established between THGEM top and drift wires, while *transfer* field is between the THGEM bottom and the mesh.

7.5.1 Calibration

The Micromegas chamber, equipped with a THGEM, can be tested both with ionizing source and with UV light, exploiting THGEM opacity; in this chapter the ionizing source measurements are presented. The two amplification stages allow high gains, therefore a Cremat CR-111, with a nominal CSA gain of 0.13 mV/fC, is used. The new readout electronics requires a dedicated calibration; since THGEM replacement operation is done in a dedicated clean area, the calibration is repeated for each new THGEM. The calibration procedure consists in the injection of a known amount of charge in the range between 0.5 pC and 10 pC. An equation of type 7.2 is fitted for each calibration, resulting in a table of fitting parameters.

7.5.2 Gain stability

Unlike Micromegas, THGEMs show a relevant gain variation in time and reach a stable condition after a certain amount of time of operation. The time for which stability is reached depends on the flux of particles at the dielectric surface, hence, depends on the illumination rate and on the gain. In moderate gain conditions and with the ionizing source available in Trieste laboratory, stable gains are obtained after $\sim$ 5 days of continuous operation.

Figure 7.8 shows the stabilization of the gain of THGEM 311Dγ with the following high voltage configuration: $\Delta V_{THGEM} = 1000\ V$, $\Delta V_{MM} = 560\ V$,

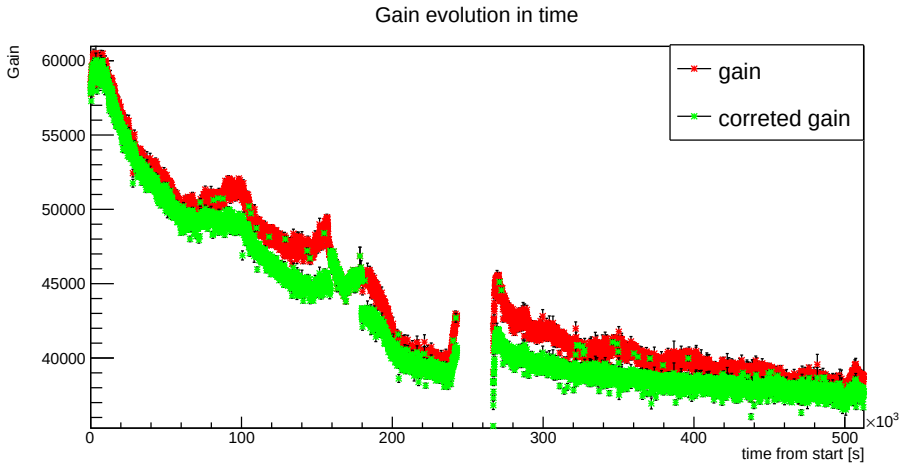

FIGURE 7.8: Gain evolution in time. Red dots represent the measured gain, green dots the gain corrected for pressure and temperature variations.

$E_{drift} = 800\ V/cm$ and $E_{trans} = 1000\ V/cm$. Green dots show the gain corrected for pressure and temperature; the correction applied is measured with a dedicated study carried out after stabilization of the gain is reached and is described in 7.5.3. In figure 7.8 an interruption of the data acquisition is visible, however, the ionizing source was not removed so we can assume that the THGEM kept charging up. This phenomenon, known since many years [50], is understood to be the combination of two different effects that take place when operating a THGEM. On one hand, the powering of the metallic surface close to a dielectric determines the migration of some of the ions inside the fiberglass. The presence of the ions inside the detector bulk reduces the electric field,resulting in a reduction of the gain. On the other hand, a fraction of the electric charge produced in the avalanche accumulates at the dielectric surfaces directly facing the multiplication region, *i.e.* the inner part of the holes and the hole rims, if present. The presence of charges that are not neutralized modifies the electric field in the amplification region, resulting in a further reduction of the gain. The latter effect is compensated by the neutralization of the charges by free electrons until a dynamical equilibrium is reached. Modelling of this process is not straightforward and is not easy to predict the asymptotic value of the gain, however data show a gain reduction of the order of $30\% - 40\%$ from the initial values.
Whenever possible, the measurements of the gain were taken after the stabilization of the prototype chamber gain.

7.5.3 pT correction

Since the dependence of the gain on pressure and temperature is expected to be different from the one measured for the Micromegas detector a new study was performed using the same procedure. The spanned pressure interval is between 972 *mbar* and 996 *mbar*, while the electric configuration is $V_{MM} =$

560 V, $E_{trans} = 1000\ V/cm$, $\Delta V_{THGEM} = 1000\ V$ and $EV_{drift} = 800\ V/cm$. Figure 7.9 shows the gain as a function of the variable p/T. In the small

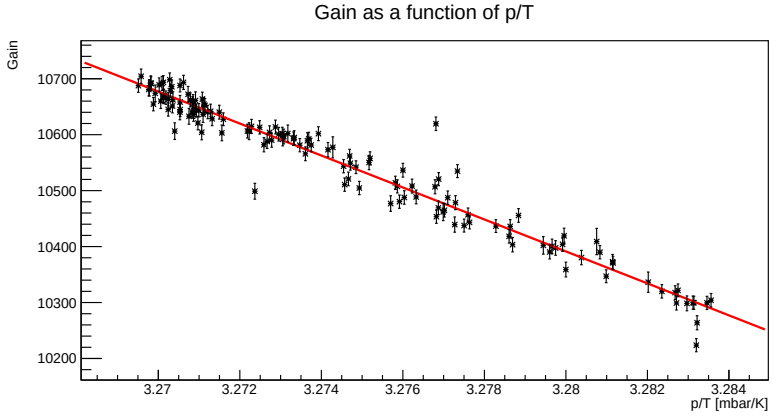

FIGURE 7.9: Gain of the chamber as a function of pressure over temperature. In the small range studied the dependence is approximated as linear, and a linear fit is performed.

range considered in our setup the relation can approximated as linear and linear fit is performed; the obtained curve, of type

$$G = a + b \cdot \frac{p}{T} \tag{7.5}$$

has parameters:
$a = (4.741 \pm 0.013)10^5$
$b = (-1.3198 \pm 0.0042)10^5\ K/mbar$

The fit curve is used for compensating the gains measured with the chamber for temperature and pressure variations. The corrected gain is relative to the standard temperature and pressure for our laboratory.

7.5.4 Gain as a function of drift and transfer fields

The chamber gain, once stabilized, is measured as a function of the drift field; figure 7.10 shows the experimental results for the three THGEMs studied. The electric fields, except for the drift one, are the same as for the gain stabilization procedure, *i.e.* $\Delta V_{THGEM} = 1000\ V$, $\Delta V_{MM} = 560\ V$ and $E_{trans} = 1000\ V/cm$. The graph shows that the drift field set for the gain stabilization, $E_{drift} = 800\ V/cm$, is well in the plateau region; it is then selected as the standard for next measurements.
Transfer field must be tuned as well in order to have full transfer of electrons from the THGEM to the mesh. A dedicated study of the gain as a function of transfer field was done, keeping the other electric fields at the values set for the gain stabilization. Figure 7.11 shows the experimental results; the gain stabilization value of $E_{trans} = 1000\ V/cm$ is just at the beginning of the plateau region and is used as standard for future studies.

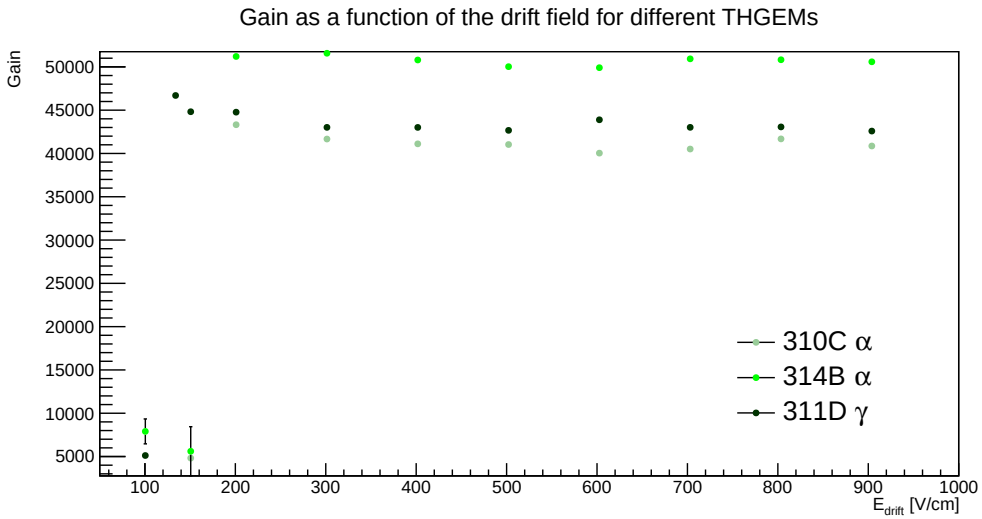

FIGURE 7.10: The gain of the chamber as a function of the drift field for the three measured THGEMs.

7.5.5 Gain as a function of the Micromegas field

With the selected drift and transfer field, the gain was measured as a function of the Micromegas voltage; the voltage range spanned corresponds to the range of the analogous study carried out with the Micromegas-only setup but the THGEM amplification layer gives much higher effective gain. The experimental points were fitted with the same exponential function 7.4. Both experimental points and fit curves are shown in figure 7.12.

Table 7.2 summarizes the V_{10}, the ΔV that needs to be applied to the amplification gap to increase the gain by a factor 10. Values of V_{10} are consistent among themselves but the values are larger than the ones obtained for the Micromegas-only chamber. A possible explanation is suggested the points at $V_{MM} = 610\ V$ which lay below the fitting curves indicating a saturation of the gain at high values ($\geq 10^5$) where space charge effects may become important.

THGEM	$V_{10}[V]$
$310C\alpha$	98.2 ± 0.2
$314B\alpha$	98.1 ± 0.2
$311D\gamma$	97.8 ± 0.2

TABLE 7.2: Values of V_{10} extracted for different THGEMs.

7.5.6 Gain as a function of the THGEM field

Finally, the gain was measured as a function of the bias voltage applied across the THGEM. To a first approximation, the electric field in the central region

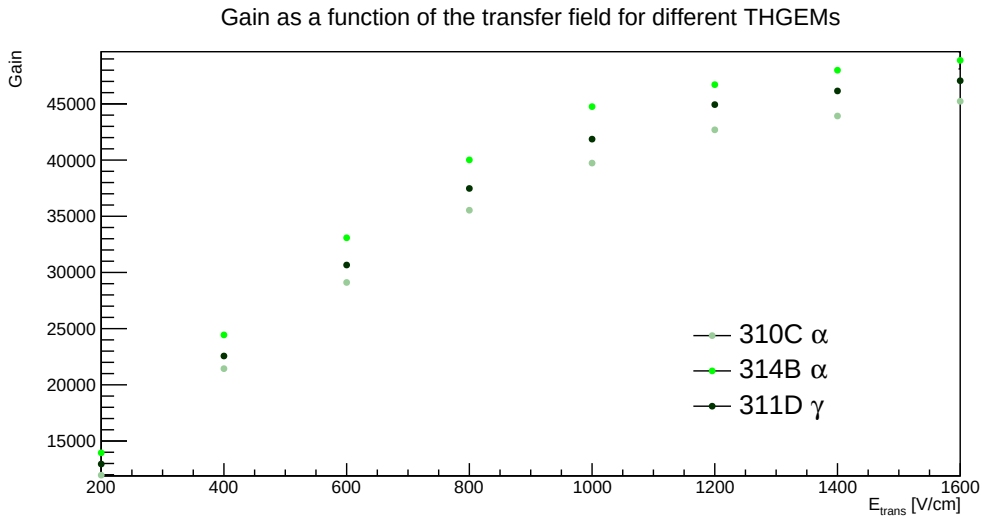

FIGURE 7.11: The gain of the chamber as a function of the transfer field for the three measured THGEMs.

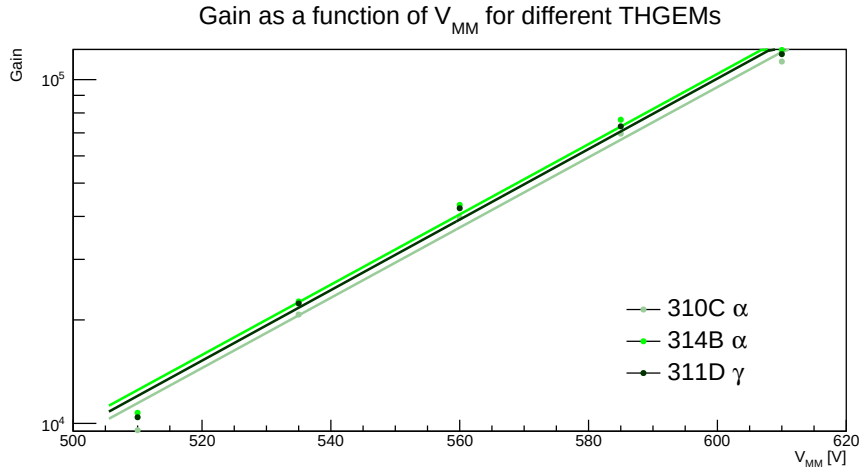

FIGURE 7.12: Gain as a function of the Micromegas voltage for the three measured THGEMs.

inside the holes, where charge multiplication occurs, can be considered constant. The amplification, then, will be an exponential of the applied voltage, just as for the Micromegas; the parameters of the exponential curves, however, are expected to be different. The voltage difference across the THGEMs was varied in a range between 1000 V, which corresponds to the value set for the gain stabilization, to a maximum determined for each THGEM by the presence of discharges. Figure 7.13 shows the gain as a function of THGEM voltages, along with the fit equation 7.4.

The fitting curves do not reproduce the behaviour of the data points, especially at high values of gains ($G \geq 10^5$): in this region the measured points lay slightly below the exponential curve, suggesting a flattening towards a saturation value. This result is reflected on the extracted values of V_{10} summarized in table 7.3: the three values of V_{10}, despite being compatible among

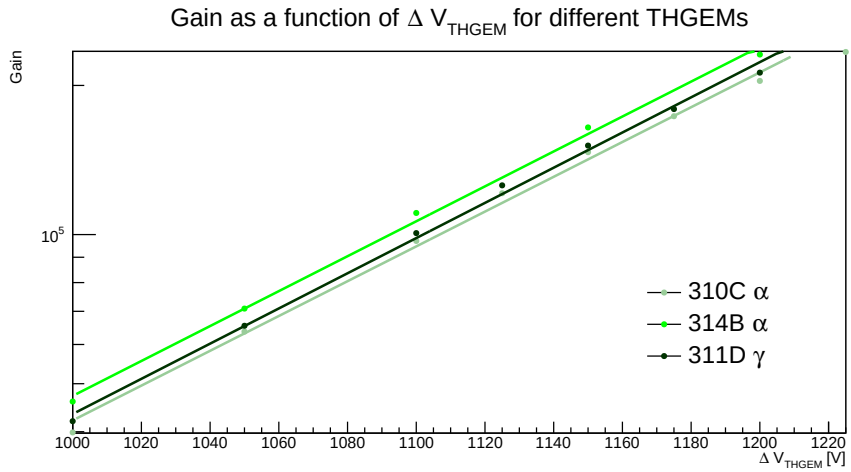

FIGURE 7.13: Gain as a function of the THGEM voltage for the three measured THGEMs.

themselves, are in disagreement with the ones typically obtained in COMPASS THGEM. Moreover, they depend on the fitting range, being higher if points at higher gains are included, indicating a near to saturation effect.

THGEM	$V_{10}[V]$
$310C\alpha$	284.7 ± 0.5
$314B\alpha$	283.7 ± 0.7
$311D\gamma$	281.6 ± 0.7

TABLE 7.3: Values of V_{10} extracted for different THGEMs.

This phenomenon can be interpreted as a saturation of the gain in the proximity of the Raether limit, discussed in chapter 1: at these very high gains, an avalanche triggered by 220 primary electrons would contain $\sim 10^7$ electrons. The prototype can be operated near to the Raether limit can be reached thanks to the good electrical stability of the detector. The saturation of the gains at high values of ΔV_{THGEM} is confirmed by a study of the gain as a function of the THGEM bias at a smaller Micromegas gain ($V_{MM} = 510\ V$), shown in figure 7.14; the comparison is studied only for THGEM $311D\gamma$.

A fit to the data is done for $G \lesssim 10^5$, where the exponential approximation is valid; a discrepancy in V_{10} is observed:

$V_{MM}[V]$	$V_{10}[V]$
510	218.5 ± 0.5
560	267.5 ± 0.9

The value of V_{10} for $V_{MM} = 510\ V$ is consistent with the values typically measured for COMPASS THGEMs, while in the case of $V_{MM} = 560\ V$ effects of saturation confines the exponential behaviour to smaller range at lower

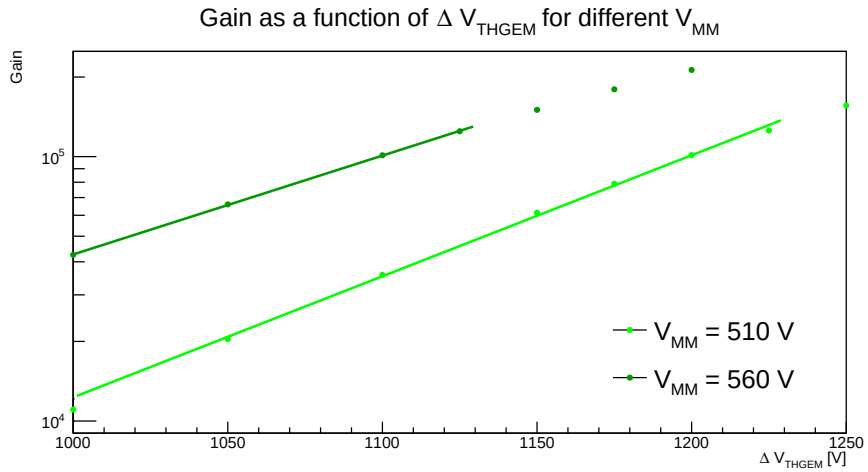

FIGURE 7.14: Gain as a function of ΔV_{THGEM} for two different Micromegas fields.

gain, as can be clearly seen in figure 7.14 and give a larger value for V_{10}.

The chamber is now characterized with a known electronics (CSA + amplifier + MCA) and an ionizing source (^{55}Fe). The characterization allows to select the optimal working conditions for the chamber. On one hand, drift and transfer fields are chosen as the standard values, $E_d = 800\ V/cm$ and $E_{trans} = 1000\ V/cm$, respectively, since they only affect the efficiency in transferring the electrons. On the other hand, the two amplification fields are lowered compared to standard in order to avoid the saturation of the charge input dynamic of the VMM front-end ASIC: signals of the ionizing source, with their 220 primary electrons, saturate the 2 pC input dynamic range for a gain higher than $60k$. The voltages selected as standard are, then $\Delta V_{THGEM} = 1000\ V$ and $V_{MM} = 500\ V$.

7.6 VMM readout

The chamber equipped with THGEM 311$D\gamma$ is tested with the VMM front-end ASIC. The changes done to the setup are minimal, involving only the replacement of the Cremat interface board with the MMFE1 board. Operating voltages are set to their nominal values, *i.e.* $E_{drift} = 800\ V/cm$, $E_{trans} = 1000\ V/cm$, $\Delta V_{THGEM} = 1000\ V$ and $V_{MM} = 500\ V$. The VMM3a allows a simultaneous readout of 64 pads, corresponding to one of the four sectors of the chamber; the studies presented in this chapter are performed in a configuration with the VMM3a connected to the bottom sector.

7.6.1 Calibration

The VMM3a output is a digital word that contains information on the channel number, timing and amplitude of the signal. The signal amplitude, digitized by a 10-bit ADC, is fundamental for estimating the chamber gain and

check the matching with the characterization done with the Cremat-based electronics. A crucial measurement for understanding the behaviour of the new electronics is the conversion between the digital amplitude and the input charge; this calibration needs to be measured on a channel by channel basis.
Each channel has a test capacitance $C_{test} = 300\ fF$ to inject a known amount of charge at the input of the CSA. The charge is injected by a voltage pulse triggered by the FPGA present on the test board. The digitized value is stored in a histogram. The digitized values cluster in a peak per input charge; peaks are identified with a pattern recognition algorithm that measures the centroid of each cluster and rejects spurious peaks. Peaks are associated to the input charge and the relation between the latter and the ADC value is extracted from a linear fit.

Five values of the test pulse DAC are selected for injecting a known amount of charge in each CSA. A dedicated software identifies the peaks in each channels and assigns them to the correct input charge, in order to get a table with the conversion parameters for every channel. A summary of the linear fits to the points in all the channels is presented in figure 7.15; note that four channels are not working. Only a global threshold can be set, for this reason in some channels with a lower baseline the lowest peaks are cut, and the result is a linear fit with a lower number of points. A fit is considered valid if the plot contains at least three points.

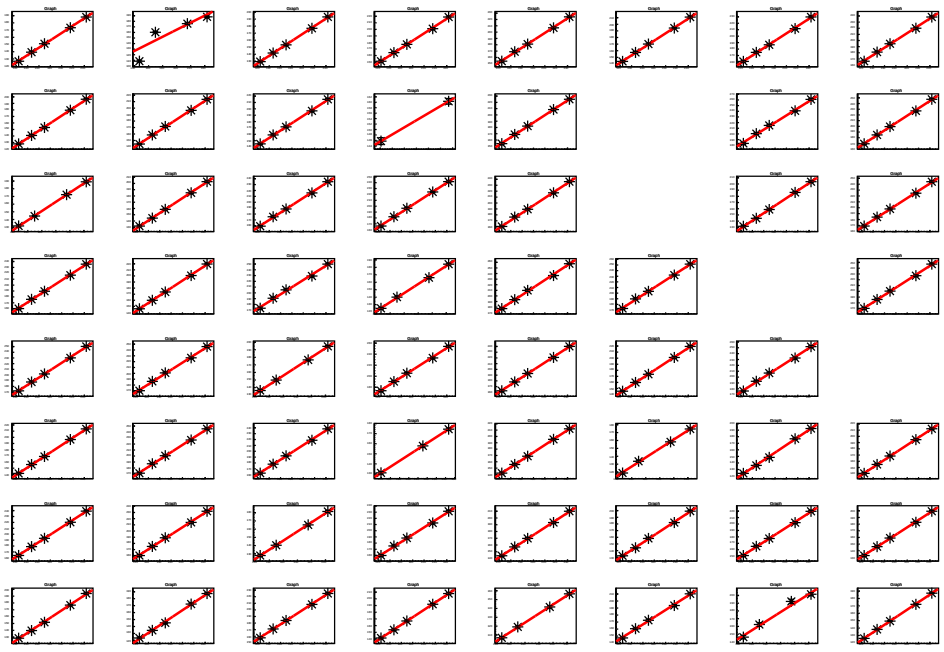

FIGURE 7.15: Calibration curve of the board Test Pulse

7.6.2 Gain as a function of Micromegas and THGEM fields

The gain was studied as a function of the amplification fields, the Micromegas and the THGEM ones. Figures 7.16 and 7.17 show the gain measured in one

single pad, the same in which the plots 7.12 and 7.13 are measured. The plots offer, hence, a comparison of the two electronics. The spanned range in voltage is limited by the maximum input charge accepted by the front-end electronics.

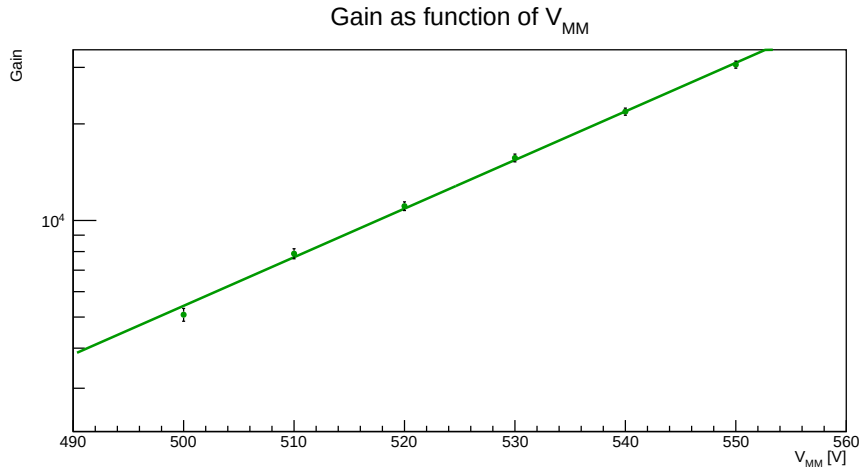

FIGURE 7.16: Gain as a function of the Micromegas voltage.

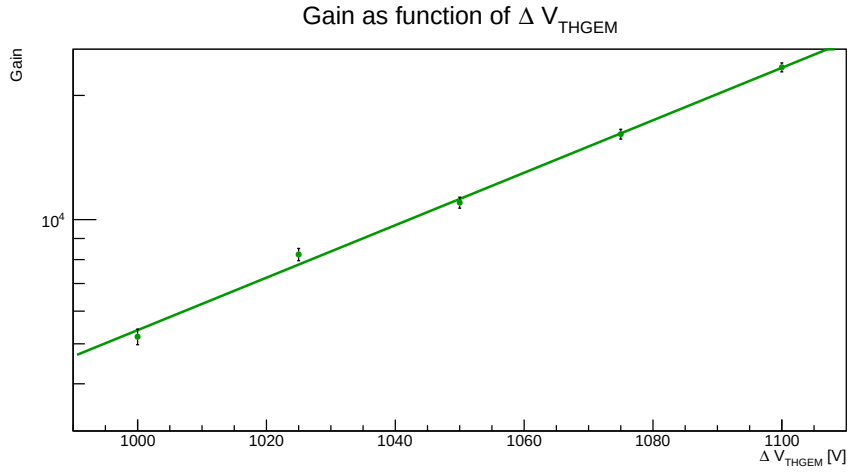

FIGURE 7.17: Gain as a function of the THGEM voltage.

The data points were fitted with a curve of type 7.4; curves are in good agreement with the curves obtained for the chamber characterization with a Cremat-based electronics. The V_{10} parameters are slightly lower than the ones obtained with the previous readout, being $V_{10}^{MM} = (66.0 \pm 1.5)\ V$ and $V_{10}^{THGEM} = (157.3 \pm 4.4)\ V$.

7.7 Comparison of the electronics

A first comparison of the two readout electronics can be obtained from the characterization with the ionizing source. In order to reduce the total amount

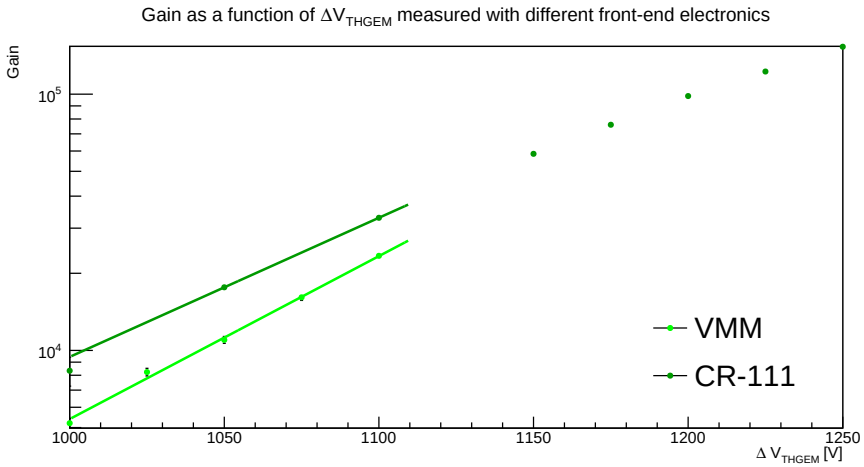

FIGURE 7.18: Gain as a function of the THGEM field.

of charge at the entrance of the VMM, the Micromegas voltage is set to $V_{MM} = 500\ V$; the choice of $V_{MM} = 500\ V$ has an effect on the comparison, since the for measurements with the Cremat-based electronics $V_{MM} = 510\ V$ is used as standard.

The discrepancy between the electronics is relevant in the study of the gain varying the voltage difference across the THGEM, shown in figure 7.18. In this case, not only the value of the gain is different, but also the slopes of the curves slightly differ. The curves were fitted in the same range so the parameters of the Cremat data set fit presented here are different from the ones quoted in 7.5.6. The voltage differences necessary to increase the gain by a factor 10 are, then, $V_{10}^{cre} = 184.2 \pm 1.8V$ and $V_{10}^{VMM} = 157.3 \pm 4.4V$.

A comparison of the electronics that is not biased by the choice of the Micromegas voltage can be observed in figure 7.19, where the transfer, drift and THGEM fields are kept at the nominal voltage and the gain is studied varying the voltage difference across the mesh gap. The systematic shift of the curve here is smaller, since the voltage configurations studied are exactly the same. Also in this case the curves were fitted in the same range, giving $V_{10}^{cre} = 81.4 \pm 0.4\ V$ and $V_{10}^{VMM} = 66.0 \pm 1.5\ V$.

A possible explanation of the different gains is the shorter shaping time τ of the VMM filter. For the presented data taking the shaping time of the Cremat-based electronics was selected at $\tau = 6\ \mu s$, a value that optimizes signal to noise ratio, while the shaping time of the VMM is $\tau = 200\ ns$. A study of the effect of shaping time on the gain is presented in chapter 8.

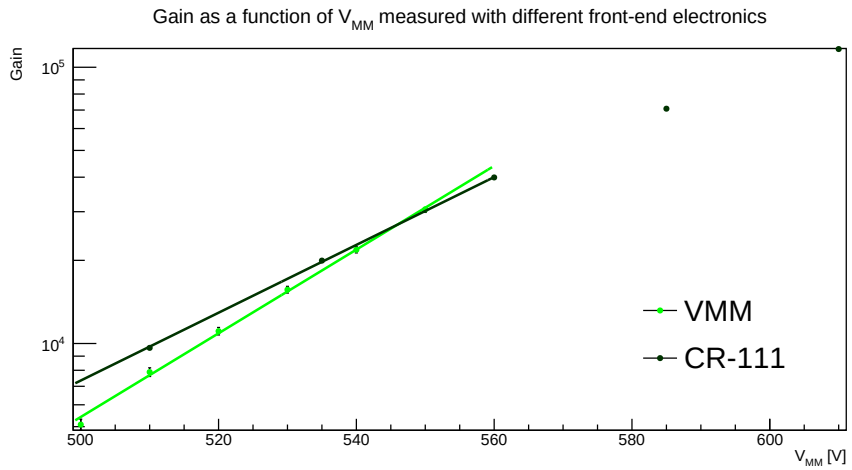

FIGURE 7.19: Gain as a function of the Micromegas field.

Chapter 8

Characterization of the detector prototype with a UV source

The characterization of the prototype with the ionizing source described in the previous chapter (see 7) established the characteristics of the chamber. However, in view of an operation as a photon detector, the study of the gain and the response of the VMM when operated with UV photons, is essential. The working procedure adopted for the tests presented in this chapter follows the same structure outlined for the previous measurements: the characterization of the chamber with the known electronics is followed by the measurements of light spectra taken with the VMM.

8.1 The UV source and extraction of the gain

The spectral range of operation of the Photon Detectors should match the spectral distribution of the Cherenkov photons. In COMPASS MPGD-based photon detectors the operating range, that depends on the properties of the photocathode, is between 160 nm and 200 nm. In the test prototype described in this thesis no photocathode was deposited and we relied on the quantum efficiency of the copper layer on top of the THGEM. The Cherenkov photons were simulated with a UV LED peaking at 250 nm, out of the efficiency range of the COMPASS photocathode but with high enough energy to extract electrons from copper. The low quantum efficiency of copper is compensated by increasing the light intensity. The UV LED is powered by a DC Power Supply and biased at a voltage between 5.5 V and 8.5 V, according to the desired intensity, drawing a current up to 50 mA.
Due to its large optical transparency, the Micromegas-alone was not tested with UV light: all the measurements presented in this chapter are taken with the complete prototype. The THGEM used is the one labelled $311D\gamma$, whose characterization is described in the previous chapter. Another important difference with respect to the previously presented results is the use of the fused silica window, since kapton is not transparent to UV photons. The spacing between the window and the drift wires, however, is unchanged and so are the gaps among the electrodes in the chamber. Figure 8.1 shows a picture of the setup for the measurements of UV photons.
The photon hitting the THGEM surface, either coated with a photocathode or not, will emit a single electron via photoelectric effect; in other words, all

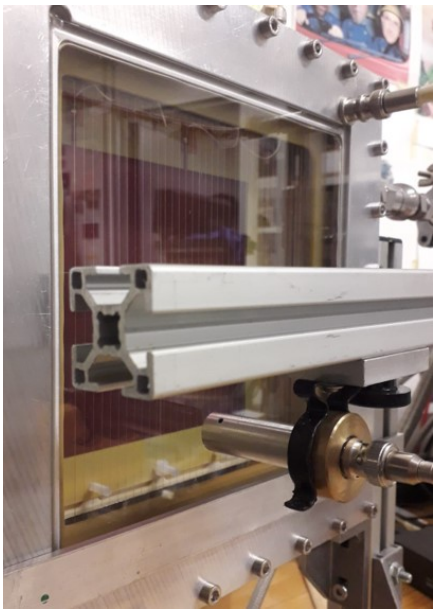

FIGURE 8.1: The chamber with UV LED. Note the fused silica window.

the avalanches that are collected at the anode are generated by a single initial photo-electron. We observe an exponential distribution of the signal amplitude in our conditions and no evidence for deviations from the exponential behaviour. A theoretical description of the mean size of the avalanche in terms of number of electrons can be found in [51].

The effective gain of the chamber is defined as the mean value of the signal charge amplitude distribution. In the case of an exponential curve, it corresponds to the inverse of its slope. The estimation of the mean gain in our setup consists in filling a histogram with measured amplitudes expressed in electric charge. The histogram is then fitted with an exponential curve and the gain and its error are obtained from the fitting parameter. The fitting curve is of type

$$f(x) = \lambda e^{-\lambda x} \tag{8.1}$$

and the mean value of the distribution is $1/\lambda$. The effective gain is thus extracted by expressing the mean value of the distribution in number of electrons and dividing it by the number of initial electrons, namely 1 since the charge multiplication is started by a single photoelectron.

$$G = \frac{1}{\lambda} \tag{8.2}$$

8.2 Chamber characterization with Cremat-based electronics

Before testing the chamber with the new VMM-based readout electronics, the behaviour of the detector prototype illuminated with UV light is determined.

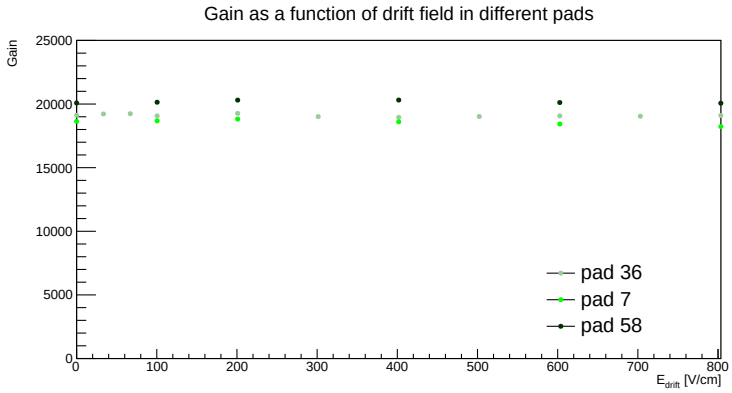

FIGURE 8.2: The gain of the chamber as a function of the drift field for three pads.

A full characterization, then, is carried out with a known electronics setup, namely the one used for characterizing the prototype with the radioactive source. Each user-defined combination of pads can be read out, thanks to the interface board described in chapter 7.2; in the following sections, however, only the pad above which the UV source is placed is read out. The studies were carried out on three different pads, centering the UV source on different parts of the chamber.

8.2.1 Calibration

The avalanche generated by a UV photon hitting the detector, being initiated by a single electron, produces a quite small charge signal, of few fC considering the gain that can be obtained with our chamber. For this reason the Cremat CR-110, with nominal amplification of 1.4 mV/fC is used (see 7.2). The new configuration, obtained mounting the fused silica window and changing the front-end electronics imposes a new calibration. The calibration procedure follows the one described in section 7.4 with an input charge spanning a range between 3 fC and 30 fC.

8.2.2 Gain as a function of drift and transfer fields

In order to select the best working conditions, the gain of the detector is studied varying the drift and the transfer field also for the UV source configuration. The modest avalanche size implies a reduced exposure of the THGEM dielectric to free charges, increasing the time needed for a gain stabilization. The presented measurements were obtained without waiting for the stabilization of the gain; for this reason, the values of the gain are around 40% higher than the corresponding quantities presented in chapter 7.
Figure 8.2 shows the gain as a function of the drift field. As for the ionizing source, the drift field is increased from $E_{drift} = 0\ V/cm$ up to $E_{drift} = 800\ V/cm$, while the other electrodes are kept at a fixed potential, $\Delta V_{THGEM} = 1000\ V$, $V_{MM} = 500\ V$ and $E_{trans} = 1000\ V/cm$. The gain does not change

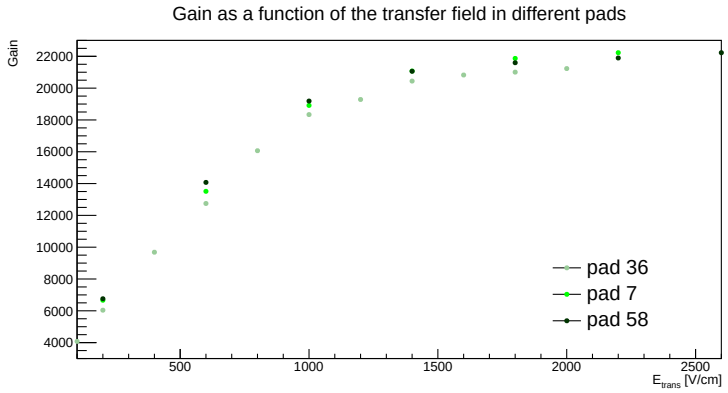

FIGURE 8.3: The gain of the chamber as a function of the transfer field for three pads.

with the variations of the drift fields; this fact can be explained by considering that the avalanche is triggered by a single primary electron, emitted at the THGEM surface and very close to the multiplication volume. The drift field value selected for future operation is the standard $E_{drift} = 800\ V/cm$. On the other hand, variations of the transfer field have a larger impact on the gain, determining a full or a partial transmission of charge. Figure 8.3 illustrates this behaviour showing an increase in the gain until a plateau is reached, for full charge collection. The gain is studied varying the transfer field between $E_{trans} = 100\ V/cm$ and $E_{trans} = 2000\ V/cm$, while the other electrodes are kept at a fixed relative potential, such as $E_{drift} = 800\ V/cm$, $\Delta V_{THGEM} = 1000\ V$ and $V_{MM} = 500\ V$. The operating transfer field is fixed at $E_{trans} = 1000\ V/cm$, at the beginning of the plateau.

8.2.3 Gain as a function of the Micromegas field

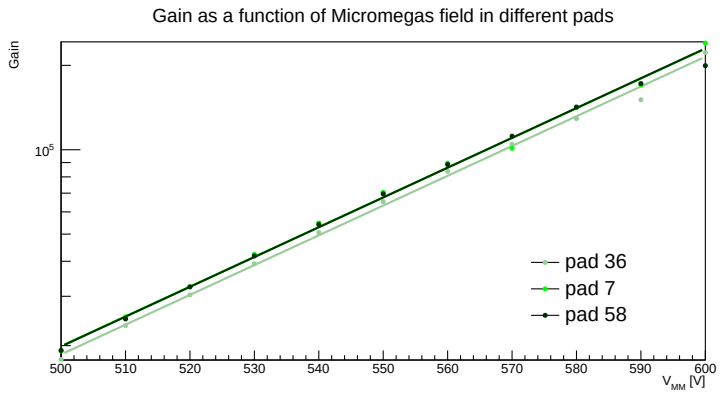

FIGURE 8.4: Gain as a function of the Micromegas voltage for three different pads.

The gain is studied as a function of the voltage difference between mesh and anode, while the other electrodes are kept at a potential such as $E_{trans} = 1000\ V/cm$, $E_{drift} = 800\ V/cm$ and $\Delta V_{THGEM} = 1000\ V$. The gain shows

an exponential behaviour at varying the Micromegas voltage like in the case of the ionizing source; an exponential fit to the data is shown in figure 8.4. From the three fitting curves we extract the parameter V_{10}. The three values, presented in table 8.1, are compatible within error bars and in line with the values obtained with the ionizing source.

TABLE 8.1: Values of V_{10} extracted in different pads.

pad	$V_{10}[V]$
36	94.1 ± 0.2
7	94.3 ± 0.2
58	94.1 ± 0.2

8.2.4 Gain as a function of THGEM field

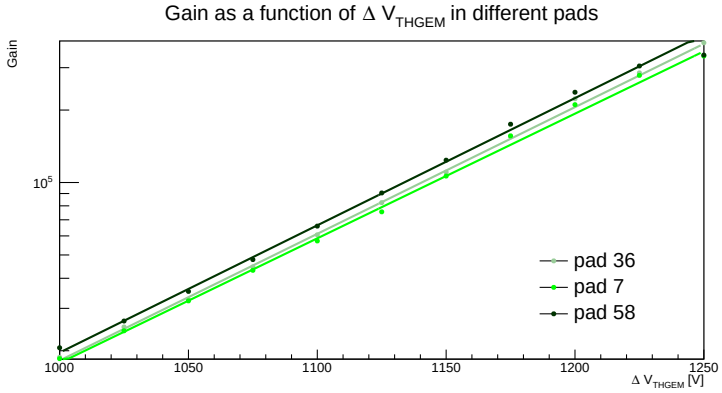

FIGURE 8.5: Gain as a function of the electric field across the THGEM measured in different pads.

The characterization of the chamber is completed by the study of the gain as a function of the voltage difference across the THGEM. For this study the voltage differences among the other electrodes are kept constant so that $E_{trans} = 1000\ V/cm$, $E_{drift} = 800\ V/cm$ and $V_{MM} = 500\ V$; ΔV_{THGEM} is spanned between 1000 V and 1250 V, the maximum voltage difference that the THGEM can withstand without sparks. The gain grows exponentially for increasing ΔV_{THGEM}, as can be seen in figure 8.5. Three data series are collected, one per studied pad; the three series are fitted with an exponential curve which allows to extract the parameter V_{10}. Table 8.2 summarizes the V_{10} values for the three pads. The three values are compatible within few sigmas, however, they are smaller than the V_{10} values obtained with the ^{55}Fe, confirming the trend, shown in figure 7.14, of decreasing V_{10} for decreasing total charge in the avalanche.

To conclude, the chamber has proven to be able to detect single UV photons. The voltage settings have been tuned and the chosen values are $E_{drift} =$

TABLE 8.2: Values of V_{10} extracted in different pads.

pad	$V_{10}[V]$
36	190.0 ± 0.4
7	193.1 ± 0.4
58	189.2 ± 0.5

800 V/cm, $E_{trans} = 1000\ V/cm$ $\Delta V_{THGEM} = 1000\ V$ and $V_{MM} = 500\ V$, confirming the choice made with the first characterization. A difference in the response of the pads, of the order of $\sim 20\%$ is observed and can be regarded as an intrinsic difference among the pads. The same difference is observed with the VMM-based electronics (see section 8.3).

8.3 VMM-based electronics

The single photon signals generated with the UV source are read out with the VMM based electronics described in the previous chapter. In order to detect these small signals the maximum available CSA gain is chosen, *i.e.* 16 mV/fC; the shaping time is kept constant at 200 ns. The new setting configuration requires a new channel by channel calibration. The calibration follows the procedure outlined in the previous chapter. Due to the large gain of the CSA only the low values of the test pulse DAC can be fed to the test capacitor, that correspond to an input charge in the range between 15 fC and 45 fC. A proper calibration could be run only in 16 channels and the results presented in the following refer to them.
Once the calibration curve per each channel is determined, the chamber is tested with photon signals; the digitized values are stored in charge histograms, one per channel. The gain is extracted from a fit to these histograms, as discussed in section 8.1. Figure 8.6 shows as an example the UV spectrum in one of the VMM channel (11), with $E_{drift} = 800\ V/cm$, $E_{trans} = 1000\ V/cm$ $\Delta V_{THGEM} = 1000\ V$ and $V_{MM} = 500\ V$.

8.3.1 Gain as a function of the drift and transfer fields

Figure 8.7 shows the gain as a function of the drift field, while figure 8.8 the gain as a function of the transfer field; both plots show the gain measured in all the sixteen calibrated pads; two pads are highlighted, namely 7 in red and pad 58 in blue: for those pads a comparison with a Cremat-based readout electronics is presented in section 8.4. For performing the presented measurements, the multiplication electrodes were kept at fixed values, $\Delta V_{THGEM} = 1000\ V$ and $V_{MM} = 500\ V$, while $E_{trans} = 1000\ V/cm$ is selected for the drift field variations and $E_{drift} = 800\ V/cm$ for the transfer field variations.

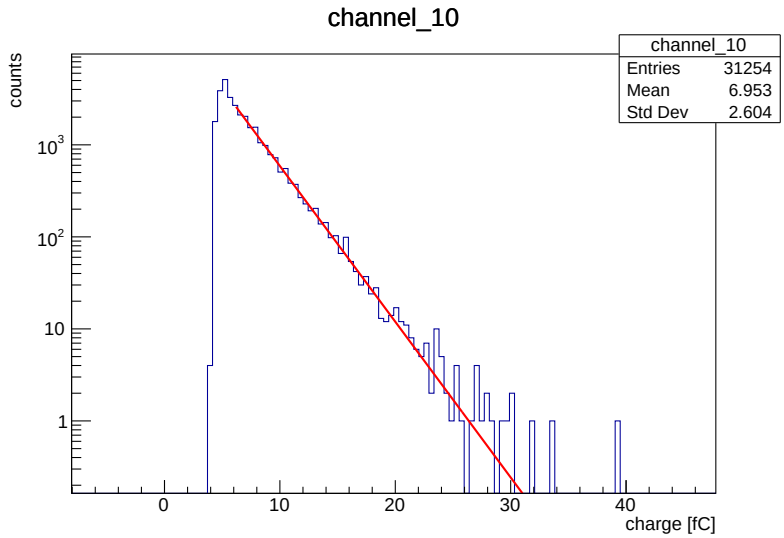

FIGURE 8.6: Spectrum of the UV source obtained in channel 11 with $E_{drift} = 800\ V/cm$, $E_{trans} = 1000\ V/cm$ $\Delta V_{THGEM} = 1000\ V$ and $V_{MM} = 500\ V$.

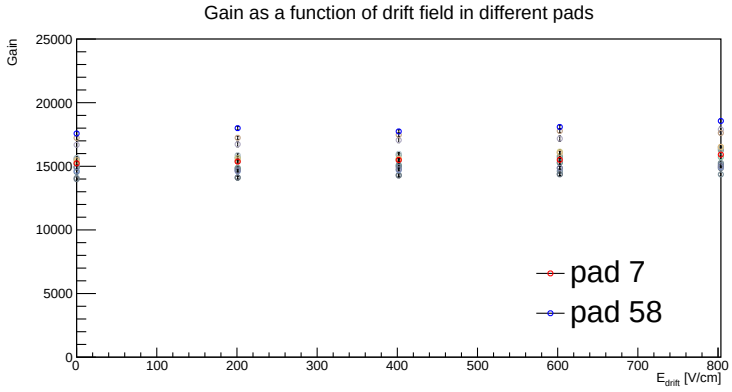

FIGURE 8.7: The gain of the chamber as a function of the drift field.

8.3.2 Gain as a function of the Micromegas field

Figure 8.9 shows the gain as a function of the field between the mesh and the anode in the sixteen pads for which the calibration was done. During this study the other fields were left unchanged at the values of $\Delta V_{THGEM} = 1000\ V$, $E_{drift} = 800\ V/cm$, $E_{trans} = 1000\ V/cm$. The different curves are fits to the data sets, showing that the behaviour is exponential in the Micromegas field. Pad 7 and 58 are highlighted being the former in red and the latter in blue. Non uniformity among the different pads are of the order of 8%; the exponential slopes are consistent to a good level: the gain increases by a factor ten for a mean voltage increase of $V_{10} = 116.9 \pm 1.6\ V$, where the mean value is obtained averaging the sixteen fit parameters. The slope values are compatible within 1.3%.

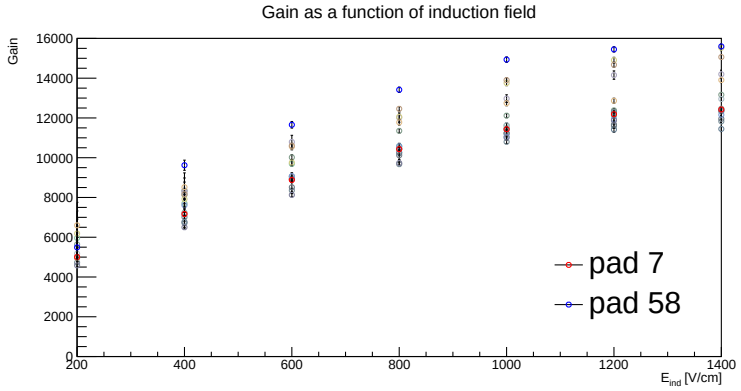

FIGURE 8.8: The gain of the chamber as a function of the transfer field.

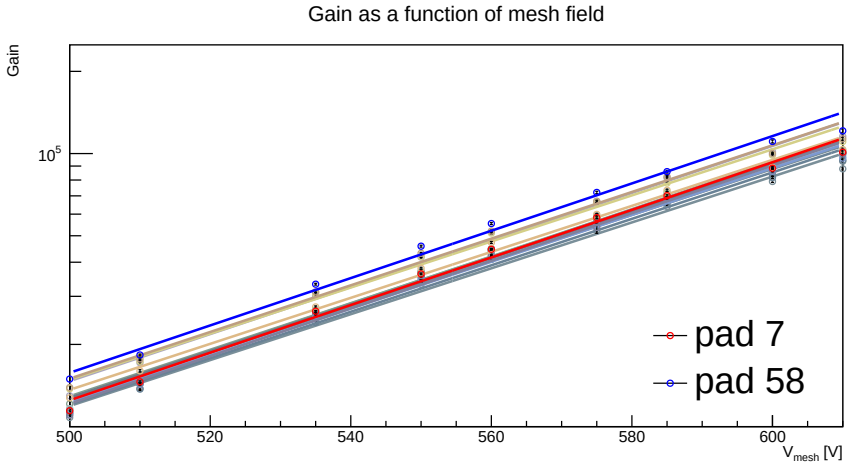

FIGURE 8.9: Gain as a function of the Micromegas field in sixteen pads.

8.3.3 Gain as a function of the THGEM field

Figure 8.10 shows the gain as a function of the field across the THGEM in the sixteen pads for which the calibration was done. During this study the other fields were left unchanged at the values of $V_{MM} = 500\ V$, $E_{drift} = 800\ V/cm$, $E_{trans} = 1000\ V/cm$. The different curves are fits to the data sets, showing that the behaviour is exponential in the THGEM field. Pad 7 and 58 are highlighted being the former in red and the latter in blue. Non uniformity among the different pads are of the order of 10%, however the exponential slopes are consistent to a good level. The gain increases by a factor ten in for a mean voltage increase of $V_{10} = 266 \pm 9\ V$, where the mean value is obtained averaging the sixteen fit parameters. The slope values are compatible within 3%.

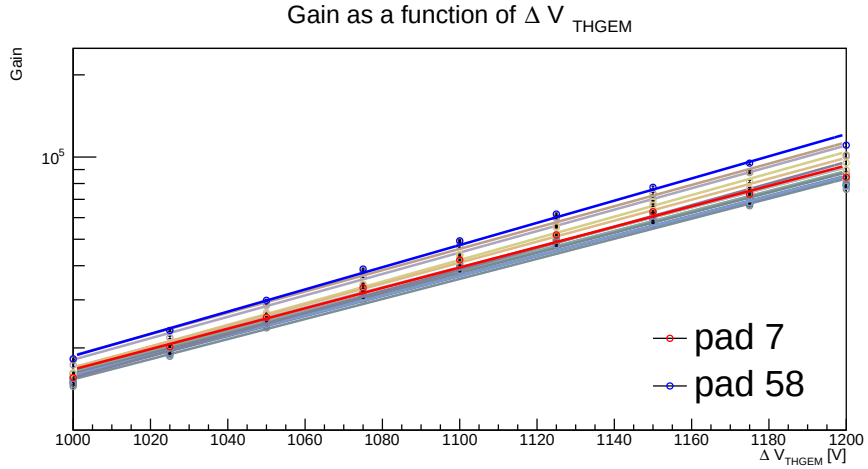

FIGURE 8.10: Gain as a function of ΔV_{THGEM} field in sixteen pads.

8.4 Comparison of the two readout electronics

An extensive characterization of the response of the two electronics to different signals has been carried out; the goal of this section is to compare and discuss the results obtained. A comparison between the two readout electronics is presented only for two electronic channels, corresponding to two readout pads of the chamber (7 and 58). Plots of section 8.3 show that, among the *working pads*, the ones selected for the comparison of the electronics have almost the largest gain intrinsic difference.
The study of the gain as a function of the drift and the transfer field brings little information about the behaviour of the two ASICs. The gain is a constant for varying drift field, meaning that it reached a plateau region with a good collection efficiency. The transfer field seems to play a more relevant role in determining the gain. This can be easily explained considering that a low enough transfer field does not collect entirely the charge but lets some electrons hit the bottom of the THGEM. With both readout electronics a rise followed by a plateau is observed. The field necessary to stabilize the gain is the same, $E_{trans} = 800\ V/cm$, with both electronics setup, as expected.
More interesting is the case of the comparison for the amplification fields, across the mesh gap and across the THGEM.

Figure 8.11 and 8.12 show the gain as a function of the mesh voltage in pad 7 and 58 respectively. In both pads a discrepancy in the gain values measured with the two front-ends can be observed; the amplitude measured with the CR-110 is about 20% larger at lower values of V_{MM}, increasing for higher values of V_{MM}. The same behaviour can be observed also for the study of the gain as a function of the voltage difference across the THGEM, presented in figure 8.13 and 8.14; the former refers to pad 7 while the latter to pad 58.

A hint to explain the discrepancy comes from the consideration that the electronics have largely different shaping times, 6 μs for the Cremat - Ortec

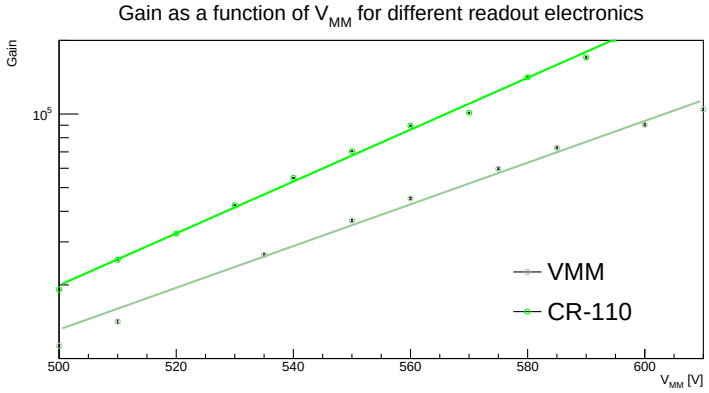

FIGURE 8.11: Gain as a function of the Micromegas voltage for pad 7 with the two tested electronic readouts.

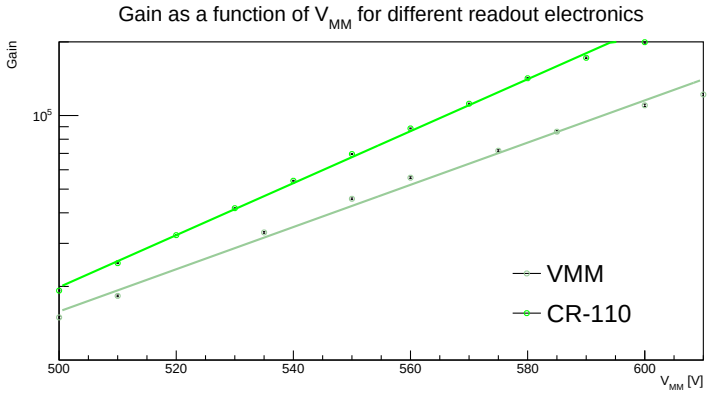

FIGURE 8.12: Gain as a function of the Micromegas voltage for pad 58 with the two tested electronic readouts.

system and 200 *ns* for the VMM. A short shaping time might mean that the output of the CSA has not reached its maximum when the filter cuts it down to restore the baseline; this phenomenon is known as *ballistic deficit*.. This behaviour is confirmed by a complementary study that was carried out with the same chamber: in one pad and for fixed values of the electric fields, the gain is measured as a function of the shaping time, spanning the range allowed by the Ortec shaper (from 0.5 μs to 10 μs). The study, presented in figure 8.15, shows that a reduction in shaping time of a factor 20, from 10 μs to 0.5 μs, determines a reduction in gain of 15%. The effect is observed also in the response to a faster signal provided with the waveform generator; in this case, however, the discrepancy is of the order of 1%, hinting at the ballistic deficit as the cause of the gain reduction. The maximum VMM shaping time, 200 *ns*, is smaller than the minimum Ortec shaping time by a factor 2.5, supporting the presented explanation of the discrepancy. A difference in the values of V_{10} in the study of the gain as a function of Micromegas and THGEM field is also observed. A possible explanation comes from the consideration that space charge affects the signal formation time, increasing its time spread. The effect of ballistic deficit may become important even at smaller values of total charge.

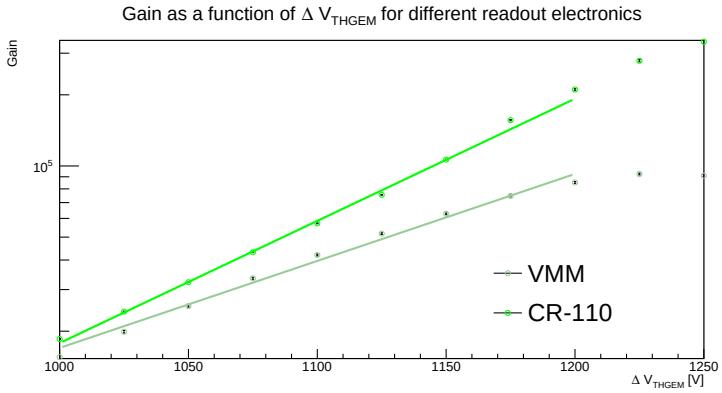

FIGURE 8.13: Gain as a function of the THGEM voltage for pad 7 with the two tested electronic readouts.

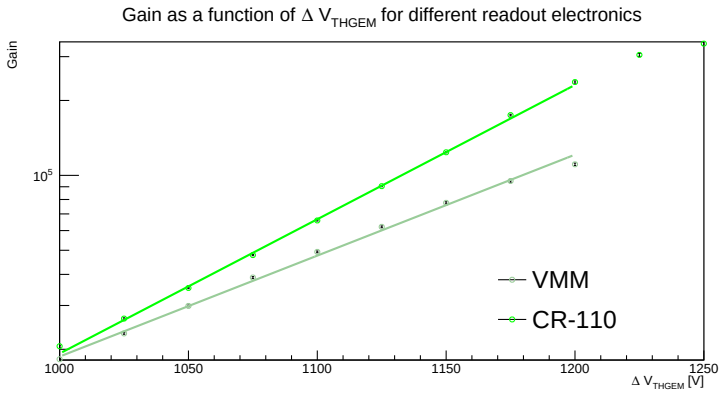

FIGURE 8.14: Gain as a function of the THGEM voltage for pad 58 with the two tested electronic readouts.

The new front-end is capable of detecting the feeble signals generated by single photo-electrons and the response in the channels studied is comparable with the response of the Cremat-based electronics. The discrepancies of the electronics find a reasonable explanation in the different shaping time that cuts part of the signals. We can conclude from the comparison of the "known" electronics with the new, VMM-based one, that the latter seems well suited for the single photon detection application and no major obstacle to its use are found in the present study.

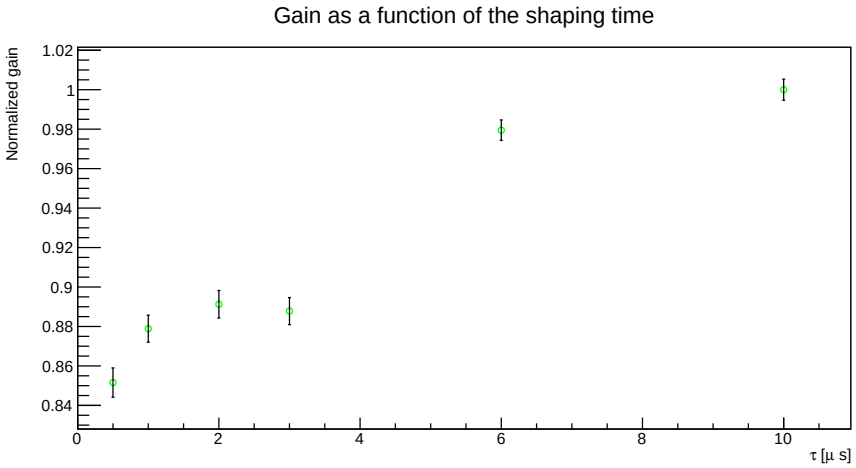

FIGURE 8.15: Gain as a function of the Ortec shaping time. For simplicity the gains are normalized to the maximum gain, namely the one obtained for the maximum possible shaping time, 10 μs.

Chapter 9

Nanodiamond powder as a novel photocathode

Gaseous detection of photons in the far UV range, $\lambda < 200\ nm$, where the Cherenkov emission has its maximum, requires a dedicated photoconverter, that absorbs the photons and emits electrons. The first photoconverters used in gaseous photon detectors were photo-ionizing vapours added to the main gas mixture [33]. Solid photoconverters were later introduced to overcome the limitations imposed by gaseous photoconverters, namely the lower rate capabilities, the need for large volumes with related parallax error and their explosive and corrosive nature that made their handling complicated. Currently, solid photoconverters based on caesium iodide (CsI) are used in almost all applications. CsI has a high quantum efficiency in the wavelength range below 200 nm and is more robust than other photoconverting materials used in vacuum-based photon detectors. A measurement of its quantum efficiency as a function of the photon wavelength is reported in figure 9.1, taken from [52]. Despite their widespread use, however, CsI based photon detectors have some limitations. A quantum efficiency degradation appears in case of water vapour absorption: the hygroscopic nature of the CsI makes the photocathode handling a very delicate operation. Moreover, quantum efficiency degradation is observed after intense ion bombardment, for an integrated charge of $\sim 1\ mC/cm^2$, making it unsuitable for high radiation environments. In a gaseous detector the main source of ions is the charge multiplication process: in each collision ions are produced along with electrons and drift towards the cathode; their neutralization on the detector electrodes depends on the geometry. Attempts to reduce the ion backflow were done by changing the geometry, like in the case of the COMPASS RICH-1 MPGD-based photon detectors described in chapter 3, that achieved a ion backflow below 3% [34].
The MPGD-based photon detectors, coupled with a CsI photoconverter, may not satisfy the stringent requirements of high gains at high rates of the ePIC environment at the EIC. The quest for an alternative UV-sensitive photocathode overcoming these limitations is a crucial step to export the MPGD photon detection technology to a new generation of RICH detectors.

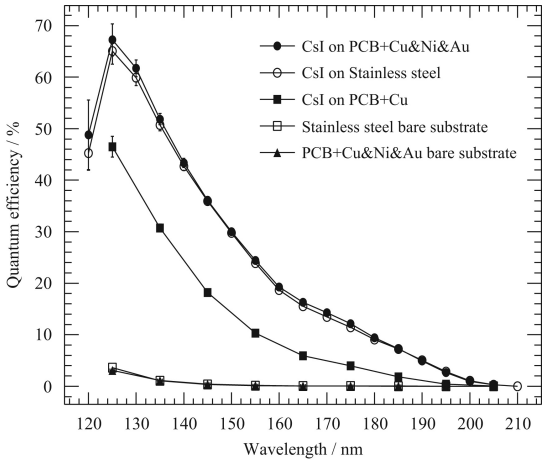

FIGURE 9.1: Quantum efficiency of CsI on different substrates, from [52]; the full points refer to the same type of substrate used for the studies of HND presented in this thesis.

9.1 Nanodiamond powder as photoconverter

The vast success of CsI as a photoconverter in the UV range is due to its high quantum efficiency, related to the low electron affinity (0.1 eV) and the wide band gap (6.2 eV) [53]. Nanodiamond particles have comparable band gap (5.5 eV) and low electron affinity ($0.35 - 0.50$ eV); if they are hydrogenated, their electron affinity decreases to -1.27 eV. The negative electron affinity allows an efficient escape in the vacuum of the generated photo electrons without an energy barrier at the surface [54]. Moreover, nanodiamond show chemical inertness and good radiation hardness, being a good candidate for replacing the more fragile CsI.
A comparison of the quantum efficiencies of the two material can be found in literature. Hydrogenated nanodiamond (H-ND), at $\lambda = 146$ nm have a quantum efficiency of 22% [54], while the quantum efficiency for CsI at the same wavelength is $\sim$ 40% [55]. The considerations on quantum efficiency and robustness of H-ND based photocathodes are the main motivation for the R&D presented, which developed following two main threads: on one side, the measurement of the quantum efficiency in a gas mixture and on the other side, the coupling of the novel photocathode with the THGEM technology.

9.1.1 Hydrogenation and spraying technique

The standard procedure of hydrogenation of ND powder photocathodes is performed by using the MicroWave Plasma Enhanced Chemical Vapor Deposition (MWPECVD) technique. For the treatment in microwave H_2 plasma, the ND powder is placed in a tungsten boat positioned on a heatable substrate holder of an ASTeX type reactor evacuated to a base pressure better than 7×10^{-7} $mbar$. The powder is heated at 650° C using an external radiative heater (via a Proportional Integral Derivative feedback control system),

then H_2 gas is flowed in the chamber at 200 *sccm*, the pressure and the microwave power are maintained at 50 *mbar* and 1250 *W*, respectively. The heating due to the microwave power increases further the temperature of the powders up to 1138° *C* as determined by a dual wavelength ($\lambda_1 = 2.1\ \mu m$ and $\lambda_1 = 2.4\ \mu m$) infrared pyrometer. After one hour of H_2 plasma exposure, the hydrogenated powder are cooled to room temperature under high vacuum; the cooling procedure takes about one day.
The MWPECVD technique, requiring temperatures higher than 1000° *C* can not be used to hydrogenate ND coated THGEMs since the dielectric material (fiberglass) would not sustain temperatures above 180° *C*. A novel technique to overcome this limitation was developed in Bari and it consists in a two steps procedure. First the ND powder is hydrogenated as described above. Then, a solution is prepared with the hydrogenated powder and deionized water in one to one proportion; the solution is sonicated for one hour and sprayed on the desired substrate (either THGEMs or simple plates, called *coins*, used for QE measurements) using a pressure atomizer in pulses of 100 *ms*, called *shots*, at about 3 *Hz* frequency. The pressure atomizer has configurable parameters and is operated via a LabView based controller. The substrates are kept at $\sim$ 150° *C* and rotated by a magnetic stirrer; the distance between the atomizer nozzle and the substrate is around 10 *mm*. The spraying procedure is used also for coating the substrates with non hydrogenated NDs for comparative studies.
The effective coating of the surface depends, to a first approximation, on the number of shots. A preliminary study was done to determine the optimal number of shots by measuring the quantum efficiency of substrates coated with a different amount of material, *i.e.* a different number of shots. The result, reported in figure 9.2 indicates that for a number of shots $\gtrsim$ 100 the quantum efficiency has no appreciable variations.

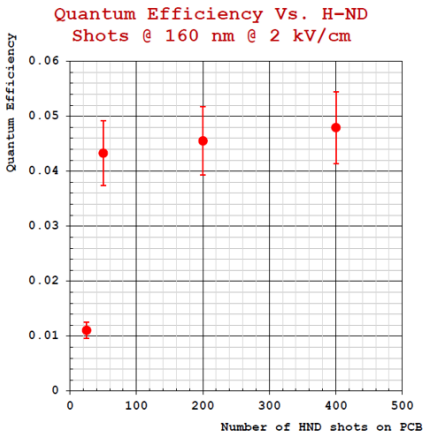

FIGURE 9.2: Quantum efficiency as a function of the number of shots. For more than 100 shots no variation of the QE are observed.

9.1.2 Quantum efficiency measurements

In the context of the present R&D, three types of nanodiamond powder, produced by different companies, are studied. Two of them have average grain size of 250 nm and are produced by Diamonds & Tools (D&T) srl and Element 6 (E6); the third type, boron doped (BDD) produced by SOMEBETTER: ChangSha 3 Better Ultra-hard materials Co., LTD has an average grain size of 500 nm. The quantum efficiency of each of the three was studied in both *as received* (ND) and hydrogenated (H-ND) form, for different wavelengths and different applied electric fields. The hydrogenated D&T ND powder has the highest quantum efficiency for all the wavelengths in vacuum. Figure 9.3 shows the quantum efficiency measured as a function of the photon wavelength. The left plot shows the quantum efficiency of the three nanodiamond powders, both *as received* and hydrogenated, while the right plot only the QE of the best performing one, the powder produced by D&T.

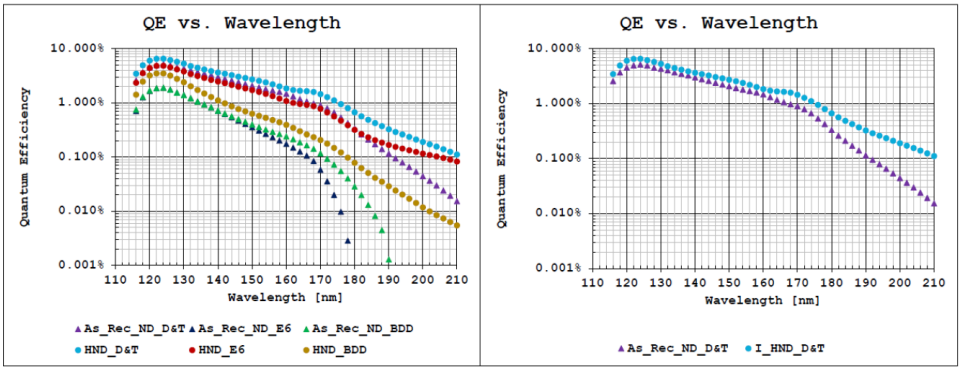

FIGURE 9.3: Quantum efficiency as a function of the photon wavelength. Left: the six tested powders, right: the best performing one (D&T) *as received* and hydrogenated.

9.1.3 QE measurement in different gas mixtures

The measurements of quantum efficiency reported in [55] and [54], as well as the ones described in section 9.1.2, were taken in vacuum chambers, where no gas was present at the surface of the photocathode and the photoelectron was emitted in vacuum. The situation of a solid state photoconverter in a gaseous detector, however, is quite different, since the photocathode faces a gas volume where several phenomena can modify the quantum efficiency. The standard gas mixture of COMPASS MPGD-based photon detectors in $Ar : CH_4 = 50 : 50$; the presented measurement is done, hence, in variable proportions of these two gases, from pure Ar to pure CH_4.
The measurements presented here are taken in Bari laboratories. The UV photons are generated by a deuterium lamp (whose spectrum has a peak at about 160 nm) and their wavelength is selected by a monochromator. The produced photons impinge either on the sample or on a NIST calibrated photodiode that gives a reference for quantum efficiency studies. The currents

are read out via a picoammeter. The sample is contained in a chamber where a gas mixture can be flushed; between the sample and the chamber window, where incoming photons arrive, a grating of thin wires ensures the possibility to establish an electric field at the photoconverting material surface.

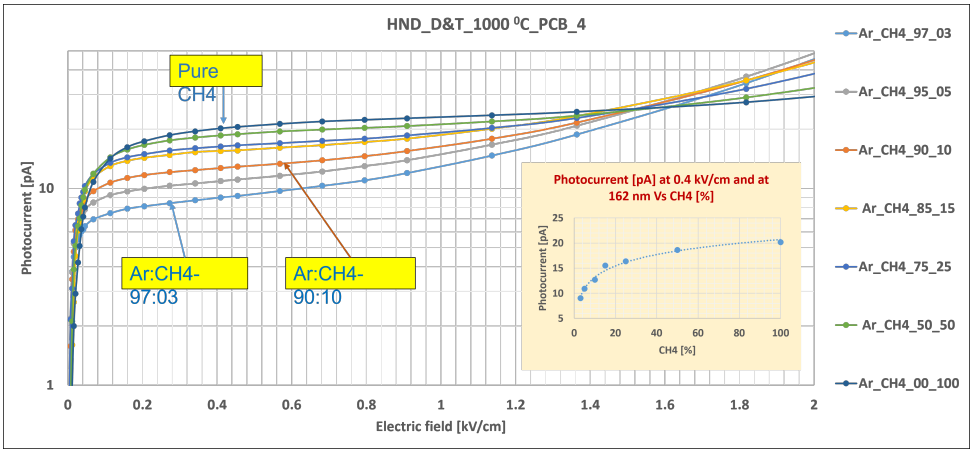

FIGURE 9.4: Photocurrents at $\lambda = 160\ nm$ as a function of the electric field. Different gas mixtures are tested.

The H-ND D&T powder is tested in different mixtures of Ar and CH_4. Figure 9.4 shows the measured photocurrents at lamp peak wavelength (160 nm) for varying electric fields; the different curves correspond to different proportion of the gases. At low electric field, Ar rich mixtures give a lower photocurrent compared to CH_4 rich ones: this is explained by the large cross section for Ar electron backscattering. For an electric field of $\sim$ 0.5 kV/cm one can observe a small effect of charge multiplication that becomes dominant at $\sim$ 1 kV/cm for Ar rich mixtures.

9.1.4 Quantum efficiency degradation study

To study the robustness of H-ND based photocathodes, a quantum efficiency measurement in different irradiation conditions is performed. Measurements were taken in the ASSET setup at GDD laboratory at CERN. The setup is made of two main chambers, one used for quantum efficiency measurement and the other for ion bombardment; the passage of the sample between the two is done with an automated manipulator under vacuum, that prevents exposure to air. Ions are generated by avalanche multiplication in gas: an X-ray source illuminates the gas volume, while a suitable electric field is established between the sample and a metallic grid fixed at 5 mm above the sample. Quantum efficiency is studied in a wavelength range between 130 nm and 180 nm in steps of 5 nm, while the accumulated charge goes up to $\sim 8\ mC/cm^2$. In the same setup a freshly CsI coated sample is tested under the same irradiation conditions. Results of the measurements are reported in figure 9.5. The quantum efficiency of H-ND is halved for an integrated charge of $\sim$ 5 mC, while the quantum efficiency of CsI is halved for an integrated

charge of $\sim 0.5\ mC$, suggesting that H-ND is ten times more robust than CsI against irradiation and ion bombardment.

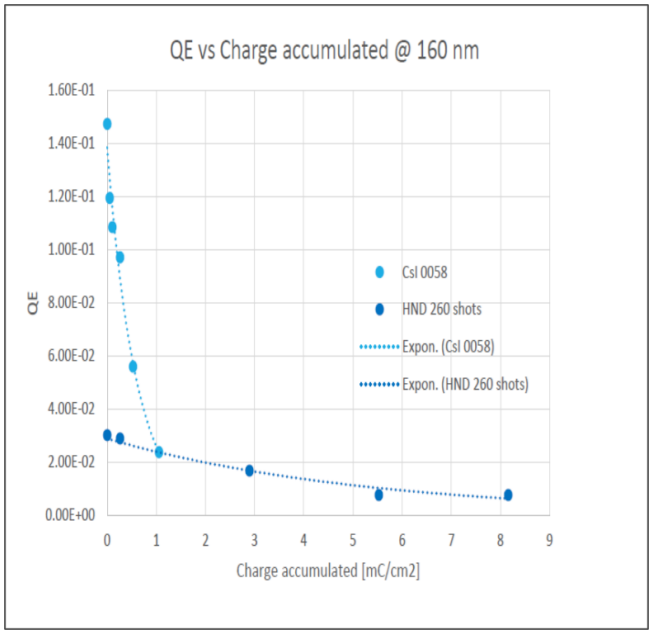

FIGURE 9.5: Absolute quantum efficiency measurement of H-ND and of CsI as a function of the integrated charge; after $\sim 1 mC/cm^2$ the QE of CsI drops below the one of HND.

9.2 Tests of nanodiamond coated THGEMs

The study presented in the previous section shows that nanodiamond-based material can be effectively used as photocathodes to detect photons in the UV range. In view of exporting the present MPGD-based photon detection technology developed for COMPASS RICH-1, a study is carried out to test the coupling of H-ND with THGEMs.
Thirty small size THGEMs, with an active area of $30 \times 30\ mm^2$ were produced with COMPASS standard characteristics. THGEMs are 400 μm thick, coated with a 35 μm thick Cu layer on both sides; holes have no rim and have 400 μm diameter and are arranged in a triangular pattern with 800 μm pitch. The produced THGEMs underwent a post-production process following the protocol described in chapter 6. Above the Cu layer, a 5 μm layer of Ni is deposited and on top of it another layer, 200 nm thick of Au.

9.2.1 Test setup

The THGEMs are tested in a dedicated setup in Trieste that consists in a chamber of dimensions $19\ cm \times 19\ cm \times 5.5 cm$ filled with $Ar : CO_2 = 70 : 30$; along the gas line, after the chamber a sensor measures temperature and pressure of the gas, to ensure the possibility to compare data taken in different environmental conditions. The chamber has a kapton window through which

FIGURE 9.6: The produced THGEMs drying in the oven.

x-ray photons enter the gas volume; tests were done with a ^{55}Fe source like the one described in chapter 7. 7.1 mm above the THGEM a grating of thin metallic wires is suspended to establish the drift field, the field where primary electrons are funneled towards the THGEM holes. The THGEM under test is suspended by plastic spacers at 2.5 mm above the anode plane. The anode is segmented in sixteen 7.7 $mm \times 7.7$ mm pads, kept at ground voltage and connected to the front-end electronics. The readout and acquisition setup is similar to the one described in chapter 7: a charge sensitive amplifier Cremat CR-110 is followed by an Ortec 672 filter, with 2μs shaping time. The shaped signals are recorded by a MCA, which digitizes the spectra and sends them to the acquisition computer. Figure 9.7 shows the setup in Trieste laboratory.

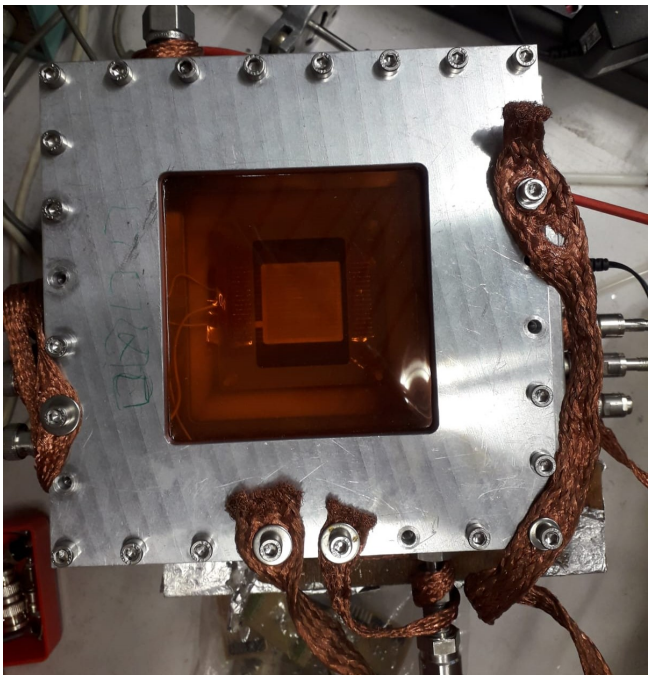

FIGURE 9.7: The test chamber seen from top. Behind the kapton window the THGEM under test is visible.

Uncoated THGEM	$\Delta V_{max}[V]$	Coating	$\Delta V_{max}[V]$
TB XV	1325	H-ND BDD	1325
TB XVI	1375	ND E6	1400
TB XVII	1350	ND BDD	1325
TB XXIV	1375	ND D&T	1325

9.2.2 Coupling of ND photocathodes with THGEMs

To study the effect of the coating on the THGEMs, all the THGEMs were tested before and after coating following a fixed procedure. All the tests presented are performed in Trieste laboratory, while THGEMs are coated with different powders in Bari via the spraying technique described in section 9.1.1; after the coating, THGEMs are stored in an oven at 120° C for $\sim$ $48h$ to remove the water that could have been trapped during the spraying of the nanodiamond solution. The THGEMs are affected by the same gain initial instability that affects the large area THGEMs, described in 7.5.2, hence the characterization procedure starts with a long exposure to ionizing radiation until stable conditions are obtained. The gain is, then, studied as a function of the drift field, of the voltage difference across the THGEM and of the induction field, the field established between the bottom of the THGEM and the anode plane. Pressure and temperature data are recorded once per second during the whole characterization process, for gain correction.

Electrical stability

An important parameter that can be extracted from the characterization is the maximum voltage at which the THGEM can be safely and stably operated. The test is carried out to determine whether the coating affects the detector stability or it has no appreciable effect. The following table summarizes the values of stable operation voltage for different THGEMs. The first column reports the name of the tested THGEM, while the third the coating; second and fourth column are the maximum stable voltage before and after the coating. The small differences can be explained by different environmental conditions and no instability seems to be introduced by the nanodiamond coating.

Gain as a function of the electric field across the THGEM

The gain of the chamber is extracted from the spectrum of the ^{55}Fe source, from a fit to the main peak that corresponds to $\sim$ 220 primary electrons, as discussed in chapter 7. The following table summarizes the values of the gain at gain stabilization with $\Delta V_{THGEM} = 1250\ V$, before and after coating; there is no evidence that the nanodiamond coating enhances or reduces the gain of the chamber. A study of the gain as a function of the voltage difference applied through the THGEMs, presented in figure 9.8 shows that the exponential dependence of the gain on ΔV_{THGEM} is unaffected by the nanodiamond coating. The study presented in this chapter shows that, due to their robustness and easy handling, nanodiamond based photocathodes are

Uncoated THGEM	Effective Gain	Coating	Effective Gain
TB XV	82	H-ND BDD	87
TB XVI	75	ND E6	63
TB XVII	84	ND BDD	69
TB XXIV	82	ND D&T	91

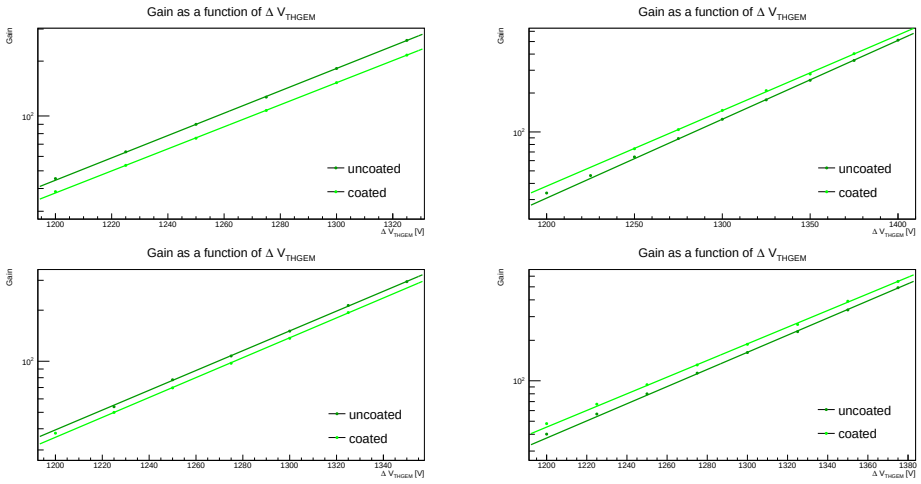

FIGURE 9.8: The gain a function of ΔV_{THGEM} for an uncoated (dark green) and coated (light green) THGEMs. From top left and clockwise, TB XV, TB XVI, TB XXIV and TB XVII. No appreciable variations in the slope are observed.

potentially good candidates to replace CsI ones in future experiments. Moreover, nanodiamond coating is compatible with THGEM technology, paving the way to a new generation of detectors.

Bibliography

[1] J M B Kellogg et al. "The Magnetic Moments of the Proton and the Deuteron: The Radiofrequency Spectrum of H_2 in Various Magnetic Fields". In: *Physical Review* 56 (1939), pp. 728–742.

[2] L W Alvarez and F Bloch. "A Quantitative Determination of the Neutron Moment in Absolute Nuclear Magnetons". In: *Physical Review* 57 (1940), p. 111.

[3] M N Rosenbluth. "High energy elastic scattering of electrons on protons". In: *Physical Review* 79.4 (1950), p. 615.

[4] J D Bjorken and E A Paschos. "Inelastic electron-proton and γ-proton scattering and the structure of the nucleon". In: *Physical Review* 185.5 (1969), p. 1975.

[5] B Povh et al. *Particles and Nuclei: An Introduction to the Physical Concepts*. Springer, 1993.

[6] A Bettini. *Introduction to elementary particle physics*. Cambridge university press, 2008.

[7] R. L. Workman et al. "Review of Particle Physics". In: *PTEP* 2022 (2022), p. 083C01. DOI: 10.1093/ptep/ptac097.

[8] Murray Gell-Mann. "A Schematic Model of Baryons and Mesons". In: *Physics Letters B* 8 (1964), pp. 1–4.

[9] C. Adolph et al. "The spin structure function g_1^p of the proton and a test of the Bjorken sum rule". In: *Phys. Lett. B* 753 (2016), pp. 18–28.

[10] C. Adolph et al. "Final COMPASS results on the deuteron spin-dependent structure function g_1^d and the Bjorken sum rule". In: *Phys. Lett. B* 769 (2017), pp. 34–41.

[11] Aneesh Manohar R.L. Jaffe. "The g1 problem: Deep inelastic electron scattering and the spin of the proton". In: *Nuclear Physics B*, 337 (3 1990), pp. 509–546.

[12] M Alekseev et al. "Flavour separation of helicity distributions from deep inelastic muon–deuteron scattering". In: *Physics Letters B* 680.3 (2009), pp. 217–224.

[13] M Alekseev et al. "Gluon polarisation in the nucleon and longitudinal double spin asymmetries from open charm muoproduction". In: *Physics Letters B* 676.1-3 (2009), pp. 31–38.

[14] J. Ashman et al. "A measurement of the spin asymmetry and determination of the structure function g1 in deep inelastic muon-proton scattering". In: *Physics Letters B* 206.2 (1988), pp. 364–370.

[15] J. Ashman et al. "An investigation of the spin structure of the proton in deep inelastic scattering of polarised muons on polarised protons". In: *Nuclear Physics B* 328.1 (1989), pp. 1–35.

[16] E S Ageev et al. "Gluon polarization in the nucleon from quasi-real photoproduction of high-pT hadron pairs". In: *Physics Letters B* 633.1 (2006), pp. 25–32.

[17] C. Adolph et al. "Experimental investigation of transverse spin asymmetries in $\mu - p$ SIDIS processes: Collins asymmetries". In: *Phys. Lett. B* 717 (2012), pp. 376–382.

[18] C. Adolph et al. "A high-statistics measurement of transverse spin effects in dihadron production from muon–proton semi-inclusive deep-inelastic scattering". In: *Phys. Lett. B* 736 (2014), pp. 124–131.

[19] Anna Martin, Franco Bradamante, and Vincenzo Barone. "Extracting the transversity distributions from single-hadron and dihadron production". In: *Phys. Rev. D* 91 (1 2015), p. 014034.

[20] M. Anselmino et al. "Transverse momentum dependence of the quark helicity distributions and the Cahn effect in double-spin asymmetry A_{LL} in semiinclusive DIS". In: *Phys. Rev. D* 74 (7 2006), p. 074015.

[21] Alessandro Bacchetta et al. "Semi-inclusive deep inelastic scattering at small transverse momentum". In: *Journal of High Energy Physics* 2007.02 (2007), p. 093.

[22] Gerhard K Mallot, Compass Collaboration, et al. "The COMPASS spectrometer at CERN". In: *Nuclear Instruments and Methods in Physics Research Section A: Accelerators, Spectrometers, Detectors and Associated Equipment* 518.1-2 (2004), pp. 121–124.

[23] R. Abdul Khalek et al. "Science Requirements and Detector Concepts for the Electron-Ion Collider: EIC Yellow Report". In: *Nucl. Phys. A* 1026 (2022), p. 122447.

[24] E Nappi. "Advances in charged particle identification techniques". In: *Nuclear Instruments and Methods in Physics Research Section A: Accelerators, Spectrometers, Detectors and Associated Equipment* 628.1 (2011), pp. 1–8.

[25] P Cherenkov. "Visible Radiation Produced by Electrons Moving in a Medium with Velocities Exceeding that of Light". In: *Physical Review* 52 (1937), p. 378.

[26] E Nappi and J Seguinot. "Ring Imaging Cherenkov Detectors: The state of the art and perspectives". In: *Rivista del Nuovo Cimento* 28.8-9 (2005).

[27] I Frank and Ig Tamm. "Coherent visible radiation of fast electrons passing through matter". In: *Selected Papers*. Springer, 1991, pp. 29–35.

[28] Thomas Ypsilantis and Jacques Séguinot. "Theory of ring imaging Cherenkov counters". In: *Nuclear Instruments and Methods in Physics Research Section A: Accelerators, Spectrometers, Detectors and Associated Equipment* 343.1 (1994), pp. 30–51.

[29] O Chamberlain. "The early antiproton work". In: *Nobel Lecture* (1959).

[30] T Ypsilantis and J Seguinot. "Theory of ring imaging Cherenkov counters". In: *Nuclear Instruments and Methods in Physics Research Section A: Accelerators, Spectrometers, Detectors and Associated Equipment* 343 (1994), pp. 30–51.

[31] D Bartlett et al. "Performance of the Cherenkov counters in the Fermilab tagged photon spectrometer facility". In: *Nuclear Instruments and Methods in Physics Research Section A: Accelerators, Spectrometers, Detectors and Associated Equipment* 260 (1987), pp. 55–75.

[32] A Roberts. "A new type of Cherenkov detector for the accurate measurement of particle velocity and direction". In: *Nuclear Instruments and Methods* 9 (1960), pp. 55–66.

[33] J Seguinot and T Ypsilantis. "Photo-ionization and Cherenkov Ring Imaging". In: *Nuclear Instruments and Methods* 142 (1977), pp. 377–391.

[34] S Dalla Torre. "Gaseous counters with CsI photocathodes: The COMPASS RICH". In: *Nuclear Instruments and Methods in Physics Research Section A: Accelerators, Spectrometers, Detectors and Associated Equipment* 970 (2020), p. 163768.

[35] F sauli. *Gaseous radiation detectors*. Cambridge University Press, 2014.

[36] F sauli. *Micro-pattern gaseous detectors*. World Scientific, 2020.

[37] Fabio Sauli. "GEM: A new concept for electron amplification in gas detectors". In: *Nuclear Instruments and Methods in Physics Research Section A: Accelerators, Spectrometers, Detectors and Associated Equipment* 386.2-3 (1997), pp. 531–534.

[38] Y Giomataris. "Development and prospects of the new gaseous detector "Micromegas"". In: *Nuclear Instruments and Methods in Physics Research Section A: Accelerators, Spectrometers, Detectors and Associated Equipment* 419.2-3 (1998), pp. 239–250.

[39] Fulvio Tessarotto. "Status and perspectives of gaseous photon detectors". In: *Nuclear Instruments and Methods in Physics Research Section A: Accelerators, Spectrometers, Detectors and Associated Equipment* 876 (2017), pp. 225–232.

[40] F Sauli. "A rich legacy". In: *Nuclear Instruments and Methods in Physics Research Section A: Accelerators, Spectrometers, Detectors and Associated Equipment* 970 (2020), p. 163440.

[41] G van Apeldoorn et al. "Gating the MWPC's of the DELPHI Barrel RICH". In: (1989). URL: http://cds.cern.ch/record/2626685.

[42] L L Jones et al. "The APV25 deep submicron readont chip for CMS detectors". In: (1999). DOI: 10.5170/CERN-1999-009.162. URL: http://cds.cern.ch/record/432224.

[43] J Agarwala et al. "The high voltage system with pressure and temperature corrections for the novel MPGD-based photon detectors of COMPASS RICH-1". In: *Nuclear Instruments and Methods in Physics Research Section A: Accelerators, Spectrometers, Detectors and Associated Equipment* 942 (2019), p. 162378.

[44] G de Geronimo et al. "The VMM3a ASIC". In: *IEEE Transactions on Nuclear Science* 69.4 (2022), pp. 976–985.

[45] G Iakovidis. "VMM3a, an ASIC for tracking detectors". In: *Journal of Physics: Conference Series*. Vol. 1498. 1. IOP Publishing. 2020, p. 012051.

[46] G De Geronimo et al. "VMM1 - An ASIC for Micropattern Detectors". In: *IEEE Transactions on Nuclear Science* 60.3 (2013), pp. 2314–2321.

[47] T Alexopoulos et al. "The VMM readout system". In: *Nuclear Instruments and Methods in Physics Research Section A: Accelerators, Spectrometers, Detectors and Associated Equipment* 955 (2020), p. 163306.

[48] Shuddha Shankar Dasgupta. "Particle Identification with the Cherenkov Imaging Technique using MPGD Based Photon Detectors for Physics at COMPASS Experiment at CERN". PhD thesis. 2017.

[49] Prijil Mathew et al. "Experimental verification of modified Paschen's law in DC glow discharge argon plasma". In: *AIP Advances* 9.2 (2019), p. 025215.

[50] M Alexeev et al. "The gain in Thick GEM multipliers and its time evolution". In: *Journal of Instrumentation* 10 (2015), P03026.

[51] J Byrne. "Statistics of electron avalanches in the proportional counter". In: *Nuclear Instruments and Methods* 74.2 (1969), pp. 291–296.

[52] Y. Xie et al. "Quantum efficiency measurement of CsI photocathodes using synchrotron radiation at BSRF". In: *Nuclear Instruments and Methods in Physics Research Section A: Accelerators, Spectrometers, Detectors and Associated Equipment* 664.1 (2012), pp. 310–316.

[53] A Buzulutskov, A Breskin, and R Chechik. "Field enhancement of the photoelectric and secondary electron emission from CsI". In: *Journal of Applied Physics* 77.2138 (1995).

[54] L Velardi, A Valentini, and G Cicala. "Highly efficient and stable ultraviolet photocathode based on nanodiamond particles". In: *Applied Physics Letters* 108.8 (2016), p. 083503.

[55] H Rabus et al. "Quantum efficiency of cesium iodide photocathodes in the 120–220nm spectral range traceable to a primary detector standard". In: *Nuclear Instruments and Methods in Physics Research Section A: Accelerators, Spectrometers, Detectors and Associated Equipment* 438.1 (1999), pp. 94–103.